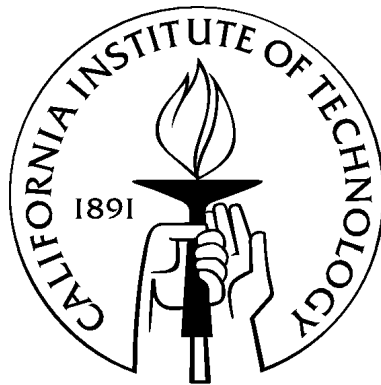


Interaction Law for a Collision Between Two Solid Particles in a Viscous Liquid

Thesis by
Fu-Ling Yang

In Partial Fulfillment of the Requirements
for the Degree of
Doctor of Philosophy



California Institute of Technology
Pasadena, California

2006

(Defended May 05 2006)

© 2006

Fu-Ling Yang

All Rights Reserved

Acknowledgements

There are many people to whom I owe my deepest gratitude for their support and understanding during my years at Caltech. I learned from them the confident but humble attitude as a scientist as well as the elegant and joyful way of living.

I especially thank Professor Melany L. Hunt who introduced me to the world of solid-liquid flows five years ago when I came aboard with the desire of studying forest fires. I am indebted to her for the full support and understanding along the way I built up my sense of conducting research and became devoted to the field of multiphase flow at large scales.

I am also grateful to my committee members, Professors John F. Brady, Christopher E. Brennen, Tim Colonius, and José Roberto Zenit Camacho, for their insightful discussions of the many problems I encountered in my study. I thank them for taking the time to review and comment on my dissertation.

The experimental work of this thesis would have been impossible without the help of my group mates, Dr. Gustavo Joseph and Angel Ruiz, who generously shared with me their knowledge on resolving the numerous difficulties in my laboratory work. I also thank Rodney Rojas and John Van Deusen at the ME shop who helped me with the machining, the task of which is always beyond my capability as an engineering student.

Most of all, I would like to thank my friends at Caltech who helped to make the demanding campus life seem normal. Special thanks to Stuart Laurence and Eric Johnsen who greatly helped me with my stressful thesis writing. Hsin-Ying Chiu, Vanessa Lin, and Min Tao shared all my happy and sad moments during the past few years. I am grateful to have them as my lifelong friends.

At last, but never the least, I want to thank my family and my dearest friends, Yu-Ching Huang and Kang-Ning Lin, for all their love and support. The most important person, whom I dedicate my thesis to, is my former advisor at National Taiwan University, Professor Shih-Ton Lee, who urged my graduate study in the states.

Abstract

This thesis addresses the problem of inter-particle collisions in a viscous liquid. Experimental measurements were made on normal and oblique collisions between identical and dissimilar pairs of solid spheres. The experimental evidence supports the hypothesis that the normal and the tangential component of motions are decoupled during a rapid collision.

The relative particle motion in the normal direction is crucial to an immersed collision process and can be characterized by an effective coefficient of restitution and a binary Stokes number. The effective coefficient of restitution monotonically decreases with a diminishing binary Stokes number, indicating a particle motion with less inertia and higher hindering fluid forces. The correlation between the two parameters exhibits a similar trend to what is observed in a sphere-wall collision, which motivates a theoretical modeling.

The collision model developed in the current work includes a flow model and a revised rebound scheme. The flow model considers the steady viscous drag, the added mass force, and the history force. How the presence of a second nearby solid boundary affects these forces is investigated. A flow model is proposed with wall-correction terms and is used to predict an immersed pendulum motion towards a solid wall. General agreement with the available experimental data validates the model. The rebound scheme considers the magnitude of the surface roughness and the minimum distance of approach resulting from an elasto-hydrodynamic contact.

The performance of the collision model in predicting the effective coefficient of restitution is evaluated through comparisons with experimental measurements and an existing elasto-hydrodynamic collision model that the current work is based on.

Based on the current experimental findings, the tangential component of motion can be described by a dry collision model, provided that the material parameters are properly modified for the interstitial liquid. Two pertinent parameters are the normal effective coefficient of restitution and an effective friction coefficient.

Contents

Acknowledgements	iii
Abstract	v
Table of Contents	vii
List of Figures	xi
List of Tables	xvii
1 Introduction	1
1.1 Motivation.....	1
1.2 Background: Sphere motion towards a solid wall in a liquid.....	3
1.3 Dimension analysis.....	4
1.4 Thesis Outline.....	5
2 Particle-Particle Immersed Normal Collision	7
2.1 Introduction.....	7
2.2 Experiment setup.....	12
2.2.1 Apparatus.....	12
2.2.2 Material properties.....	15
(a) Solid properties	
(b) Liquid properties	
2.2.3 Image analysis.....	16
2.3 Physical parameters.....	19
2.3.1 Coefficient of restitution in a liquid.....	19
2.3.2 Binary Stokes number.....	22

2.4	Normal collisions between spheres of identical sizes.....	25
2.4.1	Identical spheres.....	25
2.4.2	Dissimilar spheres.....	27
2.4.3	Comparison with particle-on-wall collision.....	29
2.5	Particle motion with zero coefficient of restitution	32
2.6	Summary	36
3	Wall Effects on the Hydrodynamic Forces	37
3.1	Background.....	37
3.2	Viscous drag.....	39
3.2.1	Higher Reynolds number effects	39
3.2.2	Wall effects on the steady viscous drag.....	39
3.3	Added mass force.....	41
3.3.1	Added mass force with a wall.....	41
	(a) Behavior of the wall correction term $W(\delta^*)$	43
	(b) Derivative of $W(\delta^*)$	47
3.4	History force	51
3.4.1	Moderate Reynolds number effects	53
3.4.2	Wall effects on the history force.....	55
3.5	Summary	63
4	Immersed Pendulum Motion Towards a Solid Wall	64
4.1	The equation of motion.....	65
4.2	Rebound in a liquid.....	69
4.2.1	EHL collision of two solid spheres	70
	(a) Outline of the paper by Davis et al., 1986.....	70
	(b) Comments.....	73
4.2.2	Contact mechanism in liquid	76
	Case I: Asperity contact.....	77
	Case II: Wet contact (EHL contact).....	77

Case III. Mixed contact	78
4.2.3 Determination of the critical Stokes number	81
4.2.4 Alternative prediction of the coefficient of restitution	84
4.3 Rebound in simulation	86
4.3.1 Summary of the rebound schemes	86
4.3.2 Velocity at wall.....	86
4.3.3 Hertzian contact time and initial rebound condition.....	88
4.4 Simulation Results	89
4.4.1 Asperity Contact at σ_s ; rebound with $U_r = -e_{dry} U_i$ ($e_{dry} = 0.97$).....	90
(a) High impact Reynolds and Stokes numbers: (Re=970, St=840).....	90
(b) High Reynolds number, moderate Stokes number: (Re=745, St=211)....	91
(c) Moderate Reynolds number, low Stokes number: (Re = 210, St = 56) ...	92
(d) Low Reynolds and Stokes numbers: (Re = 34, St = 8)	94
4.4.2 EHL contact at δ_m ; rebound with $U_r = -U_i$	95
Moderate Reynolds and Stokes number (Re=30, St=21)	95
4.4.3 Mixed contact at $(1-k)\sigma_s$; rebound with $U_r = -e_{dry} \times \eta \times U_i$	97
(a) Moderate Reynolds and Stokes numbers (Re=180, St=136)	97
(b) Moderate Reynolds and Stokes numbers (Re=90, St=70)	99
4.5 Wake Structure.....	101
4.6 Prediction of the effective coefficient of restitution	102
4.6.1 Collision of glass spheres on the Zerodur wall.....	103
4.6.2 Collision of steel spheres on the Zerodur wall.....	104
4.7 Summary	107
5 Oblique Collision Between Two Spheres in a Liquid	109
5.1 Background.....	109
5.1.1 Normal component of motion.....	109
5.1.2 Tangential component of motion.....	111
(a) At the contact point	111
(b) At the sphere center of mass	116

5.2	Experiment setup	119
5.2.1	Apparatus	119
5.2.2	Sphere surface properties	120
5.2.3	Image processing	122
5.2.3	Parameters	123
5.3	Normal component of motion	125
5.4	Tangential component of motion	128
5.4.1	Properties at the contact point	128
5.4.2	Properties at the sphere centers of mass	132
	(a) Rebound angle	132
	(b) Rebound velocity	136
5.5	Conclusion	144
6	Wall influence distance	146
6.1	Examination of the three hydrodynamic forces	146
6.2	Influence distance	156
6.3	Summary	161
7	Conclusion	163
	Bibliography	166
	Appendix	170

List of Figures

2.1	The effective coefficient of restitution as a function of the particle Stokes number for an immersed particle-on-wall normal collision in liquids.....	11
2.2	Schematic experiment setup and the release mechanism.....	13
2.3	Fixture plate with respect to the release mechanism.....	13
2.4	Illumination effects: direct and background lightening.....	15
2.5	Image conversion from RGB to binary format for a binary collision.....	17
2.6	Time evolution of the particle trajectories and the distance between the sphere centers.....	18
2.7	Schematic collision process.....	20
2.8	Effective coefficient of restitution as a function of binary Stokes number for immersed normal collisions between identical spheres.....	26
2.9	Effective coefficient of restitution as a function of binary Stokes number for immersed normal collisions between dissimilar spheres.....	27
2.10	Immersed inter-particle normal collisions between identical and dissimilar spheres.....	28
2.11	Comparison of the inter-particle and the particle-wall immersed collisions	30
2.12	An enhanced restitution due to rebounds at a greater interstitial distance...	31
2.13	Time evolution of the interstitial gap for a collision of zero restitution.....	33
2.14	Time evolution of the interstitial gap for impacts that result in zero restitution but non-zero particle motion after collision.....	34
2.15	Group efficiency number with respect to the binary Stokes number.....	35
3.1	The collapse of the partial sum of the wall correction term $W_N(\delta^*)$, $N = 3-7$, to the numerical sum of 100 terms.....	46
3.2	Discrepancy between $W_5(\delta^*)$ and $W_{100}(\delta^*)$ for $\delta^* < 0.02$	46

3.3	Derivative of the wall correction term is numerically evaluated with the first 40 and 100 terms.....	48
3.4	Comparison between the 40-term and 3-term partial sums.....	49
3.5	The 3-, 5-, and 7-term partial sums of the derivatives deviate from the 40-term partial sum when the gap drops to zero.....	49
3.6	Comparison between the 3-term approximation and the hybrid-formulation.....	51
3.7	Infinitesimal stepwise acceleration of the plate.....	56
3.8	Coordinates for the Mangler's transformation.....	57
3.9	Schematic sketch of the potential flow problem when a solid sphere moves towards a solid wall.	58
3.10	Potential functions with and without wall at different gaps.....	60
3.11	Flow velocity at the sphere surface with decreasing gaps: (a) tangential and (b) radial component.....	61
3.12	Augmentation factor for the wall-modified history force as a function of the scaled gap.....	62
4.1	Schematic representation of a pendulum motion towards a wall in liquid...	65
4.2	Archimedes number as a function of the characteristic Reynolds number for an immersed pendulum motion from $\theta_0 = 15^\circ$	67
4.3	The preceding dimensionless factor of the effective gravity.....	68
4.4	Schematic of elastohydrodynamic collision of a sphere on a stationary wall in a viscous liquid.....	70
4.5	Minimum distance of approach for a deformed sphere as a function of the elasticity parameter and the particle Stokes number.....	72
4.6	The normalized gap at which the wall-modified Stokes' drag reaches 99% of the classical lubrication force at the same impact Reynolds number.....	74
4.7	Comparison of the added mass and the lubrication force as a function of normalized gap for an immersed collision at $Re_i \approx 50$ and $St_i \approx 14$	75
4.8	Sphere collides and rebounds via an asperity contact.....	77
4.9	Asperity deforms as a hemispherical indenter under lubrication force.....	79

4.10	Interaction between the impact sphere and the fluid trapped between the surface asperities during a mixed contact.....	80
4.11	Schematic immersed collision process: (a) impact and (b) rebound.....	85
4.12	Extrapolation of the instant impact velocity is compared with the linearly interpolated value at the rebound distance.....	87
4.13	Comparison of the simulation results with the experiment data: $Re = 970$, $St = 840$	91
4.14	Comparison of the simulation results with the experiment data: $Re = 745$, $St = 211$	92
4.15	Comparison of the simulation results with the experiment data: $Re = 210$, $St = 56$	93
4.16	Comparison of the simulation results with the experiment data: $Re = 34$, $St = 8$	95
4.17	Comparison of the simulation results with the experiment data: $Re = 30$, $St = 21$	96
4.18	Comparison of the simulation results with the experiment data: $Re = 180$, $St = 136$	98
4.19	Comparison of the simulation results with the experiment data: $Re = 90$, $St = 70$	100
4.20	Flow visualization of a particle-wall immersed collision.....	102
4.21	Predicted coefficient of restitution for collisions between glass spheres.....	104
4.22	Predicted coefficient of restitution for collisions between ball bearings.....	105
4.23	Collision model prediction of the effective coefficient of restitution.....	106
5.1	The schematic representation of the sphere-on-wall oblique collision and the relevant parameters.....	110
5.2	Normal coefficient of restitution as a function of normal particle Stokes number for oblique collisions in aqueous solutions of glycerol.....	111
5.3	Non-dimensional angle of reflection, ψ_r , as a function of the angle of incidence, ψ_i	113

5.4	Effective friction coefficient, μ_C , as a function of tangential impact Stokes number.....	115
5.5	Non-dimensional angle of reflection, ψ_r , as a function of incidence angle, ψ_i , for an immersed oblique particle-wall collision.....	116
5.6	Impact of two spheres in a plane motion.....	117
5.7	Apparatus for an immersed binary oblique collision.....	120
5.8	SEM images of the two classes of steel particles.....	121
5.9	Images tracking and processing for oblique binary collision.....	123
5.10	Decomposition of the impact motion with respect to the contact normal into a normal and a tangential components.....	124
5.11	Normal coefficient of restitution as a function of normal binary Stokes number for immersed oblique collisions between identical spheres.....	126
5.12	Comparison between (e, St_B) and (e_n, St_n) for normal and the normal component of an oblique binary collision.....	127
5.13	Effective angle of reflection as a function of the effective incidence angle for immersed oblique collisions.....	130
5.14	Comparison of the effective reflection angle as a function of effective angle of incidence.....	131
5.15	Rebound angle of the impact sphere as a function of the impact angle at the sphere centers of mass.....	133
5.16	Rebound angle of the target sphere as a function of the impact angle at the sphere centers of mass.....	133
5.17	Effective rebound angle as a function of the tangential Stokes number.....	135
5.18	Effective rebound angle as a function of impact angle.....	136
5.19	Rebound angle at impact steel ball bearing center as a function of impact angle when $500 < St_n < 2400$	137
5.20	Rebound angle at impact steel ball bearing center as a function of impact angle when $St_n < 25$	138

5.21	Rebound angle at the impact Delrin sphere center as a function of impact angle when $40 < St_n < 200$	139
5.22	Rebound angle of the target sphere for immersed oblique collisions at different normal Stokes numbers.....	140
5.23	Comparison of the predicted post-collision velocity of the impact sphere using (a) <i>GS1</i> and (b) <i>GS2</i> ($\mu_c = 0.02$).....	141
5.24	<i>GS2</i> prediction with a higher lubricated friction coefficient.....	142
5.25	Comparison of the predicted tangential rebound velocity of the target sphere using (a) <i>GS1</i> and (b) <i>GS2</i> ($\mu_c = 0.02$) collision models.....	143
6.1	Comparison of the predicted pendulum motion using the full or the partial flow model with $\rho_p/\rho_f = 2.55$, at $St = 214$	148
6.2	The influence of each hydrodynamic force in determining the motion of a solid sphere of, $\rho_p/\rho_f = 2.0$, that approaches the wall at $St = 50$	149
6.3	The influence of each hydrodynamic force on the approach of a dense solid sphere of $\rho_p/\rho_f = 6.83$, that impacts at $St = 68$	150
6.4	The three hydrodynamic forces as a function of the scaled gap with (a) $St_i = 488$, (b) $St_i = 198$, (c) $St_i = 42$, and (d) $St_i = 12$ and ($\rho_p/\rho_f = 6.83$)...	152
6.5	The local added mass force scaled by the steady viscous force, as a function of scaled gap and impact particle Stokes number.....	153
6.6	The local force ratio between the added mass force and the steady viscous force as a function of St , $\delta^* = \delta/D$, and the solid-to-liquid density ratio...	154
6.7	The local force ratio between the history force and the steady viscous force as a function of St , $\delta^* = \delta/D$, and the solid-to-liquid density ratio...	155
6.8	Comparison of the velocity profile between a free swinging pendulum and a pendulum motion towards a wall.....	156
6.9	Determination of the influence distance.....	157
6.10	The predicted velocity profile for three pendulum motion at $Re_c = 530$ but different ρ_p/ρ_f	158

6.11	The predicted velocity profile for three pendulum motion at $Re_c = 175$ but different ρ_p / ρ_f	159
6.12	The dependence of the influence distance on the impact particle Stokes number and the solid-to-liquid density ratio.....	160

List of Tables

2.1 Properties of the spheres used in collision experiments	16
4.2. Summary of rebound mechanism for a fully immersed collision.....	86

Chapter 1

Introduction

1.1 Motivation

A debris flow or slurry is a mixture of solid particles and liquid, and the motion of such a material characteristically exhibits both solid and liquid aspects. The particle interactions dominate the behavior of the dispersed phase, contributing to the solid-like behavior of a mixture as sustaining and resisting the external load. The continuous liquid phase lubricates the surfaces and mediates the particle collisions. However, because the liquid has a comparable density to the solid phase, the liquid motion and its non-negligible viscous and inertial effects introduce additional mechanisms for momentum transport and energy dissipation.

Mixtures of this kind appear in many natural processes, such as rock slides and debris flows, meandering rivers and sedimentation processes. Particulate flows are also important in many industrial and engineering applications, including slurry transport, erosion, mining and milling engineering, and chemical and pharmaceutical processes. Despite the prevalence of these solid-liquid flows, a general theoretical model of the flow behavior is as yet unavailable, owing to the dual nature of the mixture. Most of the industrial processes are designed empirically, and flow control and system modifications are limited due to the poor understanding of the mixture as a bulk. With the advances in

current computational performance, future advances in flow simulation may provide an understanding of the mixture behavior under various flow conditions. The existing numerical schemes fall into two distinct groups.

For flows with negligible fluid effects, the instantaneous particle-particle collisions dominate the bulk behavior. The numerical methods treat the mixture as a discrete system of particles whose interactions are usually described with a force-displacement relation that accounts for surface friction and particle collisions (Campbell 1990). For problems with increasing fluid effects, a modification on the particle interaction law would be crucial for a realistic simulation.

Alternatively, if the interstitial liquid significantly affects the motion of the particles, simulations within a hypothesized continuum framework are usually sought. The two phases are described separately and their interactions couple the two equations through stress terms. A description of these terms requires a constitutive relation of the mixture and the interaction between the two phases at the particle level (Iverson 1997; Zhang and Prosperetti 1994). One extreme case is a suspension in which the solid particles possess nearly matching density to the ambient fluid. A solid particle in this case follows the local fluid motion and direct collisions are infrequent due to the lack of particle inertia relative to the flowing liquid. The continuum model describes the mixture as a liquid under the premise that the flow material constants can be modified to account for the presence of the suspended particles. Such a modification requires the knowledge of how a flowing particle interacts with the surrounding liquid and with other particles through long-range forces (Einstein 1906; Nott and Brady 1994).

While extensive work has been done independently for each group of flows, a hybrid numerical scheme that bridges the two aspects is not readily available. Such a scheme

would simulate the important class of solid-liquid flows in which the motion of both phases is equally important in determining the bulk behavior. If a discrete scheme is to be used, the effects of the interstitial fluid could be accommodated by a new particle-particle interaction law. As for a continuum model, the material properties of a mixture would have to account for the dispersive interaction between the colliding solids. Either approach would require a realistic description of the local interactions between solid particles and the surrounding liquid. A successful model of the bulk behavior would thus depend critically on an exact description at a small scale. The work presented here represents a first step toward such a model.

1.2 Background :

Sphere motion towards a solid wall in a liquid

The problem of a solid sphere moving towards a wall or another sphere in a liquid has been studied analytically by different researchers. If the surrounding liquid is idealized as incompressible and inviscid, the hydrodynamic force acting on the sphere can be found by potential flow theory (Lamb 1932; Milne-Thomson 1968), where the image method is applied to satisfy the wall boundary condition. For a viscous liquid, Brenner analyzed the constant approach of a sphere towards a wall at small Reynolds number (1961). A correction to the Stokes' drag was developed to account for the presence of the wall, taking the form of a monotonically increasing drag with decreasing sphere-wall gap. If the solid surface is rigid and perfectly smooth, as assumed in the analysis, the sphere is predicted to fully stop before collision. Davis, Serayssol, and Hinch (1986) considered the elastic deformation of the solid surfaces owing to the increase in the interstitial fluid pressure upon impact. Such an approach followed the concept of elastohydrodynamic lubrication theory (EHL). Their work revealed the importance of solid inertia in

predicting the sphere's motion in a liquid and resultant surface deformation. The particle Stokes number, $St = m_p U_i / 6\pi\mu_f a^2$, was defined to characterize the counterbalancing solid inertia and steady viscous drag for a sphere of radius a and mass m_p that moves at velocity U_i in a liquid of viscosity μ_f . In the literature of solid-liquid flows, the particle Stokes number is usually represented as $St = (\rho_p / \rho_f) Re / 9$ in terms of the solid-liquid density ratio and $Re = \rho_f U_i a / \mu_f$, the particle Reynolds number. McLaughlin (1968), Joseph, Zenit, Hunt, and Rosenwinkel (2001), and Gondret, Lance, and Petit (2002) investigated the immersed collision of a sphere on a wall experimentally. Following the definition of the dry coefficient of restitution, these researchers used the sphere impact and rebound velocities, U_i and U_r , to define an effective coefficient of restitution, $e = -U_r / U_i$, for collisions in a liquid. This number characterizes the particle momentum change during an immersed collision. Within the examined impact conditions, the effective coefficient of restitution was found to decrease monotonically with diminishing particle Stokes number. For an impact at high particle Stokes number, the fluid effects become negligible, resulting in a nearly unity restitution coefficient that approximates a dry impact. However, with increasing liquid viscosity or diminishing particle inertia, the sphere can no longer sustain its motion through the liquid and a critical particle Stokes number was found below which particle rebound does not occur.

1.3 Dimensional analysis

The sphere impact and rebound motion in a liquid with respect to a wall involves the following variables: impact and rebound velocities, U_i and U_r , solid and liquid densities, ρ_p and ρ_f , liquid viscosity, μ_f , the diameter and surface roughness of the sphere, D and σ_s . When elasto-hydrodynamic deformation of the solid surface is considered, the lubrication film thickness, δ_0 , and the sphere Young's modulus, E , are also important.

With three fundamental dimensions-mass, length, and time, these nine variables should form six dimensionless parameters that characterize the immersed collision according to *Buckingham Pi Theorem*. Five out of the six parameters can be readily found as the effective coefficient of restitution, $e = -U_r/U_i$, the density ratio, ρ_p/ρ_f , the particle Reynolds number, $Re = \rho_f U_i a / \mu_f$, the normalized surface roughness and lubrication film thickness, σ_s/D and δ_0/D . The last parameter should relate the surface deformation to the lubrication pressure force and the elasticity parameter, $\varepsilon \sim \mu_f U_i a^{\frac{3}{2}} / E \delta_0^{\frac{3}{2}}$, developed by Davis, Serayssol, and Hinch (1986) is adopted.

1.4 Thesis Outline

The primary goal of this thesis is to investigate the collision between two solid surfaces when the effect of the surrounding liquid is non negligible, with an emphasis on the general physical principles of such a process. In addition to a clearer understanding of the motion in each phase, the knowledge obtained can be used as the building block for future numerical simulations that consider a granular mixture of equally important solid and liquid inertias. In particular, when the approach distance between two solid surfaces drops below the size of a computational grid, the collision model developed in this study would provide a way to estimate the rebound out to a separation greater than a grid cell. This would help to resolve the breakdown of the conservation of mass, a critical problem encountered in many numerical schemes. It could also save the time-consuming matching of the liquid pressure and the solid stress at the interface near contact. (Nguyen and Ladd 2002; Potapov, Hunt, and Campbell 2001).

In chapter 2, the results from a series of experiments investigating normal collision between two immersed spheres are presented. Controllable inter-particle collisions were

achieved using a dual-pendulum apparatus. The effects of the effective coefficient of restitution and the binary Stokes number are characterized.

In order to explain the experimental findings, an equation that describes the approach of a sphere towards a wall is proposed in chapter 3. The relevant hydrodynamic forces, including the steady viscous drag, the added mass force, and the history force, are examined and modified accordingly for the presence of the wall and form a flow model describing the approach of a sphere to a wall.

In chapter 4, the flow model is applied to predict an immersed pendulum motion towards a wall. A rebound scheme that considers the interaction of the surface asperities and the interstitial liquid is proposed. The flow model and the rebound scheme are combined as a collision model. The performance of this collision model in predicting an immersed collision process is evaluated by comparisons with the experimental measurements.

Chapter 5 presents another set of experimental results on oblique immersed collisions between two identical spheres. The particle motion is decomposed into a normal and a tangential component along the line of centers. The normal component of motion is compared with the findings from chapter 2. The tangential component of motion is examined by comparing the data with predictions from dry contact models. This comparison illustrates the interstitial fluid effects and also suggests a general description of an oblique immersed collision.

To understand further the flow physics of an immersed collision, the proposed flow model is examined with various impact conditions in chapter 6. Chapter 7 summarizes these investigations and discusses the general features of an immersed collision.

Chapter 2

Particle-Particle Immersed Normal Collision

2.1 Introduction

The head-on collision between two solid objects has long been a research topic in dynamics and solid mechanics (Goldsmith 1961; Johnson 1985). A collision is conventionally described as a compression process followed by a restitution phase. Upon contact, the solid deforms and stores part of the kinetic energy as strain energy. Some other kinetic energy propagates into the body with the shear, compression, or surface Rayleigh waves. Assuming negligible effects from reflections of these waves, the objects rebound during the restitution phase by recovering the elastic strain energy into kinetic energy. As a consequence of permanent plastic deformation, wave propagation, heat loss, and vibration, a certain amount of kinetic energy is lost. The dry coefficient of restitution is widely accepted as a measure of the overall momentum loss during impact and can be calculated from the ratio of the rebound to the impact velocities. This restitution number has been extensively investigated between various materials from low to high impact velocities. Collisions between soft and ductile materials result in lower restitution, and further reduction occurs at higher impact velocities due to the yielding of the soft material. However, since the impact experiment is often conducted in air or a vacuum environment, little research has been done regarding the surrounding liquid effects. If collision occurs in a liquid, additional surface deformation is possible due to the increase of

hydrodynamic pressure in the interstitial liquid. The viscous liquid also dissipates the energy and may further diminish the restitution process.

Davis, Serayssol, and Hinch (1986) examined the collision of two deformable solid particles with a Newtonian interstitial fluid. Their analysis assumes a quasi-steady flow in the gap (Stokes regime), which is guaranteed by the thin gap width or the small size of the particles involved in the problem. A number that characterizes the ratio of particle inertia to the liquid viscous force is

$$St = \frac{m_p U_i}{6\pi\mu a^2}, \quad (2.1)$$

for a solid sphere of mass m_p and radius a that moves at velocity U_i in a liquid of viscosity μ . The quantity in equation (2.1) is referred to as *Stokes number* in the literature of solid-liquid two-phase flow and often represented by $St = (\rho_p/\rho_f)Re/9$ using the solid-liquid density ratio ρ_p/ρ_f and the particle Reynolds number $Re = 2aU_0/\nu_f$. However, different definitions of Stokes numbers have been established in the following two works.

First, Stokes (1851) studied the equation of motion of a pendulum in air to regulate a mechanical clock for a precise time standard. He derived the unsteady hydrodynamic force on the pendulum as:

$$F(t) = \left(1 + \frac{\sqrt{\pi\beta_s}}{2}\right)6\pi\mu a U_i + \frac{1}{2}\left(1 + \frac{9}{\sqrt{\pi\beta_s}}\right)m_f \frac{dU_i}{dt} \quad (2.2)$$

in the limit of high oscillation frequency. The first and second terms in equation (2.2)

resemble the Stokes steady drag and the added mass force respectively. Both force magnitudes are modified by the “Stokes number:”

$$\beta_S = 4\left(\frac{a^2}{\nu_f}\right) \frac{1}{U_0} \frac{dU_i}{dt},$$

which depends on a characteristic sphere velocity U_0 and the pendulum instant velocity U_i . This Stokes number denotes the ratio of a diffusion time, a^2/ν_f , to a time scale that characterizes the unsteadiness, $U_0/(dU_i/dt)$, of the sphere motion. The subscript “S” is used here to denote Stokes’ definition. More recently, Mei (1992) performed a set of numerical simulations to investigate the correlation between the unsteady drag and the oscillation frequency. Another Stokes number, subscripted with “M,” was defined:

$$\beta_M = \sqrt{\frac{\omega a^2}{2\nu_f}} = \sqrt{\frac{\text{Re } Str}{4}},$$

as a function of sphere Reynolds number and Strouhal number, $Str = \omega a/U_0$. If the sphere motion is expressed as $U_i = U_0 \cos \omega t$, the two definitions can be related by $\beta_S = 8\beta_M^2$. Therefore, both Stokes numbers characterize the rate of diffusion with respect to the sphere translation, which accounts for the unsteadiness of the particle motion but not its inertia against the hydrodynamic forces. In order to distinguish between the different definitions, equation (2.1) is referred as the *particle Stokes number* in the current work.

McLaughlin (1968) was the first to systematically investigate the particle collisions on a stationary wall in a liquid. A solid sphere was released towards the bottom of a vertical tube filled with aqueous glycerin solutions. The sphere rebound trajectory was used to

characterize the momentum and energy interactions between the sphere and the wall upon collision. The post-collision momentum recovery was shown to be a function of the sphere impact Reynolds number. His definition of momentum recovery can be interpreted as an effective coefficient of restitution and estimated based on the impact and rebound velocity in liquids as:

$$e = -\frac{U_r}{U_i}. \quad (2.3)$$

Equation (2.3) is conceptually equivalent to the use of dry coefficient of restitution to characterize the momentum loss during a dry collision.

Barnocky and Davis (1988) dropped a sphere in air onto a target plate that was covered with a thin lubricant layer. The critical drop height for the occurrence of rebounds was determined. To ensure a rebound, the sphere should possess sufficient inertia to overcome the hindering fluid forces for a non-zero velocity upon contact. Therefore, a greater critical drop height was measured when the viscosity and thickness of the liquid layer were increased. Though the effective coefficient of restitution was not the focus of their investigation, the experimental findings suggest the hydrodynamic effects on the sphere motion that results in additional energy dissipation. Gondret et al. (2002) performed similar experiments to McLaughlin's and confirmed the dependence of the effective coefficient of restitution on the particle Stokes number. Zenit et al. (1998) and Joseph et al. (2001) used a pendulum-like apparatus that permits a horizontal impact motion towards a vertical wall. Without the action of gravity on the near wall sphere motion, the resultant effective coefficient of restitution shows a similar dependence on the particle Stokes numbers to the previous research works. The comparison between the fore-mentioned experiments was made by Joseph (2003), as reproduced in figure 2.1.

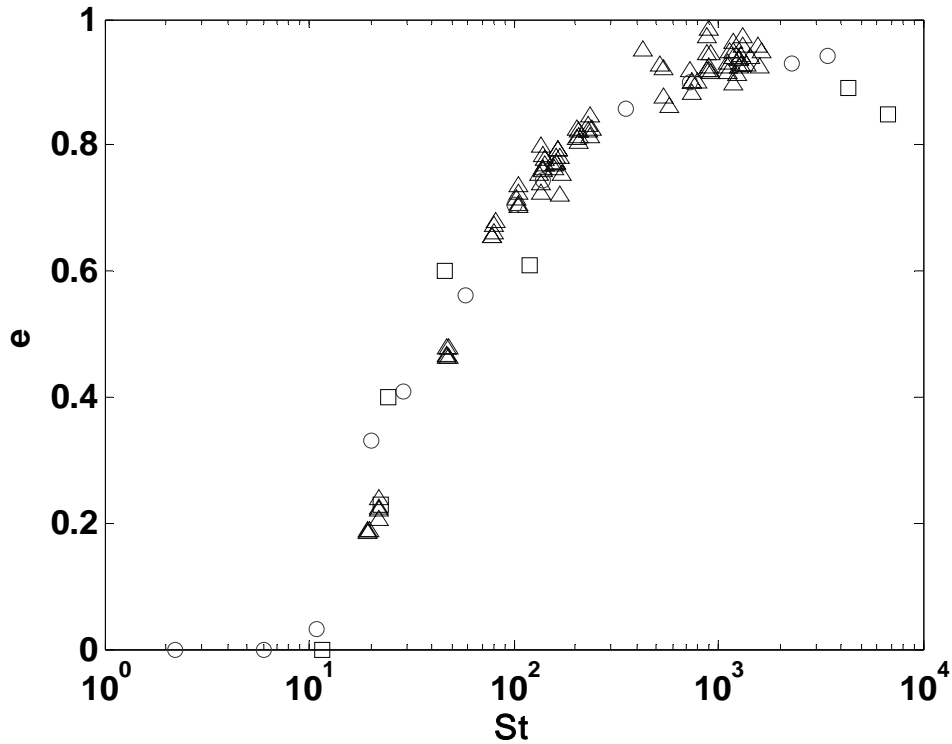


Figure 2.1. The effective coefficient of restitution as a function of the particle Stokes number for an immersed particle-on-wall normal collision in liquids. Steel and glass spheres collide on a stationary wall. (\square : McLaughlin 1968, \circ : Gondret et al. 2002, and Δ : Joseph et al. 2001)

When the sphere approaches the wall at high particle Stokes number, the viscous force becomes negligible, resulting in a nearly unity restitution coefficient, as if the collision took place in a dry medium. However, with decreasing particle Stokes number, the effective coefficient of restitution drops noticeably from e_{dry} . When the particle Stokes number falls below a critical value, a zero restitution coefficient is found, indicating no rebound motion, at least within the resolution of the image acquisition system.

The dependence of e_{dry} on particle Stokes number raises the question of whether a particle-on-particle immersed collision displays a similar trend. If the fixed wall is replaced with an object of finite size, the fluid can move around the target more easily

upon impact. The mobility of the target particle necessitates the reexamination of the parameters: the effective coefficient of restitution and the particle Stokes number, which are used to characterize an immersed on-wall collision. In the current work, the experiments were conducted using spheres of identical size ($D = 12.7$ mm) but different materials. Collisions between identical and dissimilar materials were examined. The experimental results are presented with the effective coefficient of restitution and a *binary Stokes number* for a binary collision that will be defined in section 2.3.2. The inter-particle collision result is also compared with the on-wall data.

2.2 Experiment setup

2.2.1 Apparatus

The particles were suspended as two pendulums in a viscous fluid, as shown in figure 2.2(a), to achieve a controllable inter-particle collision. The current configuration was a hybrid of the apparatuses used by Zenit and Hunt (1998), Joseph et al. (2001) and Joseph and Hunt (2003). A new release mechanism was designed for large impact particles to minimize any disturbance to the surrounding liquid during operation. As shown in figure 2.2(b), a V-shaped block was used to symmetrically support the impact particle whose swing motion was controlled by a gate. The gate was initially held in a closed position by a sturdy spring and, then suppressing the spring released the sphere at an angle θ_0 . By changing the solid materials, the liquid, and the release angle, a wide range of impact conditions could be achieved. The string was 0.02 mm diameter nylon fishing line and its influence on the particle motion has been shown to be negligible (Joseph 2003). Sufficient time was allowed between experiments for the motion of the target sphere and

the liquid to settle down, ensuring a motionless target and a quiescent ambient fluid condition.

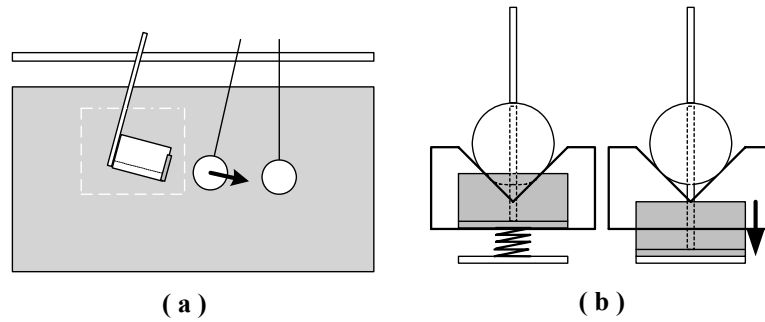


Figure 2.2. (a) Schematic experiment setup, side view, and (b) frontal sketch of the V-shaped release mechanism.

To control the inter-sphere distance upon impact, a precision fixture plate was designed, as shown in figure 2.3. Along the longitudinal plate centerline, two holes were drilled with a spacing of one sphere diameter and fine slots were cut to the side of the plate, allowing the passage of strings. The plate was aligned with the V-block guiding groove, ensuring an in-plane swinging motion. The tank was leveled and as a final calibration, one test collision was recorded from the frontal side to verify a head-on normal collision before each set of experiments.

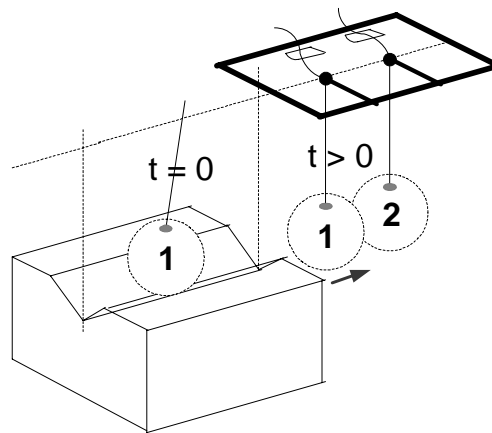
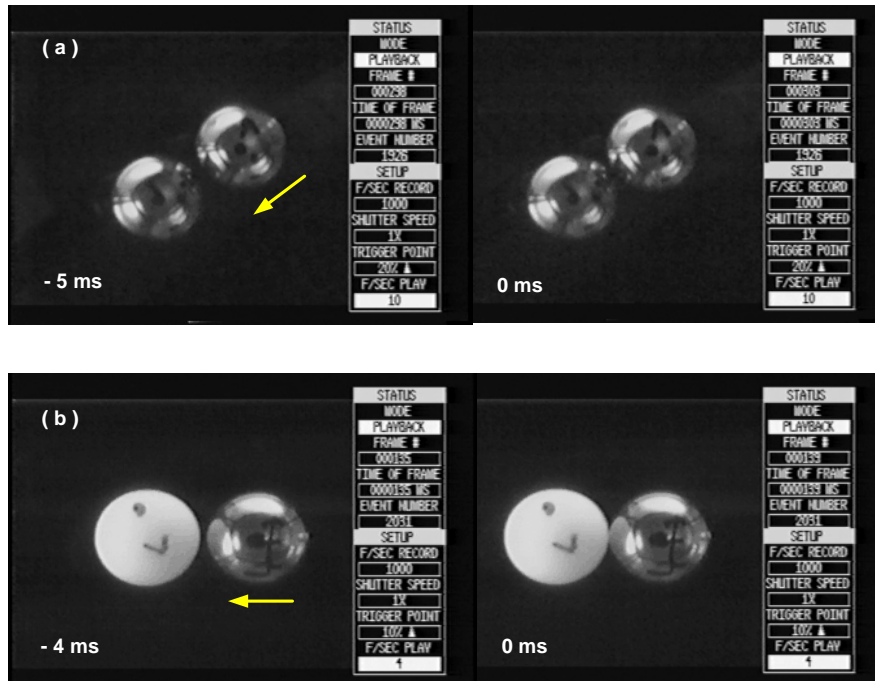


Figure 2.3. Fixture plate and its configuration with respect to the release mechanism.

The sphere motion was recorded from the side or the bottom with a high-speed camera as described in Joseph (2003). The digital images were analyzed later to characterize the collision process. More details regarding the image processing can be found in section 2.2.3. In the cases with steel spheres, direct illumination resulted in bright areas on the mirror-like surface, as shown in figures 2.4(a) and 2.4(b). The uneven surface contrast caused problems in determining the sphere edge during the post-collision image analysis. In addition, the sphere blocked the light, blurring out the contact area, and made it difficult to locate the collision precisely in time. These problems were alleviated by new illumination method-background lighting. The tank was wrapped by translucent paper and illuminated from behind. The resulting images, as shown in figure 2.4(c), had sharper edges than those obtained with direct light. Also, the dark particles contrasted with the liquid well enough to determine the surface contour even upon contact. The method of background illumination also worked for semi-opaque glass spheres, as shown in figure 2.4(d).



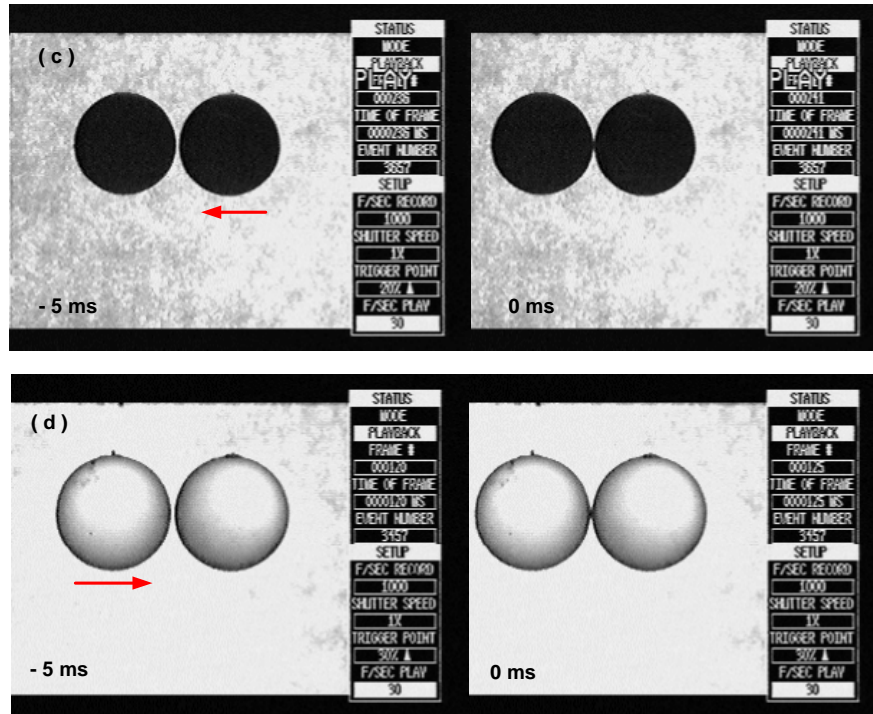


Figure 2.4. Illumination effects. All the spheres are 12.7 mm in diameter. The camera position (side or bottom view), the sphere materials as *impact-on-target*, and the illumination method are as follows: (a) Bottom view, steel-on-steel, direct illumination. (b) Bottom view, steel-on-Delrin, direct illumination. (c) Side view, steel-on-steel, background illumination. (d) Side view, glass-on-glass, background illumination.

2.2.2 Material properties

(a) Solid properties

Three types of 12.7 mm diameter solid spheres were used in the experiments: steel ball bearings, glass, and Delrin spheres. The spheres were identical to the ones used in Joseph (2003). The material properties and sphere surface roughness are summarized in Table 2.1, including solid density ρ_p , Young's modulus E , Poisson's ratio ν , and the sphere surface roughness σ_s .

Table 2.1. Properties of the spheres used in collision experiments (Joseph 2003)

Material	ρ_p (kg/m ³)	E (GPa)	ν	σ_s (μm)
Steel	7780	190	0.27	0.0236
Glass	2540	60	0.23	0.134
Delrin	1400	2.8	0.35	0.796

(b) Liquid properties

The surrounding liquid was water-based glycerol solution whose viscosity varies significantly with temperature. Therefore, the liquid temperature was measured before each collision. The apparent specific weight of the solution was measured using a hydrometer for each set of experiments. The mixture density and viscosity can be extrapolated from the tables once the mixture composition is determined. The apparent specific weight of the liquids used in the current study ranged from 0% to 80%, which corresponds to a density ranging from 990–1210 kg/m³ and a kinematic viscosity of 0.9–47 $\times 10^{-6}$ m²/s. The solution properties with respect to apparent specific weight percentage are readily found (Joseph 2003).

2.2.3 Image analysis

A high-speed digital camera (Redlake MotionScope 8000S) was used to record the collision process at rates 1 kHz or higher. The true color (RGB) image was converted into a binary (black-and-white) format, as from figure 2.5(a) to 2.5(b), by properly tuning the

grayness threshold in ImageJ¹. During conversion, the RGB index of each pixel was transformed into a grayscale with unity and zero indicating true white and black, respectively. If one pixel has grayscale higher than the designated threshold, it is

converted into a white pixel; likewise a black pixel is created for pixels with grayscale lower than the threshold. The periphery of each sphere was determined by its peak contrast to the neighboring pixels with the outer radius representing the sphere surface. A black circle was obtained for steel and Delrin spheres, but a ring was generated for semi-opaque glass particles, as show in figure 2.5(b). The interior unity (white) pixels were replaced with zeros to represent the actual occupancy of the solid material in figure 2.5(c). The sphere centers were located at the mean X- and Y- coordinates of all the black pixels (zeros).

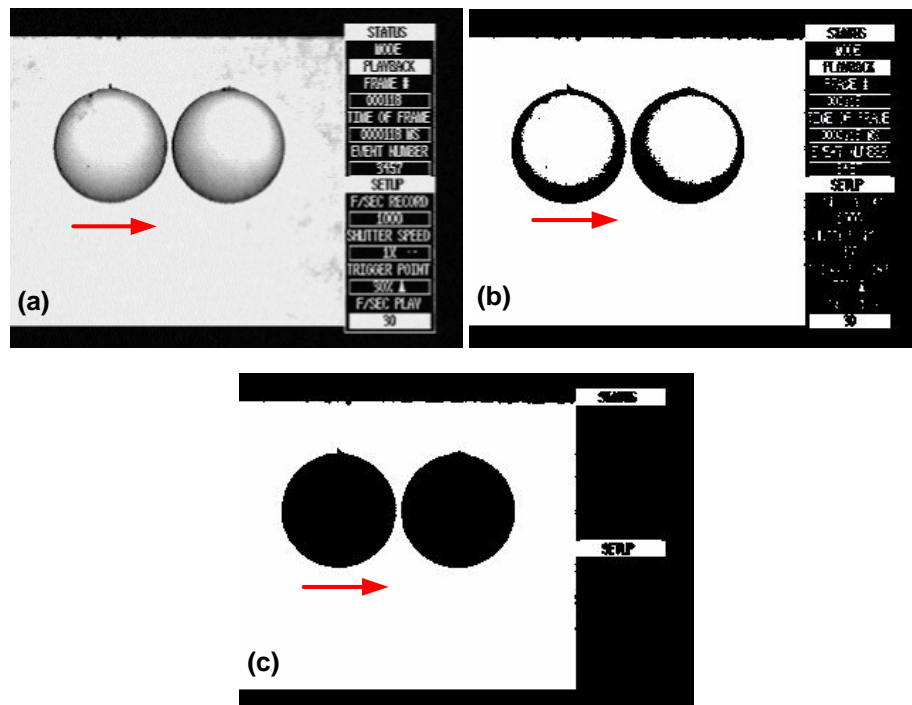


Figure 2.5. Image conversion for a glass-on-glass collision (both 12.7 mm): (a) In RGB true color. (b) Black-and-white rings locating the spheres. (c) Filled binary image.

¹ ImageJ is a Java-based free software.

Each frame was converted and analyzed to determine the time evolution of the particle trajectories. A typical result is shown in figure 2.6(a); in figure 2.6(b), the estimated distance between sphere centers is plotted. The sphere trajectories were fitted in a least-squares sense (in MatLab) before and after the collision to calculate the impact and rebound velocities, U_{i1} , U_{r1} , U_{i2} , and U_{r2} . The resultant velocities slightly varied with respect to the averaging duration. An average over 20 milliseconds would not capture the actual slowdown for a rapid collision. However, a time period shorter than 5 milliseconds does not reflect the real approaching velocity but pronounce only the decelerating particle motion. An intermediate time period, 10 to 15 milliseconds, was chosen such that the standard deviations for the four velocities are of the same order of magnitude in one collision.

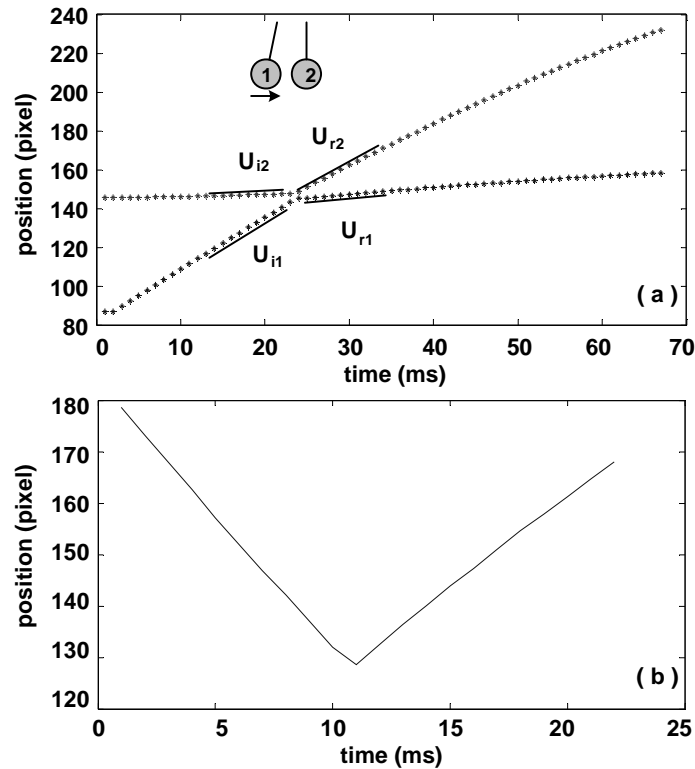


Figure 2.6. Time evolution of (a) the particle trajectories and (b) the distance between the sphere centers. For this collision, the impact and rebound velocities are $U_{i1} = 65.6$ mm/s, $U_{r1} = 3.6$ mm/s, $U_{i2} = 3.2$ mm/s, and $U_{r2} = 58.8$ mm/s.

2.3 Physical parameters

2.3.1 Coefficient of restitution in a liquid

Four velocities, U_{i1} , U_{i2} , U_{r1} and U_{r2} , are involved in a particle-particle binary collision rather than the two velocities, U_i and U_r , for particle-wall collisions. Therefore a new definition of the coefficient of restitution is required. Together with the particle Stokes number defined in equation (2.1), the coefficient of restitution, calculated by equation (2.3), successfully characterizes the particle-wall immersed collision. Therefore, it is reasonable to adopt the conventional definition:

$$e \equiv -\frac{U_{r1} - U_{r2}}{U_{i1} - U_{i2}}, \quad (2.4)$$

for a binary collision as a measure of the momentum and thus the energy loss. Equation (2.4) was first proposed by Newton as a kinematical collision model based on his experiments of dry collisions between solid objects. A second collision model was proposed by Poisson who hypothesized that a collision is composed of a compression phase followed by a restitution phase.

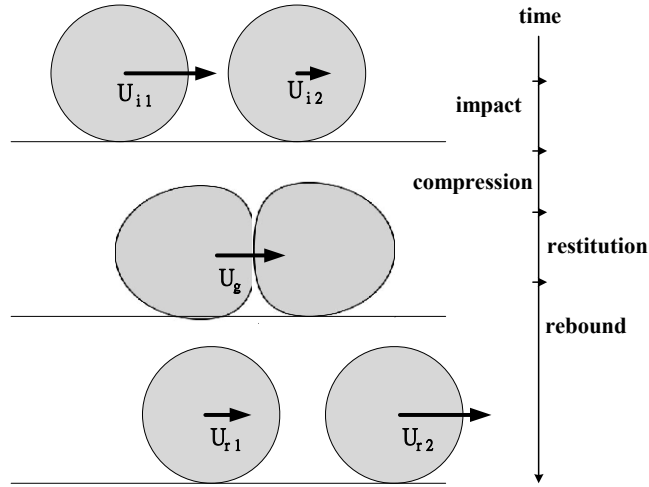


Figure 2.7. Schematic collision process.

As shown in figure 2.7, the impact sphere, of mass m_1 , impacts the target sphere, of mass m_2 and velocity U_{i2} , at a velocity U_{i1} . During the compression phase, the contact force rises and deforms both spheres and the two moves together at the group velocity:

$$U_{G0} = \frac{m_1 U_{i1} + m_2 U_{i2}}{m_1 + m_2}, \quad (2.5)$$

which is derived from the conservation of linear momentum. The compression process affects the momentum of each sphere as:

$$\begin{cases} m_1 U_{i1} - P_c = m_1 U_{G0} \\ m_2 U_{i2} + P_c = m_2 U_{G0}, \end{cases} \quad (2.6)$$

where the compression impulse, $P_c = \int_0^{\tau_c} F_c(\tau) d\tau$, is the time integration of the compression force up to time τ_c . The compression force $F_c(t)$ and duration τ_c can be found by considering the stress distribution in both spheres and is a function of the material elasticity and the relative impact velocity. Hertz contact theory can be applied as

the first approximation, assuming a fully elastic deformation. However, without explicitly evaluating the integral, the contact impulse can be found by combining equations (2.5) and (2.6) to get:

$$P_c = \frac{m_1 m_2}{m_1 + m_2} (U_{i1} - U_{i2}).$$

Similar expressions for the restitution phase are readily found as:

$$\begin{cases} m_1 U_{G0} - P_r = m_1 U_{r1} \\ m_2 U_{G0} + P_r = m_2 U_{r2} \end{cases},$$

involving three unknowns, $P_r = \int_0^{\tau_r} F_r(\tau) d\tau$, U_{r1} , and U_{r2} , with only two equations.

Poisson's hypothesis of $P_r = e P_c$ can be used as the third equation to determine the post-

collision velocities as: $U_{r1} = U_{i1} - (1+e) \frac{m_2}{m_1 + m_2} (U_{i1} - U_{i2})$ and

$$U_{r2} = U_{i2} + (1+e) \frac{m_1}{m_1 + m_2} (U_{i1} - U_{i2}).$$

The coefficient of restitution is calculated as the ratio of restitution to compression impulse and can be expressed as the ratio of relative velocities before and after the collision:

$$e = \frac{P_r}{P_c} = - \frac{U_{r1} - U_{r2}}{U_{i1} - U_{i2}}. \quad (2.7)$$

Equation (2.7) is equivalent to Newton's empirical expression in equation (2.4) for a normal collision with no friction or rotation that imparts tangential forces on the particles.

2.3.2 Binary Stokes number

For a general binary immersed collision between objects of similar or dissimilar materials, sizes, and impact velocities, a *binary Stokes number* is proposed by considering the hydrodynamic effects on the two approaching spheres. Following Poisson's hypothesis, an immersed collision is also decomposed into a compression and a restitution phase. The momentum change of the impact sphere, including the hydrodynamic effects, is written as:

$$m_1 U_{i1} - H_{c1} - P_c = m_1 U_G, \quad (2.8a)$$

with some intermediate group velocity U_G . The new term $H_{c1} = \int_0^{\tau_{fc}} h_{c1}(\tau) d\tau$ estimates the hydrodynamic impulse by integrating the total fluid force $h_{c1}(t)$ up to time τ_{fc} . The spheres make contact at τ_{fc} , initiating the physical compression process with a solid compression force. The compression force is integrated from τ_{fc} to $\tau_{fc} + \tau_c$ to determine the solid impulse P_c . After the *general* compression phase terminates at time $\tau_{fc} + \tau_c$, the *general* restitution phase commences and a momentum balance equation can be found for the impact sphere as:

$$m_1 U_G - H_{r1} - P_r = m_1 U_{r1}. \quad (2.8b)$$

The sphere is decelerated by the fluid force $h_{r1}(t)$, yielding the hydrodynamic rebound impulse $H_{r1} = \int_0^{\tau_{f2}} h_{r1}(\tau) d\tau$. A second set of equations can be derived for the target sphere with hydrodynamic impulses H_{c2} and H_{r2} as:

$$m_2 U_{i2} - H_{c2} + P_c = m_2 U_g, \quad (2.8c)$$

$$m_2 U_g - H_{r2} + P_r = m_2 U_{r2}. \quad (2.8d)$$

For both spheres, the solid impulses P_c and P_r are identical due to the mutual surface contact. However, the hydrodynamic impulses are in general different, owing to the different particle sizes, solid densities, particle velocities, and ambient flows.

Using equations (2.8a)–(2.8d), the coefficient of restitution can be manipulated into:

$$\begin{aligned} e &= -\frac{U_{r1} - U_{r2}}{U_{i1} - U_{i2}} = -\frac{\left(U_g - \frac{H_{r1}}{m_1} - \frac{P_r}{m_1}\right) - \left(U_g - \frac{H_{r2}}{m_2} + \frac{P_r}{m_2}\right)}{\left(U_g + \frac{H_{c1}}{m_1} + \frac{P_c}{m_1}\right) - \left(U_g + \frac{H_{c2}}{m_2} - \frac{P_r}{m_2}\right)} = \frac{\frac{P_r}{m^*} + \left(\frac{H_{r1}}{m_1} - \frac{H_{r2}}{m_2}\right)}{\frac{P_r}{m^*} + \left(\frac{H_{c1}}{m_1} - \frac{H_{c2}}{m_2}\right)} \\ &= \frac{P_r + m^* (\Delta U_{r1} - \Delta U_{r2})_H}{P_c + m^* (\Delta U_{i1} - \Delta U_{i2})_H}, \end{aligned}$$

where $m^* = (1/m_1 + 1/m_2)^{-1}$ is defined as the *reduced mass* of the particle system. The hydrodynamic effects are grouped into the parentheses subscripted “H.” For a dry binary collision, there is no velocity change due to the fluid force, which corresponds to Poisson’s hypothesis for dry coefficient of restitution $P_r = e P_c$. For a particle-wall immersed collision, where $\Delta U_{r2} = \Delta U_{i2} = 0$ and $m^* = m_p$, the coefficient of restitution,

$$e = -\frac{U_{r1}}{U_{i1}} = \frac{P_r + (m_p \Delta U_{r1})_H}{P_c + (m_p \Delta U_{i1})_H} = \frac{P_r^*}{P_c^*},$$

can be interpreted as the ratio of the generalized restitution and compression impulses, P_c^* and P_r^* . The term $(m_p \Delta U_{i1})_H$ represents the additional momentum change

of the impact sphere due to the action of the hydrodynamic impulses. Therefore, for a sphere traveling at higher particle Stokes numbers, the momentum change $(m_p \Delta U_{i1})_H$ will be smaller, resulting in a higher value of e . This correlation suggests a non-simple dependence of the coefficient of restitution on St .

For a binary collision, the generalized impulses include the momentum change of the target sphere and the resulting expression is:

$$e = \frac{P_r^*}{P_c^*} \equiv \frac{P_r + m^* (\Delta U_{r1} - \Delta U_{r2})_H}{P_c + m^* (\Delta U_{i1} - \Delta U_{i2})_H}.$$

Analogous to a particle-on-wall collision, the second term in the denominator represents the total momentum change in the particle system upon approaching and is assumed to be the controlling parameter for the total momentum loss during a collision. Following the correlation between $(m_p \Delta U_{i1})_H$ and St , a binary particle Stokes number is proposed as:

$$St_B = \frac{m^* U_{rel}}{6\pi\mu a^{*2}}. \quad (2.9)$$

The particle system possesses reduced mass m^* and a *reduced radius* $a^* = (1/a_1 + 1/a_2)^{-1}$, while $U_{rel} = U_{i1} - U_{i2}$ is the initial relative velocity between the two spheres. The numerator of equation (2.9) provides a measure of available momentum in the solid phases that sustains the particle motion through the liquid and is identical to the original definition given in Davis, et al. (1986). Their definition was obtained upon solving the equation of motion for two approaching spheres whose motion is decelerated by the lubrication force.

The denominator estimates the total viscous dissipation by multiplying the effective

viscous force, $6\pi\mu a^*U_{rel}$, with a forcing duration a^*/U_{rel} . For a particle-wall collision, the time interval is a/U_i and the original particle Stokes number, equation (2.1), is recovered using $m^* = m_1$, $U_{rel} = U_i$, and the viscous force $6\pi\mu aU_i$. For a binary collision between spheres of *equal size*, as used in the current experiments, the binary Stokes number can be manipulated into:

$$St_B = \frac{2}{9} \frac{\rho_p^*}{\rho_f} \text{Re}_{rel},$$

with a reduced density $\rho_p^* = (1/\rho_1 + 1/\rho_2)^{-1}$ and a Reynolds number $\text{Re}_{rel} = 2aU_{rel}/\nu_f$ based on relative velocity between the particles. Similarly, equation (2.1) can be written into $St = (\rho_p/\rho_f)\text{Re}/9$, which is widely used in the two-phase flow literature.

2.4 Normal collisions between spheres of identical sizes

2.4.1 Identical spheres

The spheres used in the experiments were all 12.7 mm in diameter and were made of steel, glass, or Delrin. The effective coefficient of restitution for collisions between identical spheres is plotted versus the binary Stokes number in figure 2.8. A monotonic decrease in e with decreasing binary Stokes numbers is observed. A critical binary Stokes number for zero coefficient of restitution, $St_{BC} = 2 \sim 8$, was found, indicating either a fully stopped impact sphere before reaching the target or a zero relative velocity after collision. For some collisions in the most viscous liquid investigated in this study ($\nu_f \approx 4.3 \times 10^{-5} \text{ m}^2/\text{s}$), the two spheres moved as a group after the impact, yielding zero

restitution. The target sphere did not accumulate sufficient inertia to overcome the hydrodynamic forces and thus was unable to escape from the impact sphere. The critical binary Stokes number is lower than the value for particle-wall collisions ($St_c = 7 \sim 12$), which may result from the mobility for the target particle.

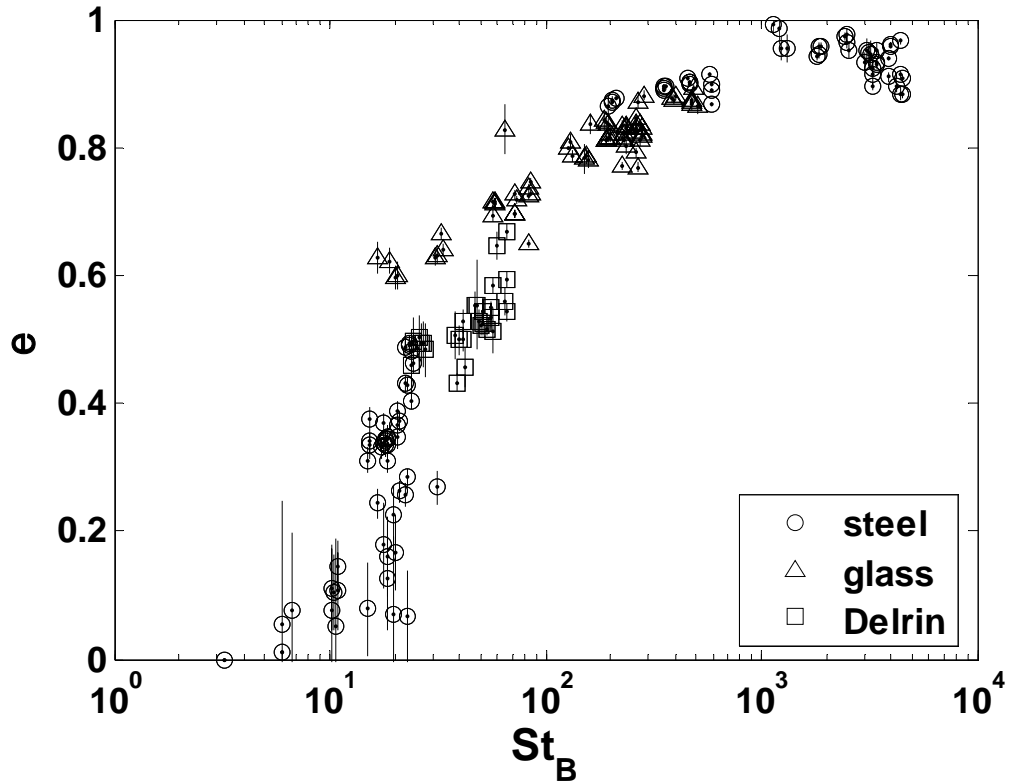


Figure 2.8. Effective coefficient of restitution as a function of binary Stokes number for immersed normal collisions between identical spheres ($D = 12.7$ mm). The pair material is steel (\square), glass (\circ), and Delrin (Δ) respectively. The error bars estimate the uncertainty in calculating the sphere velocities.

2.4.2 Dissimilar spheres

Within the same range of liquid viscosities, experiments involving collisions between spheres of identical size (12.7 mm) but dissimilar materials were also conducted. As shown in figure 2.9, a similar trend is observed of a monotonic decrease of coefficient of restitution with diminishing binary Stokes number.

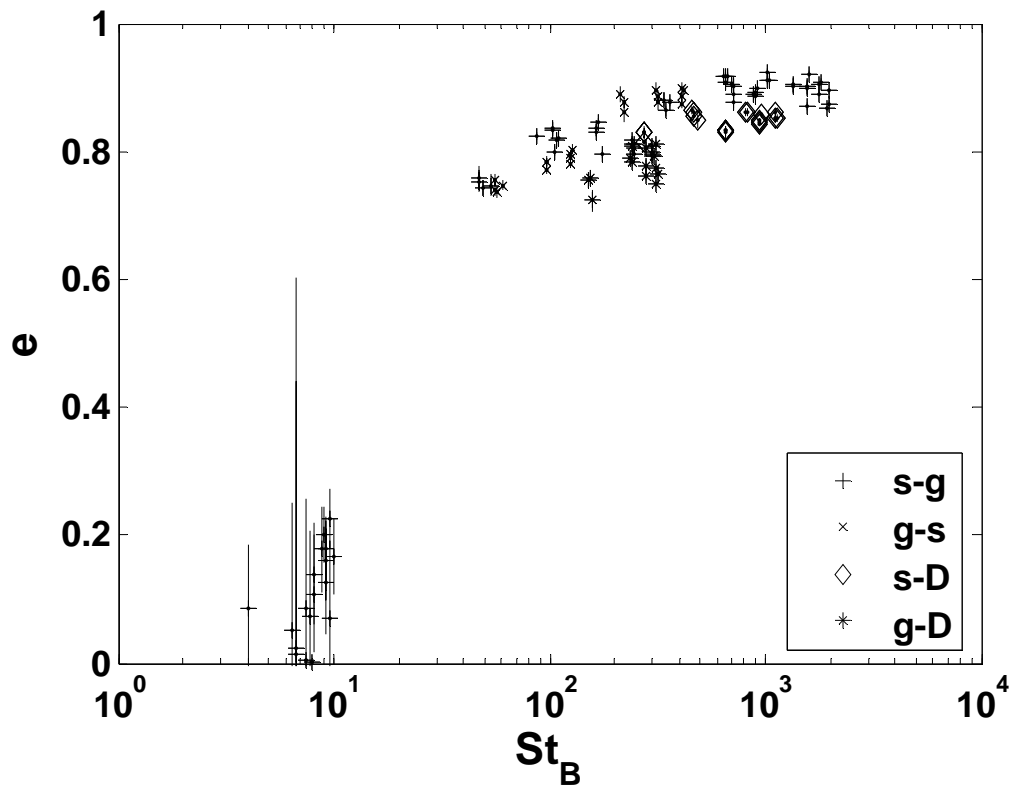


Figure 2.9. Effective coefficient of restitution as a function of binary Stokes number for immersed normal collisions between dissimilar spheres. The sphere material is abbreviated by “s,” “g,” and “d” for steel, glass, and Delrin. For the legend character pair, the impact sphere is represented with its material abbreviation followed by the target material abbreviation. Therefore, steel-on-glass collisions (\times) are denoted by the pair “s-g,” etc.

In figure 2.10, the collision data for dissimilar spheres are compared with the results for identical pairs. The general agreement between the two data sets supports the use of the coefficient of restitution $e = -(U_{i1} - U_{i2}) / (U_{r1} - U_{r2})$ and the binary Stokes number $St_B = m_p^* U_{rel} / 6\pi\mu a^{*2}$ to characterize the general binary immersed collision while a target sphere, initially stationary, is free to move upon impact.

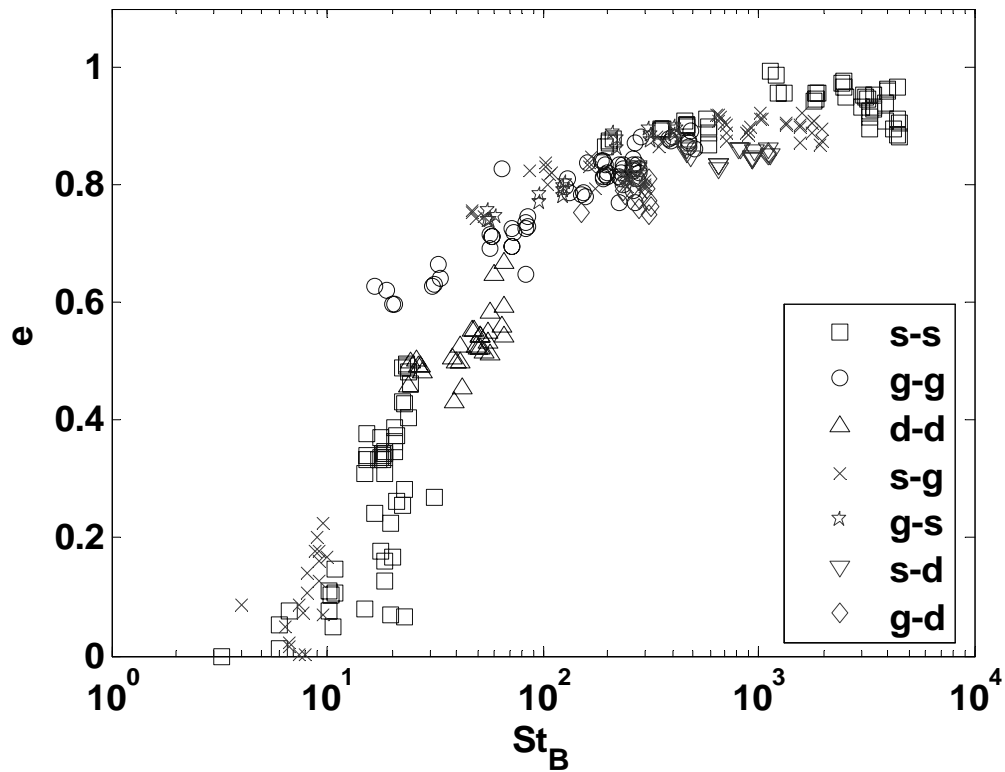


Figure 2.10. Immersed inter-particle normal collisions between identical and dissimilar spheres.

To summarize, Poisson's impulse hypothesis, relating the compression and restitution process with the coefficient of restitution, was applied to estimate the total momentum change upon impact for an immersed binary collision. Both impulses were extended to include the hydrodynamic forces. The coefficient of restitution thus serves as a measure of the momentum loss during an immersed collision between both similar and dissimilar

particles. The generalized compression impulse suggests a definition of the binary Stokes number for the pair and is shown to be well correlated with the coefficient of restitution.

2.4.3 Comparison with particle-wall collision

Furthermore, the inter-particle collision data are compared with the results of fully immersed collisions between a sphere and a stationary wall. As shown in figure 2.11, regardless of the target size and mobility, both dynamic collision process can be characterized by e and St_B , with the ambient fluid effects on the particle motion being imbedded in St_B . The effective coefficient of restitution for an immersed inter-particle collision is slightly greater than the value for particle-wall collision, which can be attributed to the mobility of the target sphere. Moreover, boundary layers develop along the solid surfaces when the interstitial liquid is squeezed out upon the approach, a layer of which undergoes strong viscous dissipation consuming the momentum of the impact sphere. Such dissipation becomes weaker when the target is of finite size because of a smaller boundary layer. Thus a slightly greater e for particle-particle immersed collisions is observed.

The inter-particle collision data revealed a smaller critical binary Stokes number than the results of particle-wall collision, a reduction of which might be attributed to the mobility of the target particle. It will be shown in chapter 3 that the presence of the target increases the hydrodynamic forces with decreasing interstitial distance. The augmentation is smaller for a smaller target due to an easier flow passage around the object and less particle inertia is required to sustain a motion through the liquids upon approaching and receding. Therefore, for collisions on a target of finite size, zero restitution is observed at smaller binary Stokes number than the critical values found for on-wall impacts.

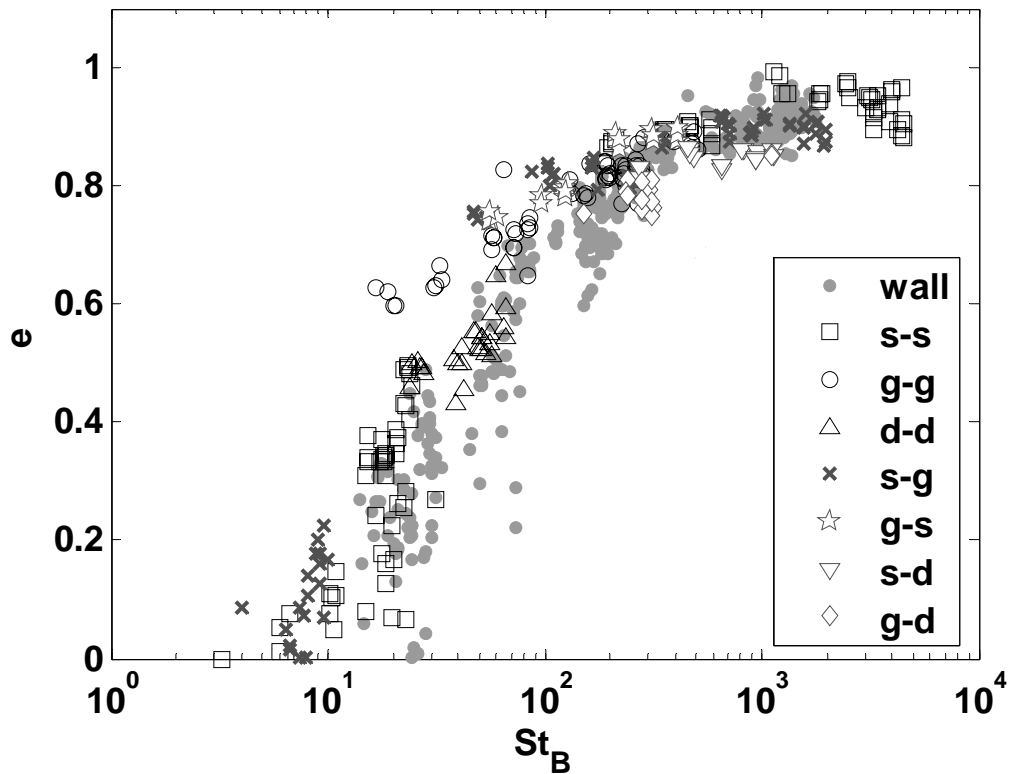


Figure 2.11. Comparison of the inter-particle and the particle-wall immersed collisions.

For $St_B \approx 20-40$, the glass-on-glass collisions resulted in higher restitution than the collisions involving other materials. This high restitution might be attributed to a large rebound distance between two glass surfaces than between other surfaces, which results in smaller hydrodynamic forces upon contact. Such an inverse dependence of the total fluid force on the gap width will be examined in chapter 3. The glass spheres used in the experiments have higher surface roughness than the steel ball bearings. Though the Delrin particle has an even rougher surface, the stiffer glass asperity deforms less. Therefore, as an overall consequence, two glass surfaces rebound at a greater separation yielding smaller hydrodynamic forces; less kinetic energy is dissipated in the fluids for the glass pair and hence a greater restitution is found. Similarly, collisions between steel and glass spheres resulted in higher restitution than between other materials at

around $St_B \approx 50-130$, which is illustrated in figure 2.12. A linear-linear plot is used for this interested regime of St_B . The interplay of the surface elements could also explain the higher restitution for steel-on-glass collisions at around $St_B \approx 10$ than for steel-on-steel impacts. However, the enhancement is less pronounced due to smaller particle inertia. For collisions at such low binary Stokes numbers, the hydrodynamic forces dominate the particle motion, diminishing the surface property effects on the rebound.

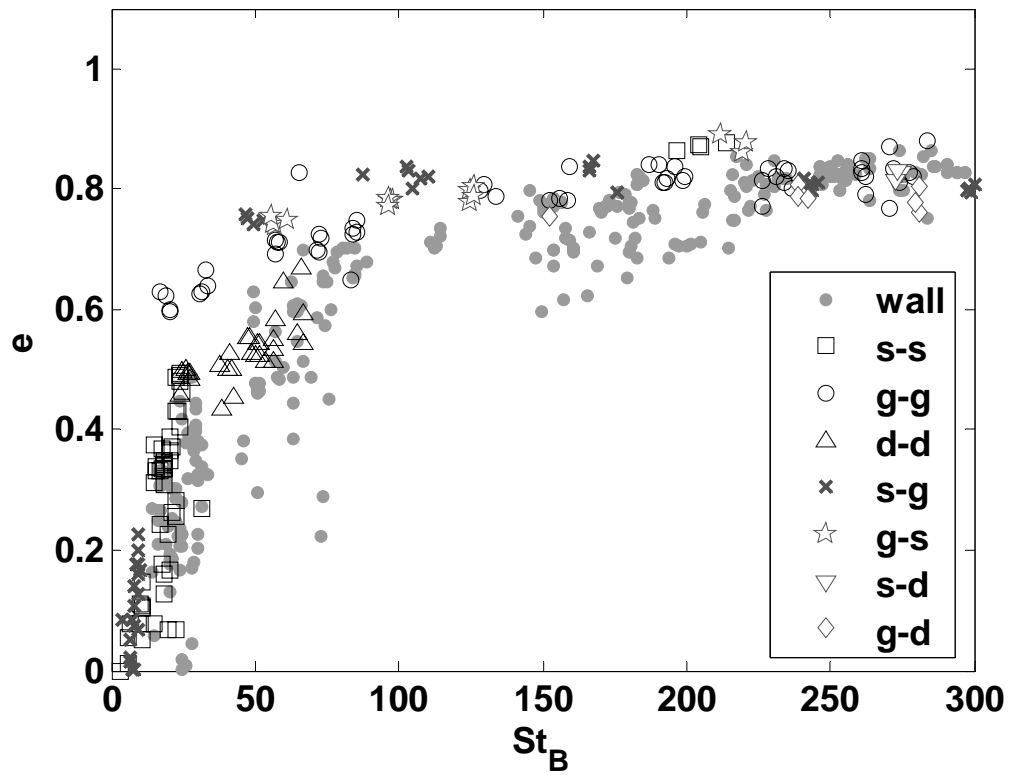


Figure 2.12. An enhanced restitution due to rebounds at a greater separation that occurs between particles of high and stiff asperities, such as glass spheres.

2.5 Particle motion with zero coefficient of restitution

In some immersed collisions, particularly those involving the most viscous liquid in the current experiments, the target sphere was observed to move, *prior to contact*, in the same direction as the incoming sphere. The momentum of the impact sphere is transmitted to the target by the pressure front built up in the incompressible interstitial liquid layer.

For a collision between two glass spheres at $St_B \sim 2$, the target motion was noticeable when the impact sphere was about one-fifth of a sphere diameter, as may be seen in figure 2.13. For this particular case, both spheres had diameter of 12.7 mm. Over the investigated duration of 500 ms, the target moved about 0.07 D, yielding a velocity of about 1.8 mm/s before the two surfaces touched. The liquid was so viscous in this case that the impact motion nearly ceased upon touching. Following the impact, the two seemed suspended together in the liquid and were slowly brought down to the lowest pendulum position by gravity.

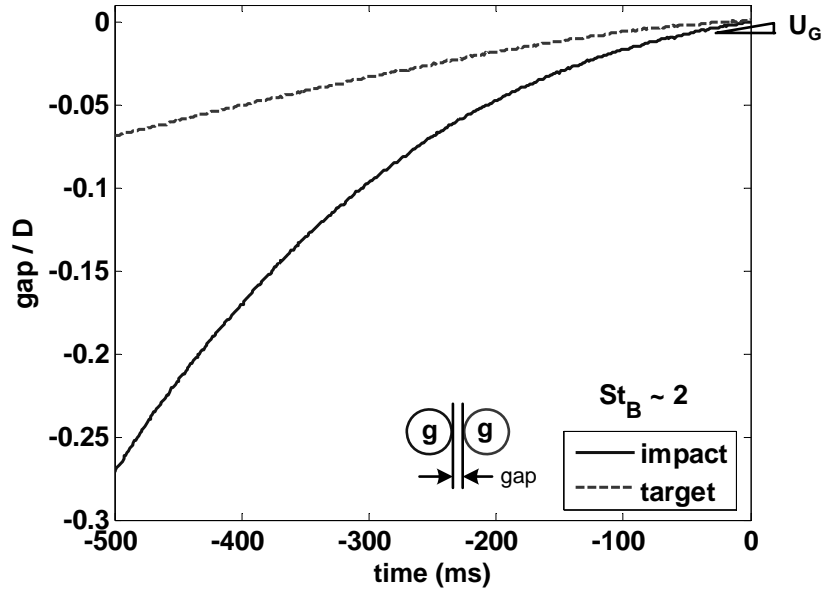


Figure 2.13. Time evolution of the interstitial gap for a glass-on-glass collision that results in zero restitution due to the nearly stopped impact sphere motion. Both glass spheres are 12.7 mm in diameter.

Unlike a particle-wall immersed collision where zero restitution results from either a fully stopped sphere upon contact or one that possesses insufficient rebound inertia for further reverse motion, an inter-particle collision can retain a post-collision group motion while a zero restitution coefficient is determined by equation (2.4). As depicted in figures 2.14(a) and 2.14(b), the target was accelerated from a non-zero velocity by the collision impulse. However, the impulse did not supply sufficient inertia for the target particle to overcome the hydrodynamic forces to separate further from the impact sphere. As a consequence, the two moved at a group velocity U_G that is always lower than the dry group

velocity, $U_{G0} = \frac{m_1 U_{i1} + m_2 U_{i2}}{m_1 + m_2}$ from equation (2.5), due to the surrounding fluid effects. In

these figures, zero time is located when the gap drops to zero.

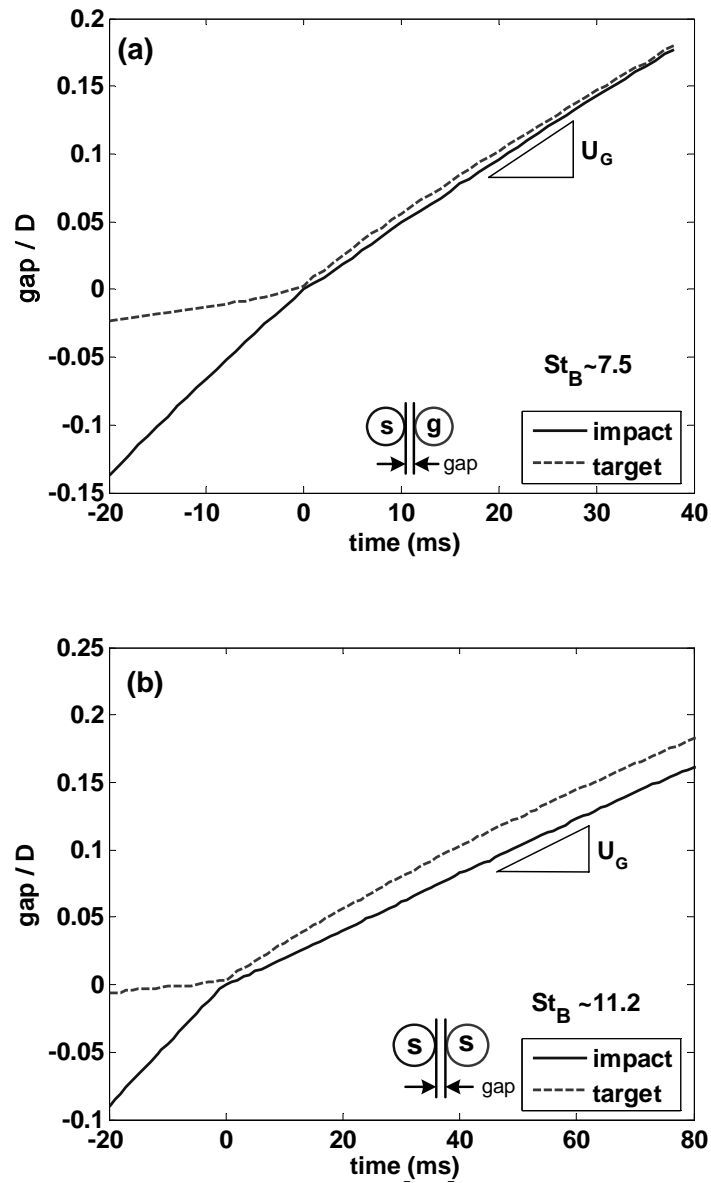


Figure 2.14. Time evolution of the interstitial gap for impacts that result in zero restitution but non-zero particle motion after collision: (a) steel-on-glass and (b) steel-on-steel collisions. All the spheres are 12.7 mm in diameter.

If the group velocity in liquid, U_G , is scaled by the dry group velocity, U_{G0} , the *group efficiency number*,

$$e_G = \frac{U_G}{U_{G0}},$$

serves as an index of how efficient the pair particles move together under hydrodynamic forces. In figure 2.15, the binary Stokes number St_B is used to estimate the total fluid force, as in the previous sections. When e_G is plotted against St_B , a decline in the group efficiency number is observed when the binary Stokes number drops below 2, at which value the viscous force surpasses the solid inertia and severely dissipates the group motion. Since this type of group motion was rarely observed within the current impact conditions, further experiments would be needed for a quantitative description.

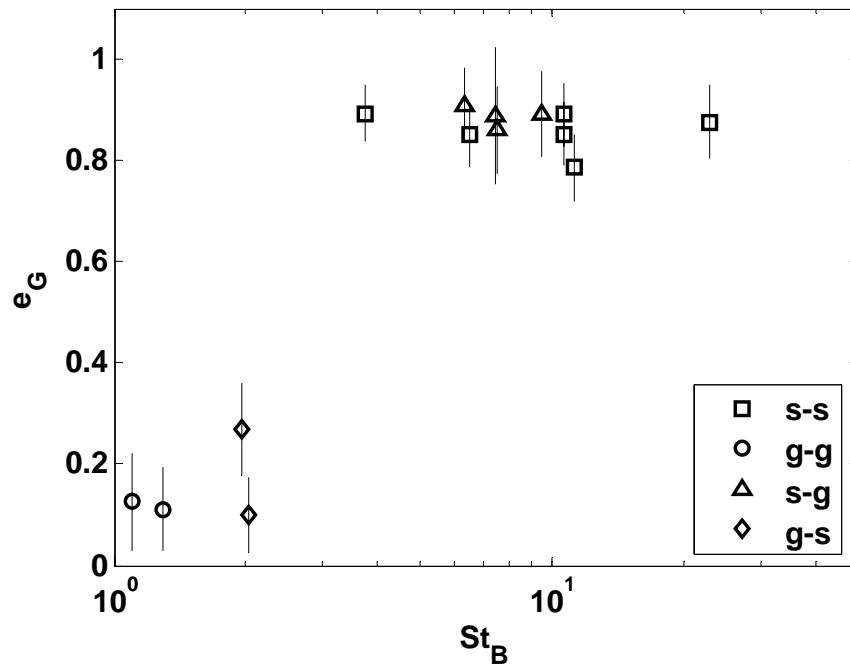


Figure 2.15. Group efficiency number with respect to the binary Stokes number. Error-bars represent the uncertainty in calculating the velocity of each sphere.

2.6 Summary

To summarize, Poisson's impulse hypothesis that relates the compression and restitution process with the coefficient of restitution was used to estimate the total momentum loss during an immersed collision, between similar and dissimilar particles. The generalized compression impulse suggests a new definition of pertinent particle Stokes number for an inter-particle immersed collision—a binary Stokes number, St_B . This number is shown to be well correlated with the effective coefficient of restitution. While the effective coefficient of restitution, e , measures the resultant energy loss upon collision, the ambient fluid effects are imbedded in the binary Stokes number. Despite the target size and mobility, the inter-particle collision data follow a similar trend to the results of particle-wall collisions. The general agreement supports the usage of e and St_B to characterize such a rapid dynamic process.

Interesting phenomenon, such as pre-collision target motion and a group motion of the particle pair, was also observed in the experiments. The target mobility and the incompressible surrounding liquid are essential for such findings, which have never been reported from the on-wall immersed collision experiments and can never occur in a dry medium.

Chapter 3

Wall Effects on the Hydrodynamic Forces

In chapter 2, a general correlation between the effective coefficient of restitution and the binary Stokes number was found for both inter-particle and particle-wall immersed collision. The monotonic decrease in the effective coefficient of restitution with diminishing binary Stokes number is expected to reveal the underlying physics of an immersed collision. A model that reproduces the correlation would be of particular use. The degree of collapse of the two data sets suggests the modeling of the sphere-wall collision as a first attempt to address how a second solid boundary affects the particle approaching motion. In order to describe the sphere motion in the proximity of wall, the conventional hydrodynamic forces, developed for the motion of a single sphere in an unbounded fluid domain, require modifications. The three forces examined in this chapter are: the steady viscous force, the added mass force, and the Basset history force.

3.1 Background

Stokes (1845) derived an expression for the force exerted on a steadily moving solid sphere in an unbounded viscous incompressible fluid. This relation now bears his name—Stokes' drag law. Besides the steady viscous drag, the added mass force that accounts for the unsteadiness in the motion of an object in a fluid is also important. A lesser known

history force, which depends on the development of an unsteady boundary layer, was derived by Basset (1888) and Boussinesq (1885) independently for the force on a sphere that oscillates in the Stokes flow regime. Since then, extensive work has been done to extend these analytical expressions for a broader range of flow conditions. A thorough review can be found in Michaelides (1997).

The problem of the approach of a solid sphere towards a wall or another sphere in a viscous fluid forms an entire field of study. Brenner (1961) developed a correction term to Stokes' drag for a rigid sphere with steady motion towards a wall at small Reynolds number. This value increases with diminishing gap width and converges to the classical lubrication theory when the gap drops to zero. Cox and Brenner (1967) applied a perturbation technique to extend this finding to sphere motion at higher Reynolds number where the liquid inertia becomes non-negligible. The new expression requires only a small gap Reynolds number, $Re_g = 2\delta U/\nu_f$, and can be used for particle motion beyond Stokes regime. As for the added mass force, the presence of the wall introduces to the flow a new boundary condition that can be satisfied using the image method. The procedure is outlined in Lamb (1932) and Milne-Thomson (1968) and modifications on the total fluid kinetic energy can be expressed as an infinite sum that also grows with decreasing interstitial gap. The infinite series through which the relation is presented is cumbersome and difficult to implement in a computation. Thus a simplified expression is developed in section 3.3 followed by the modifications of the history force.

3.2 Viscous drag

3.2.1 Moderate Reynolds number effects

When the sphere is far away from wall, the viscous drag is calculated as:

$$F_D = -6\pi\mu aU \phi(Re), \quad (3.1)$$

where the correction on the Stokes' drag, $\phi(Re)$, accounts for higher Reynolds number effects and is a function of the particle Reynolds number, $Re = 2aU/\nu_f$. It can be related to the steady state drag coefficient, $C_D(Re)$, by:

$$\phi(Re) = \frac{ReC_D(Re)}{24}. \quad (3.2)$$

Through out this work, the expression of $\phi(Re) = 1 + 0.15Re^{0.687}$ is used for $Re < 800$ (Clift, Grace, and Weber 1978). When the sphere moves close to the wall, the classical lubrication theory predicts a force that increases as the inverse of the gap width—a singular behavior not captured by equation (3.1).

3.2.2 Wall effects on the steady viscous drag

When the sphere moves closer to the wall, the small gap width ensures a Stokes' flow between the solid surfaces. When the solid sphere moves at constant speed perpendicularly towards a wall at U , Brenner (1961) solved the quasi-steady Stokes' equation and found the viscous drag force as:

$$F_D = -6\pi\mu a U \lambda(\delta^*),$$

where the non-dimensional gap, $\delta^* = \delta/a$, is scaled by the sphere radius a . The correction factor, $\lambda(\delta^*)$, takes the form of an infinite series:

$$\lambda(\delta^*) = \frac{4}{3} \sinh \alpha \sum_{n=1}^{\infty} \frac{n(n+1)}{(2n-1)(2n+3)} \left[\frac{2 \sinh(2n+1)\alpha + (2n+1) \sinh 2\alpha}{4 \sinh^2(n+\frac{1}{2})\alpha - (2n+1)^2 \sinh^2 \alpha} - 1 \right], \quad (3.3)$$

where $\alpha(\delta^*) = \cosh^{-1}(\delta^* + 1)$. Cox and Brenner (1967) extended equation (3.3) for flow at higher Reynolds number, where the convective acceleration of the interstitial liquid becomes important and required only small gap Reynolds number $Re = 2\delta U/\nu_f$. The new wall correction term depends on both the gap width and the particle Reynolds number and is given by:

$$\lambda(\delta^*, Re) \approx \frac{1}{\delta^*} \left[1 + \frac{1}{5} (1 \pm \frac{1}{4} Re) \delta^* \log \frac{1}{\delta^*} \right]. \quad (3.4)$$

Cox and Brenner's sign convention is adopted. For an approaching sphere, a plus sign in front of the particle Reynolds number is used and it is switched to a negative when the sphere rebounds from the wall. The wall-modified viscous drag can thus be written as:

$$F_D = -6\pi\mu a |U| \lambda(\delta^*, Re). \quad (3.5)$$

Since the viscous drag is a consequence of vorticity diffusion, a smooth transition from equation (3.1) to equation (3.5) is expected. Thus the two equations are matched at distance where the two corrections, $\phi(Re)$ and $\lambda(\delta^*, Re)$, converge to a single value.

3.3 Added mass force

Since the motion of the approaching sphere is intrinsically unsteady, the effects of the added mass and the history forces must be included. For an unsteady sphere moving in a viscous quiescent fluid that extends to infinity, various simulations (Chang and Maxey 1995; Kim, Elghobashi, and Sirignano 1998; Bagchi and Balachandar 2003) have revealed the presence of an unsteady force that can be described by the added mass force. Once the particle Reynolds number exceeds the Stokes flow regime, the vorticity is confined to the boundary layer and has little effect on the upstream flow. Therefore potential flow is expected to describe the upstream flow motion, whether the wall is present or not. However, the conventional potential flow function does not account for the new boundary condition at the wall. Thus the wall effects are considered as follows.

3.3.1 Added mass force in the presence of a wall

When a solid sphere moves towards a wall at velocity $U(t)$, the total kinetic energy in the fluid phase can be calculated as:

$$T = \frac{1}{4} m_f U(t)^2 \left[1 + 3 \sum_{n=1}^{\infty} \left(\frac{\mu_n}{\mu_0} \right) \right] = \frac{1}{4} m_f U(t)^2 [1 + 3W(\delta^*)], \quad (3.6)$$

where $m_f = 4/3 \pi a^3 \rho_f$ is the mass of liquid displaced by the sphere (Milne-Thomson 1968). In order to satisfy the boundary condition of no penetrating flow at the wall, a series of dipole images are placed across the wall, resulting in the infinite sum $\sum_{n=1}^{\infty} \left(\frac{\mu_n}{\mu_0} \right)$

in equation (3.6). The successive terms are $\mu_0 = \frac{1}{2}Ua^3$, $\mu_1 = \mu_0 (p_1/q_1)^3$,
 $\mu_2 = \mu_1 (p_2/q_2)^3$, \dots , where $\frac{p_1}{q_1} = \frac{a}{2h}$, $\frac{p_2}{q_2} = \frac{a}{2h - a^2/(2h)}$ are functions of sphere center-
to-wall distance $h = a(\delta^* + 1)$. A recurrence relation is given as $\mu_n = \mu_{n-1} (p_n/q_n)^3$
and $p_n/q_n = \frac{a}{2h - 2h - 2h - \dots} \frac{a^2}{2h - 2h - 2h - \dots} \frac{a^2}{2h - 2h - 2h - \dots}$ is the n th convergent to the continued fraction. This
infinite sum, $\sum_{n=1}^{\infty} \left(\frac{\mu_n}{\mu_0} \right)$, thus is solely a function of scaled interstitial gap, $\delta^* = h/a - 1$, and
will be denoted by $W(\delta^*)$ and referred as the *wall correction term* hereafter.

The time rate of change of the total kinetic energy in the fluid phase is used to calculate the work done by the moving sphere. Thus, the wall-modified added mass force on the sphere may be derived as:

$$F_{AM}(t, \delta^*) = -\frac{1}{U(t)} \frac{dT}{dt} = -\frac{1}{2} m_f [1 + 3W(\delta^*)] \frac{dU}{dt} - \frac{3}{4} m_f U \frac{dW(\delta^*)}{dt}. \quad (3.7)$$

The first term involving dU/dt on the right-hand side of equation (3.7) is similar to the conventional added mass force. However an extra fluid mass, $3W(\delta^*)$, that a sphere needs to expel when accelerating, is found. The second term that includes the time derivative of $W(\delta^*)$ may be manipulated into:

$$-\frac{3}{4} m_f U \frac{dW(\delta^*)}{dt} = \frac{3}{4} \frac{m_f}{a} U^2 \frac{dW}{d\delta^*}, \quad (3.8)$$

which can be interpreted as an unsteady opposing pressure force by analogy to the pressure term in Bernoulli's equation.

(a) Behavior of the wall correction term $W(\delta^*) = \sum_{n=1}^{\infty} \left(\frac{\mu_n}{\mu_0} \right)$

For a simpler expression, the dimensional distance between the sphere center and the wall, $h = \delta + a$, is used in this section instead of the interstitial gap. Since the consecutive terms of the infinite series, $\mu_n = \mu_{n-1} (p_n/q_n)^3$, are expressed in terms of continued fraction, (p_n/q_n) , further simplification is possible. The n th convergent to the continued fraction,

$$\frac{p_n}{q_n} = \frac{a}{2h - \frac{a^2}{2h - \frac{a^2}{\dots}}}$$

can be used to find a general relation between p_n s and q_n s as follows. Starting with $p_0 = 0$ and $q_0 = 1$, write:

$$\frac{p_1}{q_1} = \frac{a}{2h} = \frac{a}{2h - a(\frac{p_0}{q_0})} \text{ and } \frac{p_2}{q_2} = \frac{a}{2h - \frac{a^2}{2h}} = \frac{a}{2h - a(\frac{p_1}{q_1})},$$

by induction and a recurrence relation can thus be found as:

$$\frac{p_{n+1}}{q_{n+1}} = \frac{a}{2h - a(\frac{p_n}{q_n})} = \frac{aq_n}{2hq_n - ap_n}. \quad (3.9)$$

By equating the numerator and the denominator on both sides of equation (3.9), the following set of equations is obtained:

$$\begin{cases} p_{n+1} = aq_n \\ q_{n+1} = 2hq_n - ap_n \end{cases}. \quad (3.10)$$

An equation that governs the q_n s can be found after canceling the p_n terms in equation (3.10) as:

$$q_{n+1} - 2hq_n + a^2 q_{n-1} = 0. \quad (3.11)$$

The general solution of equation (3.11) can be shown to be:

$$q_n = A\alpha^n + B\beta^n. \quad (3.12)$$

The numbers, α and β , are the roots of the equivalent 2nd order equation $s^2 - 2hs + a^2 = 0$ and can be found readily as:

$$\alpha, \beta = h \pm \sqrt{h^2 - a^2}.$$

To solve for the unknown constants, A and B , in equation (3.12), the two relations, $q_0 = A + B = 1$ and $q_1 = A\alpha + B\beta = 2h = \alpha + \beta$, are applied, using equations (3.10) and (3.12) in addition to the first value of q_n . The unknown constants can be expressed in terms of α and β as $A = \alpha/(\alpha - \beta)$ and $B = -\beta/(\alpha - \beta)$. A general expression for p_n and q_n then follows:

$$\begin{cases} q_n = \frac{\alpha^{n+1} - \beta^{n+1}}{\alpha - \beta} \\ p_n = \sqrt{\alpha\beta} \frac{\alpha^n - \beta^n}{\alpha - \beta}. \end{cases}$$

The n th term in the wall correction term can now be expressed as:

$$\frac{\mu_n}{\mu_0} = \left(\frac{p_n}{q_n}\right)^3 \times \dots \times \left(\frac{p_2}{q_2}\right)^3 \left(\frac{p_1}{q_1}\right)^3 = \left(\frac{\alpha^* - \beta^*}{\alpha^{*n+1} - \beta^{*n+1}}\right)^3,$$

in terms of the scaled roots:

$$\begin{cases} \alpha^* = \alpha/a = h^* + \sqrt{h^{*2} - 1} \\ \beta^* = \beta/a = h^* - \sqrt{h^{*2} - 1}, \end{cases}$$

where the quantity, h^* , is the scaled center-to-wall distance $h^* = h/a = \delta^* + 1$. The wall correction term can be expressed as a function of the scaled interstitial gap δ^* :

$$W(\delta^*) = \sum_{n=1}^{\infty} \left(\frac{\alpha^* - \beta^*}{\alpha^{*n+1} - \beta^{*n+1}}\right)^3. \quad (3.13)$$

The advantage of using equation (3.13) instead of its original expression with the successive multiplication term, $\prod_{i=1}^n \left(\frac{p_i}{q_i}\right)^3$, resides in its explicit dependence on h^* and thus δ^* , which helps the analysis on the series convergence. Figure 3.1 shows the behavior of $W_N(\delta^*)$, which is the partial sum of the first N terms in equation (3.13). When compared to the numerical sum of the first 100 terms, $W_5(\delta^*) - W_7(\delta^*)$ show good convergence to the numerical sum even at small gaps.

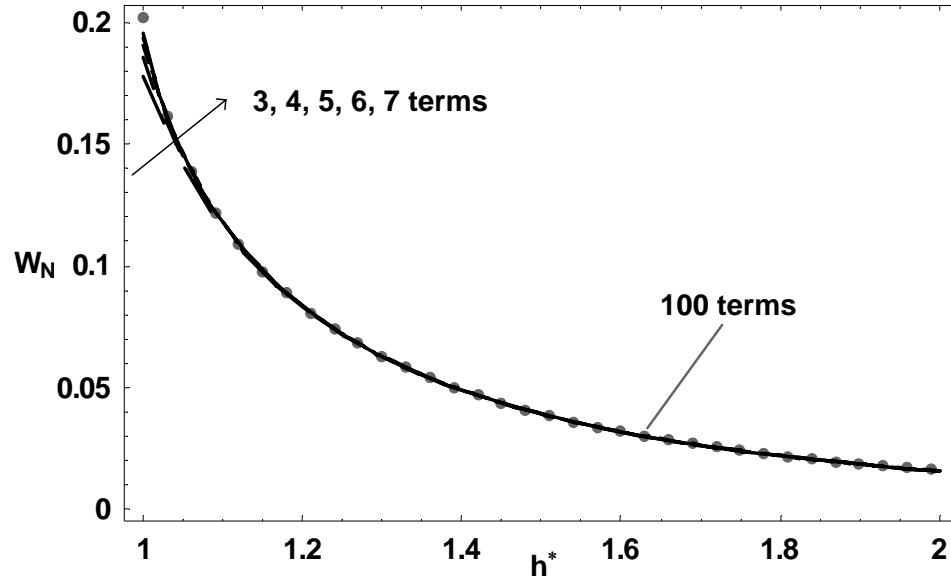


Figure 3.1. The collapse of the partial sum $W_N(\delta^*)$, $N = 3-7$, onto the numerical sum of 100 terms presented in the gray dots.

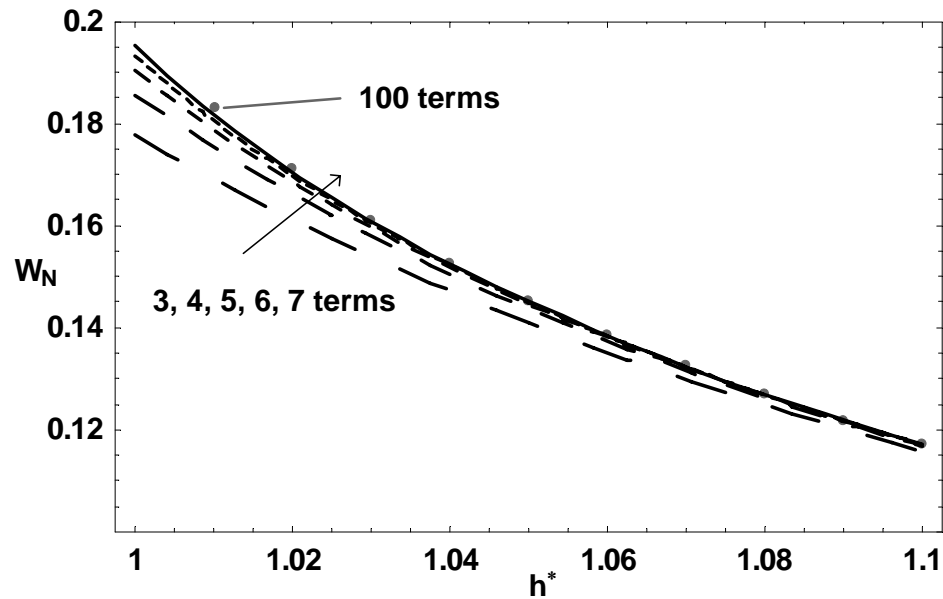


Figure 3.2. Discrepancy between $W_5(\delta^*)$ and $W_{100}(\delta^*)$ for $\delta^* < 0.02$.

As shown in figure 3.2, when the scaled gap δ^* drops below 0.02, the partial sum $W_7(\delta^*)$ yields a closer estimation to the numerical value $W_{100}(\delta^*)$. At $\delta^* = 0.02$,

$W_7(\delta^*) \approx 0.995 W_{100}(\delta^*)$ and $W_7(\delta^*) \approx 0.98 W_{100}(\delta^*)$ at $\delta^* = 0.002$. Therefore, the 7-term partial sum is used as an approximation for $W(\delta^*) = \sum_{n=1}^{\infty} \left(\frac{\mu_n}{\mu_0} \right)$ and its explicit form is

given as, with $h^* = \delta^* + 1$:

$$W_7(h^*) = \frac{1}{8h^{*3}} + \frac{1}{(4h^{*2} - 1)^3} + \frac{1}{(8h^{*3} - 4h^*)^3} + \frac{1}{(16h^{*4} - 12h^{*2} + 1)^3} + \frac{1}{(32h^{*5} - 32h^{*3} + 6h^*)^3} \\ + \frac{1}{(64h^{*6} - 80h^{*4} + 24h^{*2} - 1)^3} + \frac{1}{(128h^{*7} - 192h^{*5} + 80h^{*3} - 8h^*)^3} . \quad (3.14)$$

(b) Derivative of $W(\delta^*)$

The derivative of $W(\delta^*)$ with respect to δ^* is now sought in order to calculate the opposing pressure term in equation (3.8). Since $\left(\frac{\mu_n}{\mu_0} \right)$ is analytic for all δ^* , term-by-term

derivative is valid. The partial sum of the derivative $\frac{dW_N}{d\delta^*} = \sum_{n=1}^N \frac{d}{d\delta^*} \left(\frac{\mu_n}{\mu_0} \right)$ is evaluated

and the value with the first 40 terms agrees with that obtained using 100 terms, as shown in figure 3.3. Therefore, 40 terms were used for further approximation with reasonable computational time.

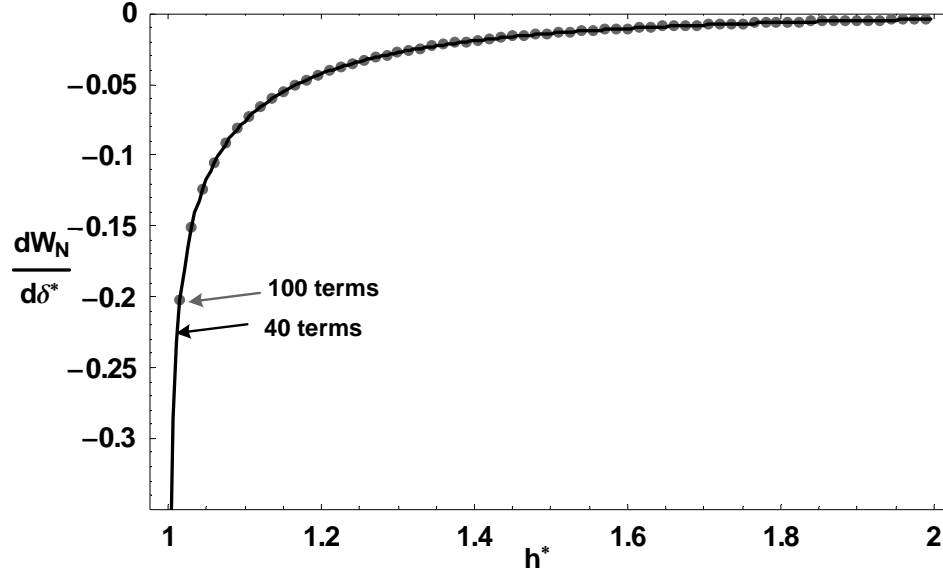


Figure 3.3. Derivative of the wall correction term is numerically evaluated using the first 40 and 100 terms.

When the 40-term numerical value is compared to the 3-term partial sum in figure 3.4, the 3-term approximation compares well with the numerical value for $h^* > 2$ where

$\left. \frac{dW_3}{d\delta^*} \right|_{h^*=2} = -0.004$ is only 0.003 % greater than the value of $\left. \frac{dW_{40}}{d\delta^*} \right|_{h^*=2}$. At a smaller

distance, $h^* = 1.2$, $\left. \frac{dW_3}{d\delta^*} \right|_{h^*=1.2} = -0.0418$ deviates from $\left. \frac{dW_{40}}{d\delta^*} \right|_{h^*=1.2} = -0.0424$ by 1.5% of

the value with 40 terms. Therefore, the derivative of the wall correction term is calculated with the first 3 terms for a gap width $\delta^* > 1$ as:

$$\begin{aligned} \frac{dW_3}{d\delta^*} = & \frac{1}{128h^{*2}(h^{*2}-1)(2h^{*2}-1)^3} - \frac{3h^*(4h^{*2}-3)}{2(h^{*2}-1)(4h^{*2}-1)^4} + \frac{h^*}{2(h^{*2}-1)(4h^{*2}-1)^3} \\ & - \frac{8h^{*4}-8h^{*2}+1}{128h^{*4}(h^{*2}-1)(2h^{*2}-1)^4} + \frac{1}{16h^{*2}(h^{*2}-1)} - \frac{(2h^{*2}-1)}{16h^{*4}(h^{*2}-1)}. \end{aligned} \quad (3.15a)$$

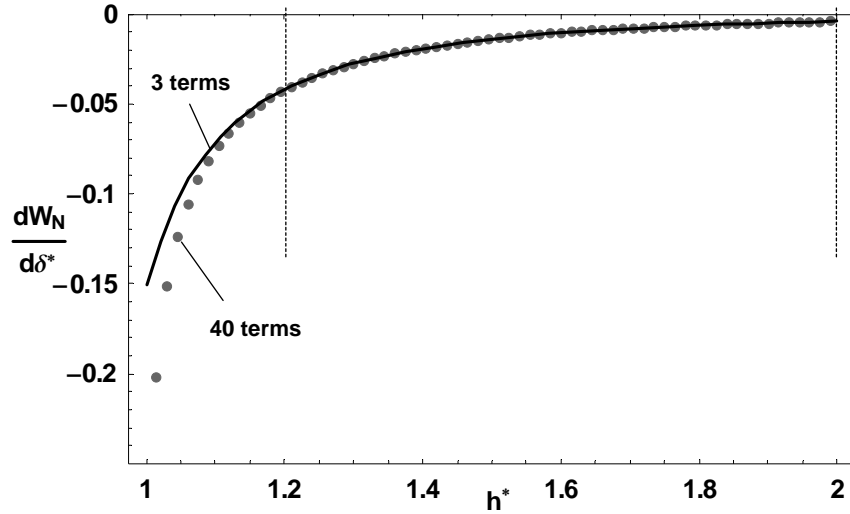


Figure 3.4. Comparison between the 40-term and 3-term partial sums.

At a position closer to the wall, the singularity at $\delta^* = 0$ dramatically slows down the series convergence, as shown in figure 3.5.

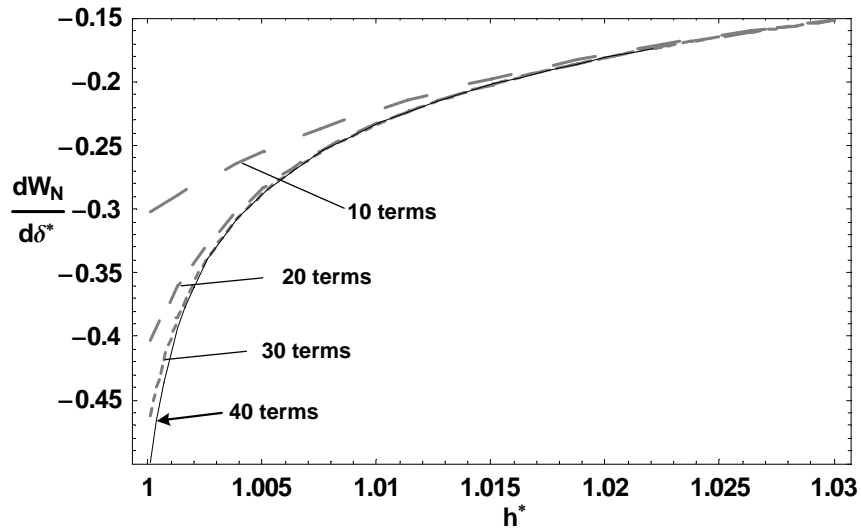


Figure 3.5. The 3-, 5-, and 7-term partial sums of the derivatives deviate from the 40-term partial sum when $\delta^* \rightarrow 0$.

Hence to approximate the derivative of the infinite series within reasonable computation time, the numerical partial sum of the first 40 terms was fitted with Mathematica® in the

least-square sense over $0.0001 \leq \delta^* \leq 1$ yielding:

$$\begin{aligned} \frac{dW_F}{d\delta^*} \approx & 0.241 - 2.3 \times 10^{-4} \delta^{*-1/2} - 0.311 \delta^{*1/2} + 6.6 \times 10^{-2} \delta^* \\ & + 9.8 \times 10^{-2} \log(\delta^*) - 2.06 \times 10^{-4} \log(\delta^*) \delta^{*-1/2}, \end{aligned} \quad (3.15b)$$

with a standard deviation of 9.24×10^{-4} . Since algebraic functions were insufficient to capture the series behavior, logarithm functions were used for a more compact fit.

To patch the two expressions, the numerical difference, $\left| \frac{dW_F}{d\delta^*} - \frac{dW_3}{d\delta^*} \right|$, between equations

(3.15a) and (3.15b), was estimated for the optimal position. Though the position $\delta^* = 1.99$ yielded the smallest difference of 2.8×10^{-9} , the position $\delta^* = 1.0$ with a difference of 2.54×10^{-6} will be used, with comparable accuracy to the computation in chapter 4, for a simpler formulation. To summarize, the derivative of the wall correction term was evaluated numerically and a hybrid expression in equation (3.15c) will be used throughout this work:

$$\left\{ \begin{aligned} \left(\frac{dW}{d\delta^*} \right)_{h^* > 2} &= \frac{1}{128h^{*2}(h^{*2}-1)(2h^{*2}-1)^3} - \frac{3h^*(4h^{*2}-3)}{2(h^{*2}-1)(4h^{*2}-1)^4} + \frac{h^*}{2(h^{*2}-1)(4h^{*2}-1)^3} \\ &\quad - \frac{8h^{*4}-8h^{*2}+1}{128h^{*4}(h^{*2}-1)(2h^{*2}-1)^4} + \frac{1}{16h^{*2}(h^{*2}-1)} - \frac{(2h^{*2}-1)}{16h^{*4}(h^{*2}-1)} \\ \left(\frac{dW}{d\delta^*} \right)_{h^* \leq 2} &= 0.24 - \frac{2.3 \times 10^{-4}}{(\delta^*)^{1/2}} - 0.31(\delta^*)^{1/2} + 6.6 \times 10^{-2}(\delta^*) \\ &\quad + 9.8 \times 10^{-2} \log(\delta^*) - \frac{2.06 \times 10^{-4} \log(\delta^*)}{(\delta^*)^{1/2}}. \end{aligned} \right. \quad (3.15c)$$

The 3-term expression is extrapolated to the wall and compared with the curve-fitted expression in figure 3.6. The underestimation of the derivative by equation (3.15a) is obvious.

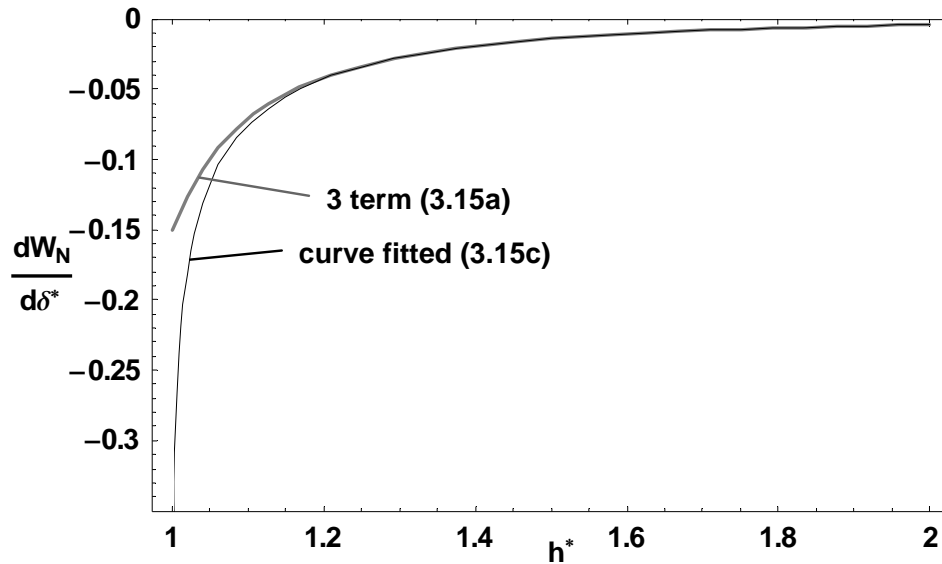


Figure 3.6. Comparison between the 3-term approximation and the hybrid-formulation.

3.4 History force

While the added mass force accounts for the form drag due to unsteady particle motion, the history force addresses the viscous effects that are not included in the steady viscous drag discussed in section 3.2. As discussed in Crowe et al. (1998), this force accounts for the temporal delay in the boundary-layer development when the relative velocity between a solid surface and its adjacent fluid varies in time.

After Stokes (1851) developed the hydrodynamic force for a solid sphere oscillating in a viscous unbounded fluid, Basset (1888) and Boussinesq (1903) generalized Stokes'

solution by considering all possible oscillating frequencies. The total hydrodynamic force for an arbitrary sphere translation in an unbounded quiescent liquid is:

$$F = -6\pi\mu a U(t) - \frac{2}{3}\pi a^3 \rho_f \frac{dU}{dt} - 6\pi\mu a^2 \frac{1}{\sqrt{\pi\nu_f}} \int_0^t \frac{dU}{d\tau} \frac{d\tau}{\sqrt{t-\tau}}, \quad (3.16)$$

where the first two terms represent the steady viscous force and the added mass force respectively. The last term is the history force, which depends on the sphere acceleration history. The force has a time kernel $t^{-1/2}$ that diminishes the effects from the earlier sphere acceleration. The derivation can be found in Landau and Lifshitz (1987), where the arbitrary sphere velocity is represented as a Fourier integral. They solved the equation of motion in the frequency space and transformed back to the time domain by an inverse Fourier integral over the whole frequency domain. The inversion is conceptually identical to both Basset's and Boussinesq's earlier derivations and gives an equivalent expression, as the last term in equation (3.16):

$$F_H = -6\pi\mu a^2 \frac{1}{\sqrt{\pi\nu_f}} \int_0^t \frac{dU}{d\tau} \frac{d\tau}{\sqrt{t-\tau}}. \quad (3.17)$$

All three derivations assume a creeping flow condition in an unbounded fluid domain. Thus equation (3.17) is subject to modifications for higher Reynolds number flow conditions and the presence of the wall.

3.4.1 Moderate Reynolds number effects

To extend the classical history force for a moderate Reynolds number flow condition, Mei and Adrian (1992) performed a detailed numerical simulation to investigate the unsteady hydrodynamic force on a sphere when the relative velocity between a solid sphere and the ambient flow oscillates at small amplitudes and low frequencies. A new kernel was found to decay faster than $t^{-1/2}$ as Stokes' solution is for oscillations at small amplitude but high frequencies.

The numerical result for finite Reynolds number was matched with the analytic solution, equation (3.17), to obtain a modified history force:

$$F_H = -6\pi\mu a \int_0^t \frac{dU}{d\tau} K(t-\tau) d\tau, \quad (3.18)$$

With a new kernel $K(t-\tau) = \left\{ \left[\frac{\pi(t-\tau)v_f}{a^2} \right]^{1/4} + \left[\frac{\pi |U(t)|^3 (t-\tau)^2}{2 av_f f_H^3(\text{Re})} \right]^{1/2} \right\}^{-2}$ using a fitted

function $f_H(\text{Re}) = 0.75 + 0.105 \text{Re}$. The new kernel collapses to the conventional history force kernel $(t-\tau)^{-1/2}$ at small times but gives a faster decay as t^{-2} for longer times. The history force for a higher Reynolds number flow thus has a shorter memory. Though numerical investigation was performed for $\text{Re} < 100$, the applicability of equation (3.18) for translational motion at higher Reynolds numbers is expected. The reason follows.

Consider boundary layer development over a plate that oscillates in its own plane. The alternating motion changes the sign of the vorticity generated at the surface. As the positive and the negative vorticity diffuse, they cancel each other, limiting the viscous

penetration, which results in a confined viscous penetration depth and thus a limited boundary layer growth (Batchelor 1967). This mechanism explains the characteristic transverse length scale that Mei and Adrian (1992) observed in their simulation of an oscillating flow over a stationary sphere. For a sphere traveling at higher Reynolds numbers, the boundary layer is more confined, which validates the use of equation (3.18) for Reynolds numbers beyond 100.

Kim, Elghobashi, and Sirignano (1998) further extended Mei and Adrian's result by considering a complete range of oscillating conditions. They examined both small and large oscillation amplitudes and developed a kernel based on Mei and Adrian's formulation but with modifications for further unsteadiness. With a new function $G(t)$ and a fitted coefficients, C_1 , the modified kernel takes the form:

$$K(t - \tau) = \left\{ \left[\frac{\pi(t - \tau)v_f}{a^2} \right]^{\frac{1}{2}C_1} + G(\tau) \left[\frac{\pi |U(t)|^3 (t - \tau)^2}{2 a v f_H'^3(\text{Re})} \right]^{\frac{1}{2}C_1} \right\}^{-C_1}. \quad (3.19)$$

The new coefficient $C_1 = 2.5$ differs from the value 2 used by Adrian and Mei. A second coefficient $C_2 = 0.126$ in the function $f_H' = 0.75 + C_2 \text{Re}$ can be compared to Adrian and Mei's fitted result of 0.105. The newly added coefficient $G(t) = 1 / \left(1 + \beta(t) \sqrt{M_1(t)} \right)$ highly depends on the instantaneous flow behavior. This time-varying coefficient depends on a primary acceleration number, $M_1(t) = \frac{2a}{|U - V|^2} \left| \frac{d(U - V)}{dt} \right|$, and another fitted function $\beta(t) = C_5 / \left\{ 1 + \phi_r(t)^{1+C_4} / [C_3(\phi_r(t) + \phi_r(t)^{C_4})] \right\}$. The fitted function, β , depends on constants $C_3 = 0.07$, $C_4 = 0.25$, $C_5 = 22.0$, and the ratio $\phi_r(t) = M_2(t) / M_1(t)$, which also

depends on a secondary acceleration number $M_2(t) = \frac{(2a)^2}{|U-V|^3} \left| \frac{d^2(U-V)}{dt^2} \right|$. In the current study, the kernel developed by Kim, Elghobashi, and Sirignano (1998) in equation (3.19) is used with a zero ambient flow velocity V .

3.4.2 Wall effects on the history force

As shown in the previous section, the history force is known as an unsteady viscous force that depends on the sphere acceleration history, which is related to the temporal delay of the boundary layer development due to unsteady surface motion. The physical meaning of this force can be interpreted as follows. When a stationary infinite flat plate is impulsively accelerated to a constant speed, U_0 , the viscous flow in the upper half plane ($y \geq 0$) can be readily found, as this corresponds to Stokes' first problem:

$$\frac{u(y,t)}{U_0} = 1 - \operatorname{erf}\left(\frac{y}{\sqrt{4\nu_f t}}\right). \quad (3.20)$$

The wall shear stress can be calculated from equation (3.20) to be $\tau = \mu U_0 / \sqrt{\pi \nu_f t}$. Describe a general unsteady plate motion as a series of infinitesimal step changes, as sketched in figure 3.7, the cumulative wall shear stress at a later time, t , is found as:

$$\tau(t) = \frac{\mu}{\sqrt{\pi \nu_f}} \left[\frac{\Delta U_0}{\sqrt{t}} + \frac{\Delta U_1}{\sqrt{t-t_1}} + \frac{\Delta U_2}{\sqrt{t-t_2}} + \dots \right], \quad (3.21)$$

using the linearity of low Reynolds flow.

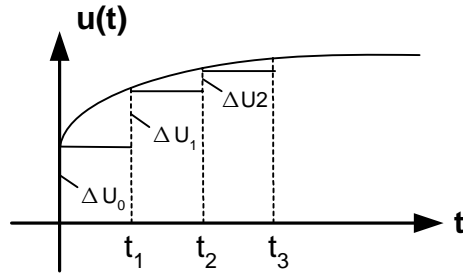


Figure 3.7. Infinitesimal stepwise acceleration of the plate.

The history force *per unit plate area* is obtained from equation (3.21) by replacing the discrete sum with a continuous time integral, $F_H = \frac{\mu}{\sqrt{\pi\nu_f}} \int_0^t \frac{dU}{d\tau} \frac{d\tau}{\sqrt{t-\tau}}$, so that the classical expression in equation (3.17) is developed.

For a sphere that is translating at U_0 , an axisymmetric boundary layer is generated from the front stagnation point. For an axisymmetric flow, Mangler's transformation can be applied to simplify the equation of motion. With the coordinates defined in figure 3.8, the transformation:

$$\tilde{x} = \int_0^x \left(\frac{r_0(z)}{a} \right)^2 dz, \quad \tilde{y} = \frac{r_0(x)}{a} y, \quad \tilde{u} = u, \quad \text{and} \quad \tilde{v} = \frac{a}{r_0} \left[v + \frac{y}{r_0} u \frac{dr_0}{dx} \right],$$

reduces the three-dimensional momentum equation into a two-dimensional boundary layer equation. The function $r_0(x, y)$ represents the distance from the line of symmetry and $r_0(x) = a \sin(x/a)$ is readily found for a sphere (Panton 1995).

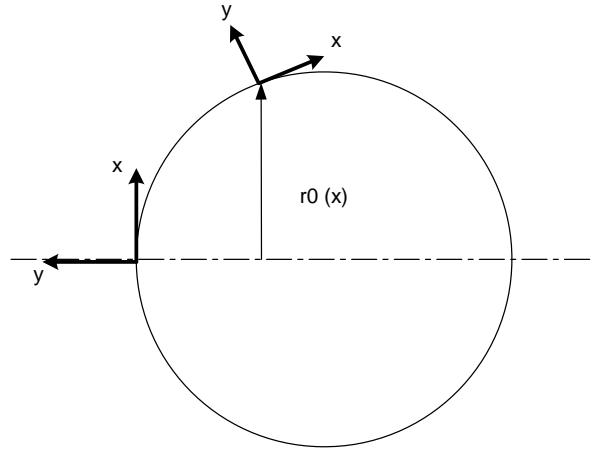


Figure 3.8. Coordinates for the Mangler's transformation.

The velocity field in the transformed boundary layer equation may be expressed as a series sum:

$$\frac{\tilde{u}(\tilde{x})}{U_0} = \sum_i c_i \left(\frac{\tilde{x}}{a} \right)^i,$$

where the coefficients depend on the shape of the object and the potential flow field outside the boundary layer (Schlichting 1960). The shear stress along the sphere surface, in terms of Mangler's variable, can be found as:

$$\tau \left(\frac{\tilde{x}}{a} \right) = \sqrt{\frac{3\rho_f \mu}{a}} U_0^{3/2} \left\{ 1.39155 \left(\frac{\tilde{x}}{a} \right) - 0.54615 \left(\frac{\tilde{x}}{a} \right)^3 + 0.0379 \left(\frac{\tilde{x}}{a} \right)^5 + \dots \right\}, \quad (3.22)$$

which reveals a 3/2 order dependence on the tangential flow velocity at the sphere surface.

As discussed in section 3.3.1, with a solid wall present in front of the moving sphere, the potential flow requires modifications and a wall-modified tangential velocity at the

sphere surface is expected. The potential function for the flow between the wall and the approaching sphere can be constructed by considering the symmetry case where two identical spheres move towards each other along their line of centers. As shown in figure 3.9, a solid sphere S_1 approaches the wall from a distance h at velocity U_0 . The requirement of no penetrating flow at the wall is first met by placing an image sphere S_2 from a distance h across the wall that moves towards S_1 at the same magnitude of speed.

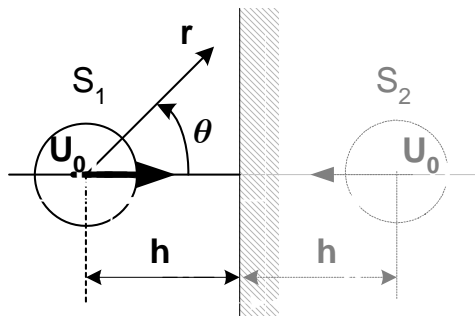


Figure 3.9. Schematic sketch of the potential flow problem when a solid sphere moves towards a solid wall.

However, the addition of this image sphere introduces a new normal flow on the surface of sphere S_1 . Thus a second image sphere (dipole) of certain strength is added to counterbalance such an induced surface flow at a certain distance from the center of S_1 . The boundary condition of the image sphere S_2 is now subjected to further modification with an additional image dipole. This process continues and the resulting potential function ϕ is found to be:

$$\begin{aligned}
\phi = \frac{U_0 a^3}{2} & \left\{ \left[\left(1 + \frac{\mu_2}{\mu_0} + \frac{\mu_4}{\mu_0} + \dots \right) - \left(\frac{\mu_1}{\mu_0} + \frac{\mu_3}{\mu_0} + \frac{\mu_5}{\mu_0} + \dots \right) \right] \frac{\cos \theta}{r^2} \right. \\
& + 2 \left[- \left(\frac{\mu_1}{\mu_0} \frac{1}{f_1^3} + \frac{\mu_3}{\mu_0} \frac{1}{f_3^3} + \frac{\mu_5}{\mu_0} \frac{1}{f_5^3} + \dots \right) \right. \\
& \left. \left. + \left(\left(\frac{1}{2h^*} \right)^3 + \frac{\mu_2}{\mu_0} \left(\frac{1}{2h^* - f_2} \right)^3 + \frac{\mu_4}{\mu_0} \left(\frac{1}{2h^* - f_4} \right)^3 + \dots \right) \right] r \cos \theta \right\}, \tag{3.23}
\end{aligned}$$

where μ_i and f_i are functions of the scaled distance $h^* = \delta^* + 1$. The first square bracket preceding $\frac{\cos \theta}{r^2}$ includes the series of image dipoles that are related to the approaching

sphere S_1 ; the first subgroup, $\left(1 + \frac{\mu_2}{\mu_0} + \frac{\mu_4}{\mu_0} + \dots \right)$, represents the sequential images inside

the sphere that are used to match the no penetrating flow boundary condition at

the S_1 surface, while the second subgroup, $-\left(\frac{\mu_1}{\mu_0} + \frac{\mu_3}{\mu_0} + \frac{\mu_5}{\mu_0} + \dots \right)$, corresponds to the

images for the wall boundary condition. The second square bracket followed by $r \cos \theta$ is the approximate contribution from the image sphere S_2 . The corresponding subgroups are for the boundary conditions at the S_2 surface and the wall respectively. It is noted that equation (3.23) should be used as an approximation of the potential flow only in the proximity of sphere S_1 .

To illustrate how the wall affects the potential function, equation (3.23) is compared with the potential function for a single solid sphere translating at the same velocity U_0 in an unbounded fluid domain,

$$\phi_0 = \frac{a^3}{2} U_0 \frac{\cos \theta}{r^2},$$

in figure 3.10 at a radial position of $r/a = 1.1$. The front stagnation point is located at $\theta = 0$. The partial sum of equation (3.23) is used as an approximation correct to h^{*-12} . When the sphere is far from the wall, the no-wall potential value is recovered.

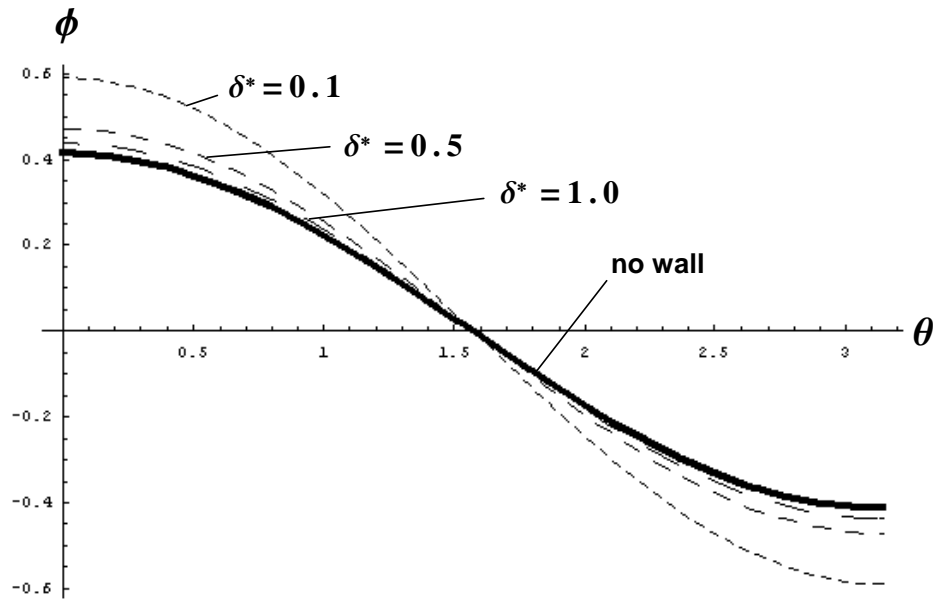


Figure 3.10. Potential functions with and without wall at different gaps ($r/a = 1.1$).

With the wall modified potential function, the radial and tangential velocities are calculated using $u_r = \frac{\partial \phi}{\partial r}$ and $u_\theta = \frac{1}{r} \frac{\partial \phi}{\partial \theta}$. As shown in figure 3.11(a), the surface tangential velocity is augmented by the presence of the wall. A smaller gap width induces a greater tangential velocity along the sphere surface due to the sequential opposing image dipoles. However, no such augmentation is observed in the radial velocity, as shown in figure 3.11(b). The wall modified radial flow velocity equals the no-wall value, validating the no penetrating flow boundary condition required at the sphere surface.

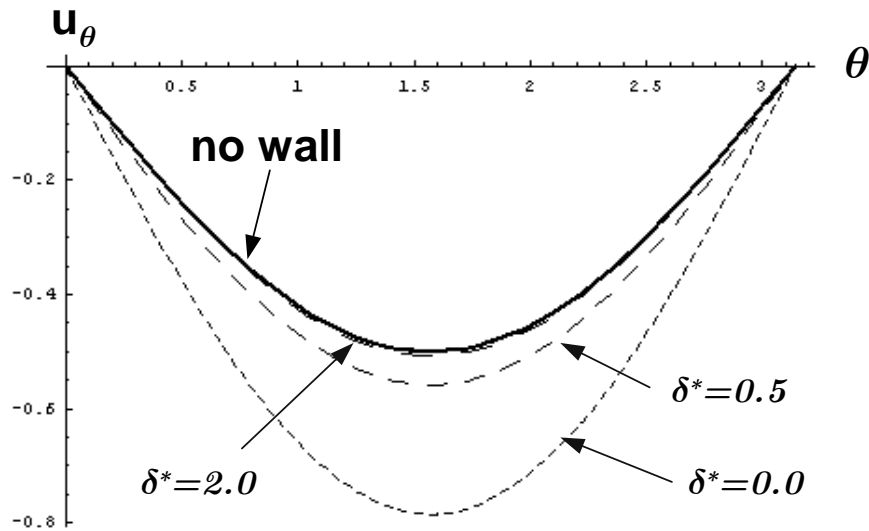


Figure 3.11(a). Tangential flow velocity at the sphere surface at different gaps.

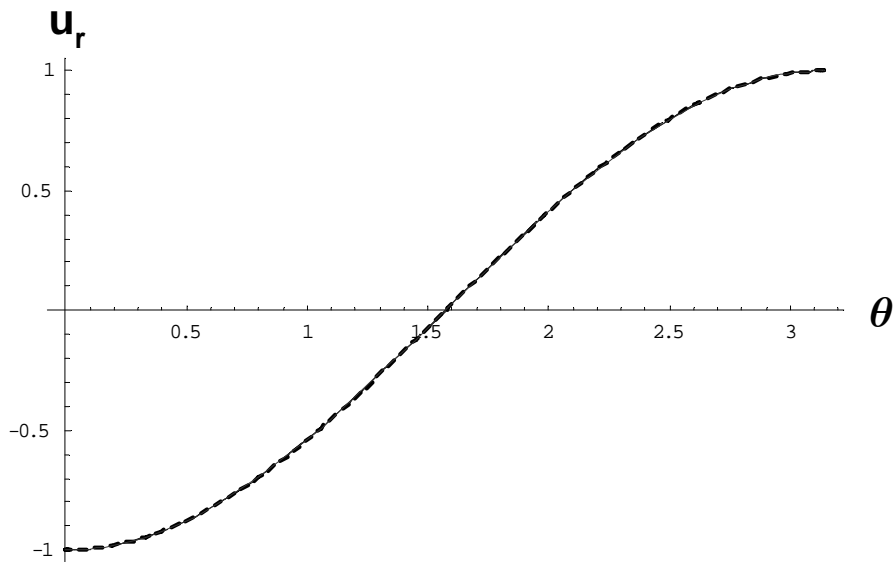


Figure 3.11(b). Radial flow velocity at the sphere surface at different gaps.

It is proposed that the wall affects the history force by amplifying the tangential flow velocity. An *augmentation factor* $K_H(\delta^*)$ can be found by dividing the wall-modified tangential velocity by the no-wall value, $-\frac{U_0}{2}\sin\theta$, at the sphere surface:

$$\begin{aligned}
K_H(\delta^*) &= 1 + \frac{0.375 - 0.03125/(1-2h^{*2})^3}{h^{*3}} - \frac{3}{(1-4h^{*2})^3} - \frac{0.015625}{(h^* - 2h^{*3})^3} \\
&+ \frac{3}{(1-12h^{*2} + 16h^{*4})^3} + \frac{0.375}{(3h^* - 16h^{*3} + 16h^{*5})^3}.
\end{aligned} \tag{3.24}$$

Equation (3.24) is plotted in figure 3.12 as a monotonically increasing function of decreasing normalized gap width.

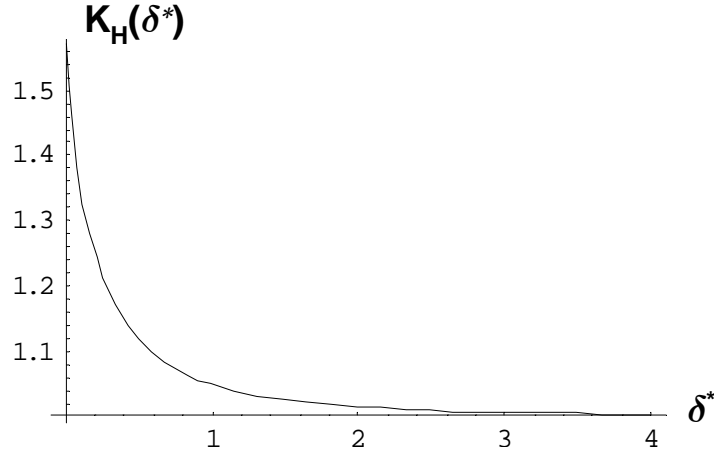


Figure 3.12. Augmentation factor for the wall-modified history force as a function of the scaled gap width.

With the wall-modified surface tangential velocity, $K_H(\delta^*)U_0$, the shear stress in equation (3.22) is modified accordingly:

$$\tau\left(\delta^*, \frac{\tilde{x}}{a}\right) = \sqrt{\frac{3\rho_f\mu}{a}} [K_H(\delta^*)U_0]^{3/2} \left\{ 1.39155\left(\frac{\tilde{x}}{a}\right) - 0.54615\left(\frac{\tilde{x}}{a}\right)^3 + 0.0379\left(\frac{\tilde{x}}{a}\right)^5 + \dots \right\}. \tag{3.25}$$

When equation (3.25) is compared to the no-wall shear stress, equation (3.22), the terms inside the curly brackets represent the same shear stress distribution over the sphere as the no-wall value. The only difference is the augmentation factor $K_H(\delta^*)$ that is raised to the power of $3/2$, in accordance with the shear stress dependence on the surface tangential velocity. Therefore, integrated with equation (3.19), the wall-modified history force is proposed as

$$F_H(\delta^*, t) = -6\pi\mu a K_H(\delta^*)^{3/2} \int_0^t \frac{dU}{d\tau} K(t-\tau) d\tau. \quad (3.26)$$

The factor $K_H(\delta^*)$ accounts for the wall effects on amplifying the shear stress at the sphere surface. The effects of motion at higher Reynolds number are imbedded in the new history kernel $K(t-\tau)$ given by equation (3.19). Note that the incoming sphere also generates a boundary layer along the solid wall when the fluid is squeezed out of the gap. This second boundary layer might change the shear stress distribution over the approaching sphere surface, the terms in the curly bracket of equation (3.25), but it is assumed to be negligible in the current work.

3.5 Summary

In this chapter, three conventional hydrodynamic forces are modified for the presence of the wall and are found to diverge when the interstitial gap drops to zero. Moreover, the effects of a higher Reynolds number flow are addressed by using an empirical relation or a fitted expression from simulation results.

Chapter 4

Immersed Pendulum Motion Towards a Solid Wall

In chapter 3, the conventional hydrodynamic forces on a solid sphere were investigated for a collision process beyond Stokes flow regime. A flow model, including the steady viscous force, the added mass force and the Basset history force, was proposed with modifications for the effects at higher Reynolds flow conditions and for the presence of wall. In order to validate the proposed model, a pendulum motion towards a solid wall is simulated and will be compared with the available experimental measurements in this chapter. In addition, the impact of two solid surfaces with interstitial liquid layer is also investigated. A rebound scheme that considers different contact mechanisms is proposed and implemented in the current computation. The predicted rebound motion is examined with the trajectory of an actual pendulum rebound. The proposed collision model, comprising the flow model from chapter 3 and the new rebound scheme, is applied to estimate the effective coefficient of restitution as a function of particle Stokes numbers. By comparing the model prediction to the experimental results, the performance of the proposed collision model is evaluated.

4.1 The equation of motion

The equation of motion for an immersed pendulum was derived in chapter 3, taking into account the wall modifications on all non-conservative hydrodynamic forces. The schematic representation of the problem of an immersed pendulum motion towards a wall is shown in figure 4.1 with the relevant variables. The circumferential position of the sphere center s is scaled by the total arc length $s = L\theta_0$ calculated with pendulum string length L and release angle θ_0 . The time and the circumferential velocity are scaled with two *characteristic convective scales*, as $t^* = t/T_C$ and $u^* = u/U_C$, subject to the requirement of $T_C U_C = L\theta_0$.

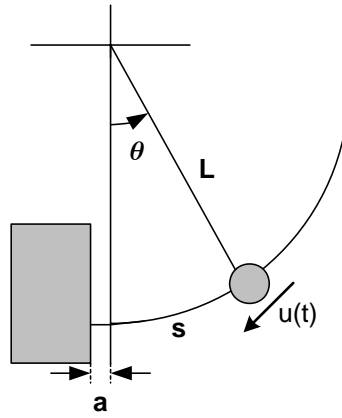


Figure 4.1. Schematic representation of a pendulum motion towards a fixed wall in liquid.

To estimate the characteristic velocity U_c , it was assumed that the effective potential energy is fully dissipated by the steady viscous force when the sphere travels the whole arc at velocity U_c . The following equation balances the potential energy by the dissipative viscous work:

$$\frac{4}{3} \pi a^3 (\rho_p - \rho_f) g \Delta H = 6 \pi \mu a U_c \phi(\text{Re}_c) s, \quad (4.1)$$

for a sphere of radius a and density ρ_p that moves in a liquid of viscosity μ_f and density ρ_f . The experimental relation for modifying the steady viscous force for higher Reynolds number $\phi(\text{Re})$ is given in equation (3.2) and $\Delta H = L(1 - \cos \theta_0)$. Equation (4.1) can be manipulated into:

$$\text{Re}_C \phi(\text{Re}_C) = \frac{4}{9} \frac{(1 - \cos \theta_0)}{\theta_0} Ar, \quad (4.2)$$

where $\text{Re}_C = 2a|U_C|/\nu_f$ is the characteristic Reynolds number and $Ar = ga^3(\frac{\rho_s}{\rho_f} - 1)/\nu_f^2$ is the Archimedes number that characterizes the ratio of the effective gravity to the viscous drag for an immersed object motion. Iteratively solving equation (4.2) determines the characteristic convective velocity U_C and the resulting convective time T_C . Besides T_C at characterizes the time required for an immersed pendulum motion towards the wall, there are other time scales important to the problem, including the diffusion time scale, a^2/ν_f , and the period for a pendulum motion, $\sqrt{L/g}$, with negligible liquid effects. However, only the characteristic convective time T_C results in non-dimensional equations of motion of comparable order of magnitude over all the impact conditions investigated in this chapter.

The relationship between the Archimedes number and the convective Reynolds number from equation (4.2) is illustrated in figure 4.2 for a pendulum motion at a release angle of 15° . The Archimedes number increases monotonically with increasing Re_C . Due to the square of liquid viscosity in the denominator, the Archimedes number is in general of 2–4 orders of magnitude greater than the characteristic Reynolds number.

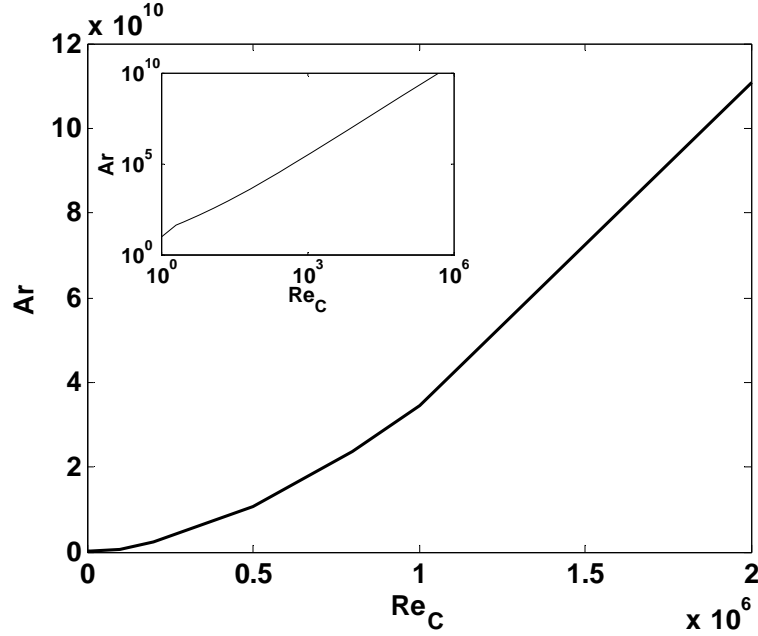


Figure 4.2. Archimedes number as a function of the characteristic Reynolds number for an immersed pendulum motion from $\theta_0 = 15^\circ$.

With the effective mass, $M^*(\delta^*) = \frac{\rho_s}{\rho_f} + \frac{1}{2}(1 + 3W(\delta^*))$, a set of dimensionless equations

was found for the pendulum motion as follows:

$$\begin{cases} \frac{ds^*}{dt^*} = U^* \\ M^*(\delta^*) \frac{dU^*}{dt^*} = \frac{Ar}{Re_c^2} \sin \theta - \frac{3}{4} \frac{dW}{d\delta^*} U^{*2} - \frac{9}{4} \frac{U^*}{Re_c} \phi(Re) - \frac{9}{4} \frac{K_H^{\frac{3}{2}}(\delta^*)}{Re_c} \int_0^{t^*} \left(\frac{dU^*}{d\tau^*} \right) K(t^* - \tau^*) d\tau^* . \end{cases} \quad (4.3)$$

The first equation calculates the pendulum circumferential velocity and the second equation is the momentum balance equation for the sphere. The dimensionless forces on the right-hand side of the momentum equation are the effective gravity, the opposing pressure force, the steady viscous drag, and the history force respectively.

The correction for higher Reynolds number effects on the steady viscous drag, $\phi(\text{Re})$, is replaced by Brenner's wall correction term, $\lambda_{\pm}(\delta^*, \text{Re})$, when the sphere moves close to the wall. Since the viscous diffusion is a continuous process, a smooth transition was guaranteed by matching the local values of $\phi(\text{Re})$ and $\lambda_{\pm}(\delta^*, \text{Re})$. At large convective Reynolds number, the viscous drag and the history force become negligible and the effective gravity and the pressure force govern the pendulum motion. The dimensionless factor Ar/Re_c^2 in the effective gravity term is plotted as a function of Re_c in figure 4.3. The quantity of this value remains of order unity even at large Reynolds numbers, indicating the case where the effective gravity drives the pendulum motion without significant viscous dissipation. Moreover, the opposing pressure force, which is a result of potential flow theory, is independent of viscosity.

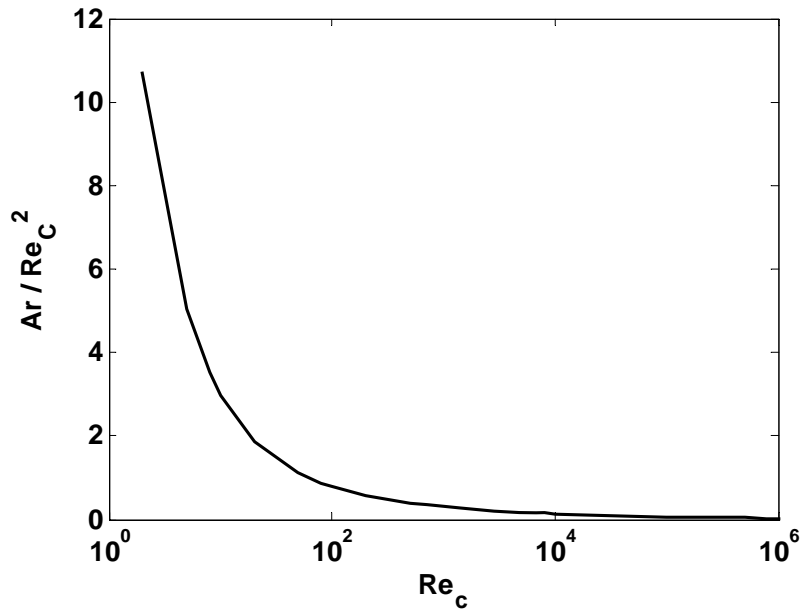


Figure 4.3. The preceding dimensionless factor of the effective gravity in the momentum equation of equation (4.3). The release angle is $\theta_0 = 15^\circ$.

The history kernel, in terms of the dimensionless variables, is:

$$K(t^* - \tau^*) = \left\{ \left(\frac{2\pi}{\text{Re}_c} (t^* - \tau^*) \right)^{\frac{1}{2}c_1} + G(\tau^*) \left(\frac{\pi}{4} \text{Re}_c \frac{|U^*|^3 (t^* - \tau^*)^2}{f_H(\text{Re})^3} \right)^{\frac{1}{2}c_1} \right\}^{-c_1},$$

$$\text{where } G(t^*) = \frac{1}{1 + \beta(t^*)\sqrt{M_1(t^*)}}, \quad \beta(t^*) = \frac{C_5}{1 + \phi_r^{1+C_4} / [C_3(\phi_r + \phi_r^{C_4})]}, \quad \phi_r(t^*) = \frac{M_1(t^*)}{M_2(t^*)},$$

$$M_1(t^*) = \frac{2}{|U^*|} \left| \frac{d|U^*|}{dt^*} \right|, \quad \text{and } M_2(t^*) = \frac{4}{|U^*|^3} \left| \frac{d^2|U^*|}{dt^{*2}} \right|.$$

The pendulum starts from zero velocity with the effective gravity as the only driving force. Thus the initial conditions:

$$U^* \Big|_{t^*=0} = 0 \quad \text{and} \quad \frac{dU^*}{dt^*} \Big|_{t^*=0} = \frac{Ar}{\text{Re}_c^2} \sin \theta_0$$

are used when the set of equations (4.3) is solved numerically.

4.2 Rebound in a liquid

Theoretically, the singularity $\delta^* = 0$ requires that all of the hydrodynamic forces increase to infinity at the wall, resulting in a fully stopped sphere prior to contact. Since the surface is neither perfectly smooth nor rigid, as assumed in the theory, rebound is observed in real immersed collisions. Therefore, a criterion of where and how the sphere should rebound is crucial to any collision model. The first work that solves the minimum

lubrication film thickness for two approaching surfaces is by Davis et al. (1986). They applied the elastohydrodynamic lubrication theory (EHL) which couples the interstitial fluid pressure with the solid surface deformation and numerically investigated the collision between two deformable elastic spheres. The findings are crucial to the rebound mechanism proposed in the current work. Thus their analysis is summarized in the following section.

4.2.1 EHL collision of two solid spheres

(a) Outline of the paper by Davis et al. 1986

As depicted in figure 4.4, a perfectly smooth but deformable solid sphere, of mass m_p and radius a , approaches the stationary wall in a liquid of viscosity μ from a distance δ with local velocity U . The sphere motion is described by two kinetic equations: $d\delta/dt = -U(t)$ and $m_p dU/dt = -6\pi\mu a^2 U/\delta$, assuming that the lubrication force dominates the hydrodynamic forces.

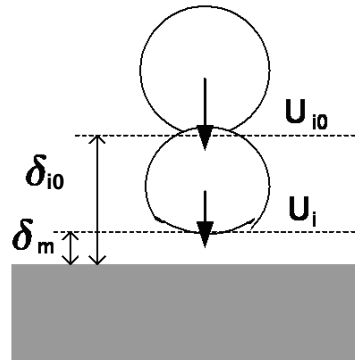


Figure 4.4. Schematic of elastohydrodynamic collision of a sphere on a stationary wall in a viscous liquid.

These two equations can be combined, yielding the sphere deceleration as a function of the separation as:

$$m_p \frac{dU}{d\delta} = \frac{6\pi\mu a^2}{\delta}. \quad (4.4)$$

With the initial velocity $U = U_{i0}$ at $\delta = \delta_{i0}$, equation (4.4) can be integrated to determine the local approach velocity U at location δ :

$$\frac{U}{U_{i0}} = 1 - \ln\left(\frac{\delta_{i0}}{\delta}\right) / St_{i0}, \quad (4.5)$$

which depends on the impact particle Stokes number, $St_{i0} = m_p U_{i0} / 6\pi\mu a^2$. The gap δ depends on the instantaneous surface deformation as estimated by Hertz contact theory. The stress distribution on the solid surface is required to match the pressure in the liquid phase, which couples Hertz contact theory with the lubrication theory at the interface. The initial separation where the fluid force starts to deform the surface, δ_{i0} , is assumed to be comparable to the lubrication film thickness. Davis et al. (1986) found a dimensionless elasticity parameter that quantifies the tendency of elastic deformation under the lubrication pressure force as:

$$\varepsilon = \frac{4E^* \mu U_{i0} a^{3/2}}{\delta_{i0}^{5/2}}. \quad (4.6)$$

Besides the impact velocity and the initial film thickness, equation (4.6) also depends on the sphere size, the liquid viscosity, and the reduced elastic modulus $E^* = (1 - \nu_1^2) / \pi E_1 + (1 - \nu_2^2) / \pi E_2$ that depends on the Poisson's ratio ν_i and the Young's modulus E_i of each sphere ($i = 1, 2$). In addition to the elasticity parameter, the minimum

approach distance δ_m for a collision involving significant surface deformation was also obtained:

$$\delta_m \approx \frac{1}{3} \delta_{i0} \varepsilon^{\frac{2}{3}}. \quad (4.7)$$

The factor $1/3$ in equation (4.7) was extrapolated from their simulation result, as reproduced in figure 4.5. Once the impact Stokes number exceeds a certain threshold, the minimum approach distances asymptote to a constant value over a wide range of ε . The asymptotic value decreases slightly with increasing Stokes numbers but a non-zero constant is expected for Stokes numbers greater than 20. Throughout this chapter, equation (4.7) will be applied to estimate the minimum approaching distance.

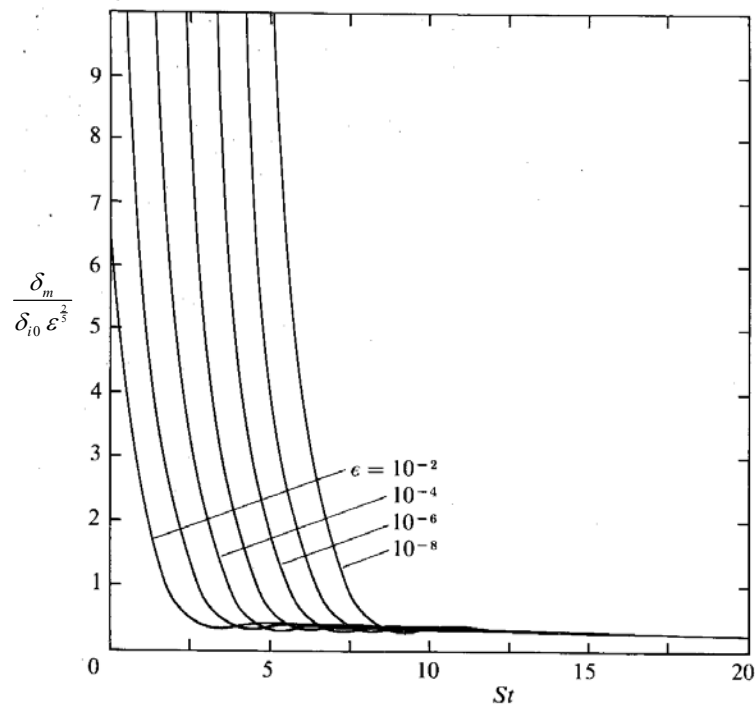


Figure 4.5. Minimum distance of approach for a deformed sphere as a function of the elasticity parameter and the particle Stokes number. (Figure 13 of Davis et al. 1986)

(b) Comments

In order to apply the EHL results, equations (4.5), (4.6), and (4.7), it is crucial to have a good estimate of the initial film thickness δ_{i0} . In the Tribology literature, the shearing film thickness for a steady roller pair can be found as a function of the rolling velocity, the normal load, the liquid viscosity, and the size and the elastic properties of the rollers (Gohar 1988). However, the film thickness for an unsteady squeezing sphere pair has not been studied. The lack of successful experimental investigations is mainly due to the difficulty in measuring such a rapid, unsteady process.

In Davis et al. (1986), the only condition imposed on δ_{i0} is to be small with respect to the sphere radius a . They use $\delta_{i0} \approx 0.01a$ for the aerosol and hydrosol particles. The size of these fine particles guarantees small particle Reynolds number and the lubrication force reasonably approximates the actual total hydrodynamic force. As mentioned in chapter 3, the wall-modified Stokes' drag behaves as the lubrication force when both the normalized gap, $\delta^* = \delta/a$, and the local Reynolds number approach zero. It is thus of special interest to compare the lubrication force, $F_{\text{lub}} = 6\pi\mu aU/\delta^*$, with the wall-modified Stokes' drag, $F = 6\pi\mu aU\lambda_+(\delta^*, \text{Re})$. Brenner's correction, $\lambda_+(\delta^*, \text{Re})$, is given in equation (3.4). In figure 4.6, the normalized distance, $\delta^* = 0.99/\lambda_+(\delta^*, \text{Re})$, where the wall-modified Stokes drag reaches 99% of the lubrication force is plotted as a function of impact Reynolds number Re_i . For motion with $\text{Re}_i \leq 0.1$, the dimensionless gap δ^* asymptotes to 0.011, corresponding to the value suggested by Davis et al. (1986) for fine particles.

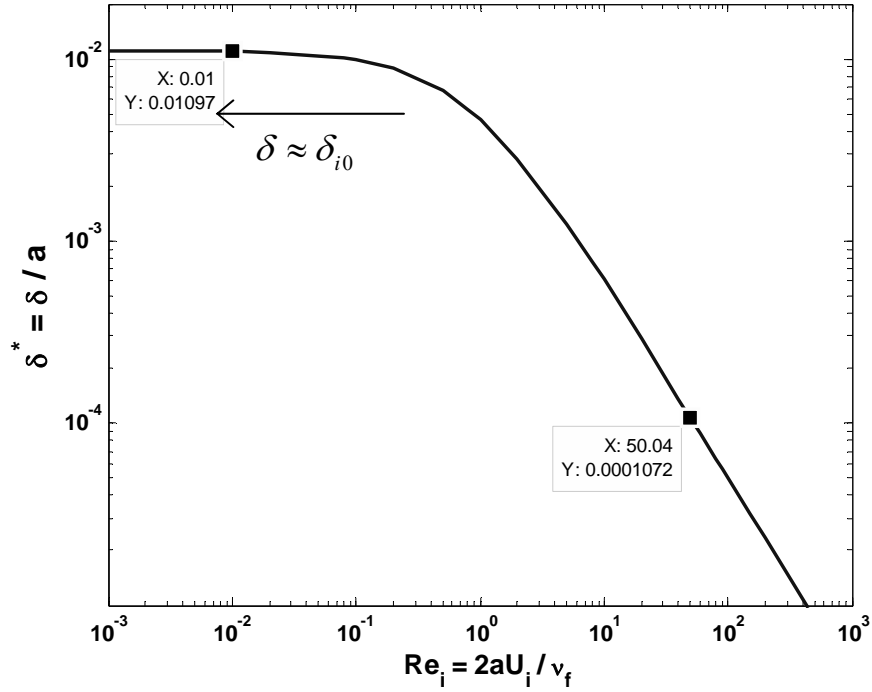


Figure 4.6. The normalized gap at which the wall-modified Stokes' drag reaches 99% of the classical lubrication force at the same impact Reynolds number.

However, large solid particles that possess sufficient inertia to overcome the hindering hydrodynamic forces can collide at a Reynolds number greatly higher than 0.1, which invalidates the quasi-steady flow condition. The dynamic pressure field in the wall-modified added mass force—the second term of equation (3.6)—may result in additional surface deformation. Therefore, a direct reading from figure 4.6 will underestimate the undeformed separation δ_{i0} and result in erroneous calculation with EHL theory. For a collision at $Re_i \approx 50$ and $St_i \approx 14$, the normalized lubrication film thickness is estimated to be $\delta_{i0}^* \approx 10^{-4}$ from figure 4.6. If the added mass force, after scaling by $m_p U_C/T_C$, is compared with the lubrication force in figure 4.7(a), the wall-modified added mass force exceeds the lubrication force at a distance of about $0.02a$. As indicated in figure 4.7(b), the wall-modified added mass force surpasses F_{lub} , by two orders of magnitude, when the gap drops to the estimated film thickness. Thus, under the investigated impact

conditions of $Re_i \approx 50$ and $St_i \approx 14$, the total liquid force should start deforming the solid surface at a distance greater than $0.02a$. If the wall-modified added mass force was to be included in an extended EHL theory, the initial film thickness δ_{i0} should be thicker than the estimation considering only the lubrication force.

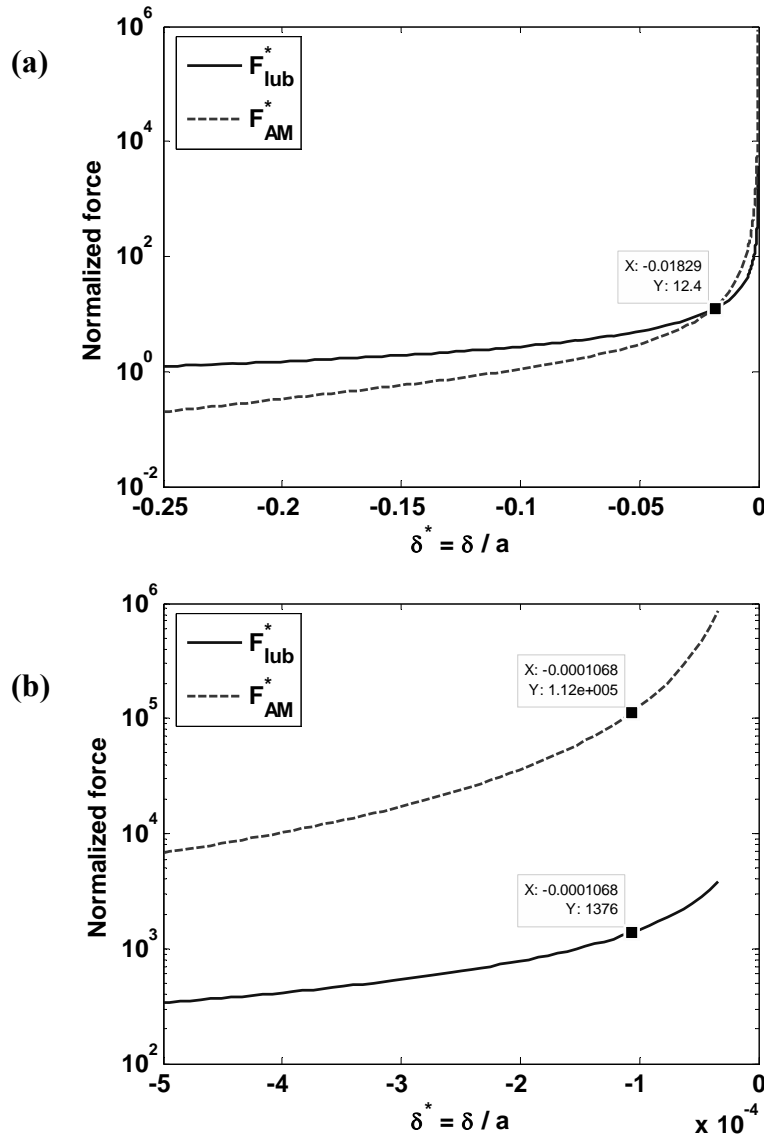


Figure 4.7. Comparison of the added mass and the lubrication force as a function of normalized gap for an immersed collision at $Re_i \approx 50$ and $St_i \approx 14$: (a) upon approaching and (b) at the estimated film thickness.

Furthermore, in addition to the steady viscous drag and the added mass force, the history force may become important for the approach motion towards the wall. Hence, the EHL model in general will underestimate the actual hydrodynamic forces. The uncertainty in estimating the initial separation δ_{i0} also poses a limitation on extending the EHL theory, referring equation (4.5), to an impact at higher Reynolds and Stokes numbers. Thus, it is important to consider the full hydrodynamic model-the momentum equation in equation (4.3)-for an accurate pendulum motion towards a stationary solid wall.

The inclusion of the added mass force brings to the problem a new time scale that depends on the sphere acceleration. If the added mass force affects the particle motion at a rate slower than the force due to solid deformation, the conventional EHL theory should serve as a good model for the approach motion. The competition between this hydrodynamic deceleration time, $U_i/(dU_i/dt)$, and the deforming strain rate should provide a measure of how crucial the added mass force is in any collision model.

4.2.2 Contact mechanism in liquid

For a fully immersed collision, the minimum approach distance from EHL theory provides a length scale to determine the rebound distance. A second length scale, provided by the actual asperity height, should also be considered. With these two length scales, the contact mechanism for an immersed collision may be separated into the following three cases.

Case I: Asperity contact

Consider a solid particle that is rigid but not perfectly smooth. Upon collision, the physical asperity contact occurs at a distance commensurate to the surface roughness σ_s , resulting in a surface deformation as illustrated in figure 4.8. Like a dry collision, the restitution impulse rebounds the particle so long as the deformation is not fully plastic. The hydrodynamic effects are assumed to be negligible during the contact and the immediate rebound velocity can be characterized using the dry coefficient of restitution as $U_r = -e_{dry} U_i$.

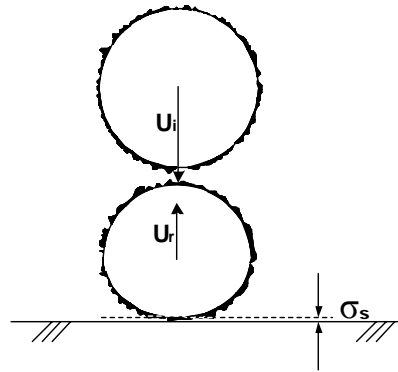


Figure 4.8. Sphere collides and rebounds via an asperity contact.

Case II: Wet contact (EHL contact)

When the liquid is being squeezed during a collision, the hydrodynamic pressure built up in the gap can deform the solid surfaces as delineated in the EHL theory. The minimum approach distance δ_m can be found using equation (4.7). Once the two deformed surfaces come to the minimum approach distance, the stored strain energy is released and the restitution process commences. Since Hertz contact theory assumes fully elastic deformation, no energy is lost in the solid phase. Therefore, for an EHL contact, the instant rebound velocity should take the negative value of the instant impact velocity, i.e., $U_r = -U_i$.

Case III: Mixed contact

Under some impact conditions, the two length scales are comparable to each other. The developing lubrication force flattens the asperities and delays the physical contact to a distance smaller than the dry surface roughness σ_s . Mixed contact mechanism is proposed in this section to estimate the instant rebound velocity at the new asperity height.

As shown in figure 4.9, the asperity is modeled as a semi-sphere with a radius commensurate to its undeformed height σ_s . The deformation is treated as a spherical indenter under axisymmetric loading (Johnson, 1985). Due to the smallness of the asperity, the deformation is assumed to be fully plastic and is estimated as:

$$\Delta\sigma_s = r^2/2\sigma_s, \quad (4.8)$$

where $r \approx 40\pi E^* Y \sigma_s$ is the characteristic radius of the contact area and Y is the yield strength of the deforming material. Equation (4.8) may be rewritten as:

$$\Delta\sigma_s = \frac{(40\pi E^* Y)^2}{2} \sigma_s = k \sigma_s.$$

Using this expression, the impact sphere is proposed to rebound at the deformed asperity height $(1-k)\sigma_s$. The typical value of k for a collision between a steel ball bearing and a Zerodur wall is about 1/8. This material pair has $E^* \approx 6 \times 10^{-12} Pa^{-1}$ and $Y = 6 \times 10^8 Pa$. On a Delrin-on-Zerodur collision, the typical value of k becomes about 1/12 with a corresponding material constant $E^* \approx 1 \times 10^{-10} Pa^{-1}$ and $Y \approx 0.4 \times 10^8 Pa$. The physical asperity contact results in an energy loss in the solid phase that can be characterized by e_{dry} , as an asperity contact.

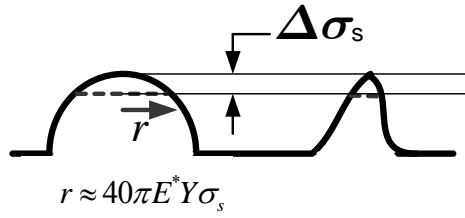


Figure 4.9. Asperity deforms as a hemispherical indenter under lubrication force.

Furthermore, the liquid trapped between the asperities will further reduce the kinetic energy. A measure of such hydrodynamic effects may be obtained by considering the particle momentum change due to inter-asperity fluid forces. As shown in figure 4.10, consider the interaction between the impact sphere and two asperities in the contact area. Since the asperity is of micron scale, it is assumed that the local trapped fluid motion can be described as a squeezing lubrication force:

$$f = 6\pi\mu a^2 U_i / \sigma_s ,$$

depending on the asperity height. The number of such inter-asperity liquid wells, N , depends on both the contact area and the number density of the asperities over the sphere surface. The lubrication liquid wells across the contact area decelerate the impact sphere motion as N parallel springs. Thus the total liquid force may be estimated as the sum over all such localized squeezing lubrication forces:

$$F = N6\pi\mu a^2 U_i / \sigma_s .$$

Consider a forcing duration $\Delta T \approx \sigma_s / U_i$, a quantity that characterizes the ratio of the sphere inertia, $m_p U_i$, to the total inter-asperity dissipating force may be estimated as:

$$st = \frac{m_p U_i}{N6\pi\mu a^2}, \quad (4.9)$$

similar to the particle Stokes number. Equation (4.9) can be readily rewritten in terms of the impact particle Stokes number as $st = St_i/N$.

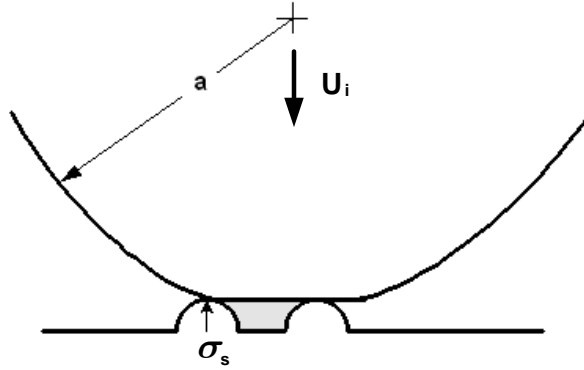


Figure 4.10. Interaction between the impact sphere and the fluid trapped between the surface asperities, which dissipates more kinetic energy and reduce the restitution during a mixed contact.

In chapter 2, the kinetic energy loss into the liquid phase is estimated by relating the resultant sphere momentum change to the inverse of the local particle Stokes number. Similarly, the additional energy loss into the trapped liquid wells across the contact area is first correlated to the momentum change of the sphere, $m_p \Delta U_i$, which then reveals the inverse dependence on the particle Stokes number. Therefore, a dissipation parameter, η , is proposed as:

$$\eta = -\frac{m_p \Delta U_c - m_p \Delta U_i}{m_p \Delta U_c}, \quad (4.10)$$

where the actual momentum change was scaled by the critical momentum loss, $m_p \Delta U_c$, that leads to zero restitution. With the inverse relationships, $m_p \Delta U_c \sim 1/st_c = N/St_c$ and $m_p \Delta U_i \sim N/St_i$, the dissipation parameter may be manipulated into:

$$\eta = 1 - \frac{St_c}{St_i}. \quad (4.11)$$

At high particle Stokes numbers, the inter-asperity fluid effects are negligible due to the large particle inertia and equation (4.11) results in a nearly unity η . Zero η indicates the case that a sphere collides at a non-zero velocity, loses all its kinetic energy to the inter-asperity liquid, and does not rebound. To characterize the total energy loss in both phases during a mixed contact, the dry coefficient of restitution is multiplied by the dissipation parameter, and the instant rebound velocity is obtained as $U_r = -e_{dry} \eta U_i$. To incorporate collisions at $St_i < St_c$, the dissipation parameter is set to zero since a fully stopped sphere should be expected for an impact with such low particle inertia.

4.2.3 Determination of the critical Stokes number

The experiments involving particle-wall collisions with liquid effects revealed the existence of a critical Stokes number St_c below which rebound from the wall does not occur. As stated in chapter 2, such phenomenon can be attributed to either a fully stopped sphere upon contact or a sphere with insufficient rebound inertia to depart from the wall. In EHL theory, the sphere deforms and comes to rest at the minimum approach distance, δ_m , at the end of the compression phase. Using $U_i = 0$ at δ_m , the minimum critical Stokes number required for rebound can be estimated from equations (4.5) and

(4.6):

$$St_c = \ln(\delta_{i0}/\delta_m) = \ln(3) - 0.4 \ln(\varepsilon) = 1.0986 - 0.4 \ln(\varepsilon). \quad (4.12)$$

The critical Stokes number depends on the elasticity parameter, ε , which reveals the coupling of the lubrication force with the particle inertia and the elastic properties. McLaughlin (1968) reported a value of $St_c = 9.3$ for a steel sphere vertically colliding on a hardened steel anvil; the predicted critical Stokes number for this case is as low as $St_c = 4.84$.ⁱ Gondret et al. (2002) dropped steel spheres vertically towards an optical quality glass wall, and a critical Stokes number of $St_c \approx 11$ can be extrapolated from their results. However, equation (4.12) predicts $St_c = 5.3$ ⁱⁱ for this impact condition, a value that is again lower than the experimental result. With a pendulum apparatus, Joseph et al. (2001) were able to achieve immersed collisions with no gravity acting in the direction of impact and rebound. For collisions between glass spheres and a glass-like Zerodur wall, the predicted critical Stokes number is roughly $St_c \approx 6.7$ ⁱⁱⁱ but a value of $St_c = 9$ was found in the experiments. The prediction given by the EHL model is generally lower than

ⁱ McLaughlin: The liquid viscosity and density are $\mu = 2.39 \text{ Pa} \cdot \text{s}$ and $\rho_f = 1246 \text{ kg/m}^3$. The steel sphere diameter is 6.35 mm and the impact velocity is 0.41 m/s. The wall is made of hardened steel and assumed to have the same elastic material properties as the sphere: $E \approx 128 \text{ GPa}$ and $\nu \approx 0.286$. The elasticity parameter is $\varepsilon \approx 3.61 \times 10^{-4}$.

ⁱⁱ Gondret et al.: $\mu = 0.1 \text{ Pa} \cdot \text{s}$ and $\rho_f = 965 \text{ kg/m}^3$. The steel sphere of 5 mm has $E = 240 \text{ GPa}$, $\nu = 0.3$, and $\rho_s = 7800 \text{ kg/m}^3$. The glass wall has $E = 60 \text{ GPa}$ and $\nu = 0.24$. The elasticity parameter is $\varepsilon \approx 2.76 \times 10^{-5}$.

ⁱⁱⁱ Joseph et al.: $\mu = 1.29 \times 10^{-2} \text{ Pa} \cdot \text{s}$ and $\rho_f = 1163 \text{ kg/m}^3$. The glass sphere, of 6.35 mm diameter, has $E = 60 \text{ GPa}$, $\nu = 0.24$, and $\rho_s = 2540 \text{ kg/m}^3$. The Zerodur wall has $E = 91 \text{ GPa}$ and $\nu = 0.24$. The elasticity parameter is $\varepsilon \approx 7.73 \times 10^{-7}$.

the experiment results, which may be attributed to the debatable use of $\delta_{i0} = 0.01a$ when estimating the elasticity parameter.

More recently, Davis et al. (2002) proposed a different rebound distance, δ_r , by equating the elastic deformation force, $\delta_r \sqrt{2a\delta_r} / E^*$, with the lubrication force, $F_{\text{lub}} = 6\pi\mu a^2 U / \delta$, at $\delta = \delta_r$. Instead of solving equation (4.5), they arbitrarily chose $U = U_{i0}/2$ to estimate F_{lub} . The rebound distance was found to be:

$$\delta_r = 1.23 \delta_{i0} \varepsilon^{2/5}, \quad (4.13)$$

which differs from the minimum approaching distance, δ_m in equation (4.7) by a constant. This constant can be readily found as $\delta_r \approx 3.69\delta_m$. With the new rebound distance, the critical Stokes number can be estimated as:

$$St_c = \ln(\delta_{i0}/\delta_r) = -0.207 - 0.4 \ln(\varepsilon). \quad (4.14)$$

Equation (4.14) results in a smaller critical Stokes number than that obtained from equation (4.12), and thus yields a prediction that deviates even further from the experiment data. In addition to the uncertainty in the initial distance, $\delta_{i0} = 0.01a$, the arbitrary squeezing velocity $U = U_{i0}/2$ might raise other problems when using the EHL collision model. To avoid these issues, the experimental critical Stokes number was used when calculating the dissipation number in equation (4.11).

4.2.4 Alternative prediction of the coefficient of restitution

Instead of numerically solving the sphere motion with all the hydrodynamic forces, a theoretical prediction is possible if only the lubrication force is considered. Barnocky and Davis (1988) used equation (4.5) for the sphere approach velocity, assuming this value up to the rebound distance δ_c , as illustrated in figure 4.11(a). The instantaneous rebound velocity was calculated as:

$$U_r = -e_{dry} U_i = -e_{dry} \left[1 - \log\left(\frac{\delta_{i0}}{\delta_c}\right) / St_{i0} \right] U_{i0} , \quad (4.15)$$

assuming an asperity contact. Joseph et al. (2001) extended Barnocky's analysis to the rebound motion and obtained the rebound velocity:

$$\frac{U_{r0}}{U_{i0}} = \frac{U_r}{U_{i0}} - \log\left(\frac{\delta_{i0}}{\delta_c}\right) / St_{i0} , \quad (4.16)$$

after the sphere has bounced back to δ_{i0} , as shown in figure 4.11(b). Combining equations (4.16) and (4.5), the *effective coefficient of restitution*, $e = -U_{r0}/U_{i0}$, can be expressed as a function of e_{dry} , St_{i0} , and the length scale ratio δ_{i0}/δ_c as:

$$e_{EHL} = e_{dry} - \frac{1 + e_{dry}}{St_{i0}} \log\left(\frac{\delta_{i0}}{\delta_c}\right) . \quad (4.17)$$

The subscript ‘‘EHL’’ in equation (4.17) is used to denote the application of EHL theory.

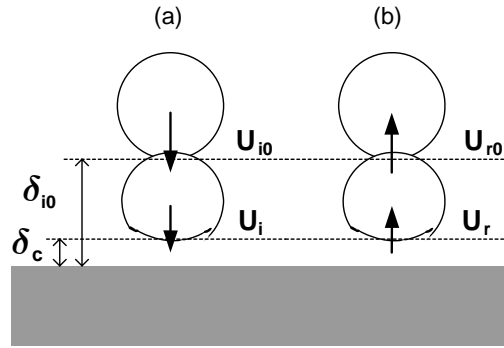


Figure 4.11. Schematic immersed collision process: (a) impact and (b) rebound.

More recently, Davis et al. (2002) used the new rebound distance, δ_r , to determine the instantaneous rebound velocity as given by equation (4.15). The wet coefficient of restitution was defined in terms of the quantities preceding the initial impact velocity U_{i0} as:

$$e_{wet} = e_{dry} \left(1 - \frac{\log(\delta_{i0}/\delta_r)}{St_{i0}} \right), \quad (4.18)$$

with which the immediate rebound velocity could be determined as $U_r = -e_{wet} U_{i0}$. This expression is similar to the instant rebound velocity, $U_r = -e_{dry} \eta U_i$, proposed in section 4.2.2 for a mixed contact. Therefore, a comparison of the predicted rebound motion with the two instantaneous rebound velocities will be presented in section 4.6, along with other simulation results.

4.3 Rebound in simulation

4.3.1 Summary of the rebound schemes

For each simulation, the impact velocity was first calculated and then used to estimate the minimum approaching distance, δ_m , given by equation (4.7). This distance was compared with the dry surface roughness, σ_s , to determine the contact mechanism, the rebound distance δ_c , and the rebound velocity U_r . The types of rebound schemes are summarized in Table 4.2.

Table 4.2. Summary of rebound mechanism for a fully immersed collision

Contact type		Criterion	Rebound distance δ_c	Rebound velocity
Asperity	Case I	$\sigma_s > \delta_m$	σ_s	$U_r = -e_{dry} U_i$
EHL	Case II	$\sigma_s < \delta_m$	δ_m	$U_r = -U_i$
Mixed	Case III	$\sigma_s \approx \delta_m$	$(1-k)\sigma_s$	$U_r = -e_{dry} \eta U_i$

For collisions of glass and steel spheres with impact velocities between 40 and 360 mm/s, the mean dry coefficient of restitution was found by Joseph et al. (2001) to be $\bar{e}_{dry} = 0.97 \pm 0.02$, without direct dependence on the impact velocity. Therefore, $e_{dry} = 0.97$ was used in the simulation.

4.3.2 Velocity at wall

The immersed pendulum motion, described by equations (4.3), is solved with a fourth-order Runge-Kutta method. Since uniform time steps are used, the sphere never reached

the rebound distance δ_c in an integral number of time steps. Thus, a proper extrapolation scheme is necessary to estimate the impact velocity and the corresponding hydrodynamic forces at δ_c . The fluid forces are singular at the wall, which makes conventional linear extrapolation inadequate for this estimation. To address this issue, Neville's algorithm is used (Press et al. 1996). As shown in figure 4.12, the sphere moves across the rebound distance, represented by the gray dashed line, from time step k to $k+1$, during this time the velocity drops dramatically from U_k^* to U_{k+1}^* due to the hydrodynamic forces. If the velocities at the five consecutive positions, δ_k^* to δ_{k-4}^* , prior to the rebound distances are used, Neville's extrapolation gives $U_i^* = 0.31$ at δ_c^* . However, if U_k^* and U_{k+1}^* are used to linearly interpolate the impact velocity, a smaller value, $U_i^* = 0.29$, is found. By reducing the time increment, the deviation between the two schemes can be reduced at the expense of computational overhead. Thus, Neville's algorithm is chosen for the current work and more details regarding the numerical method can be found in the reference. The impact time T_i is linearly interpolated as $T_i = t_N + (\delta_c^* - \delta_k^*)/U_k^*$.

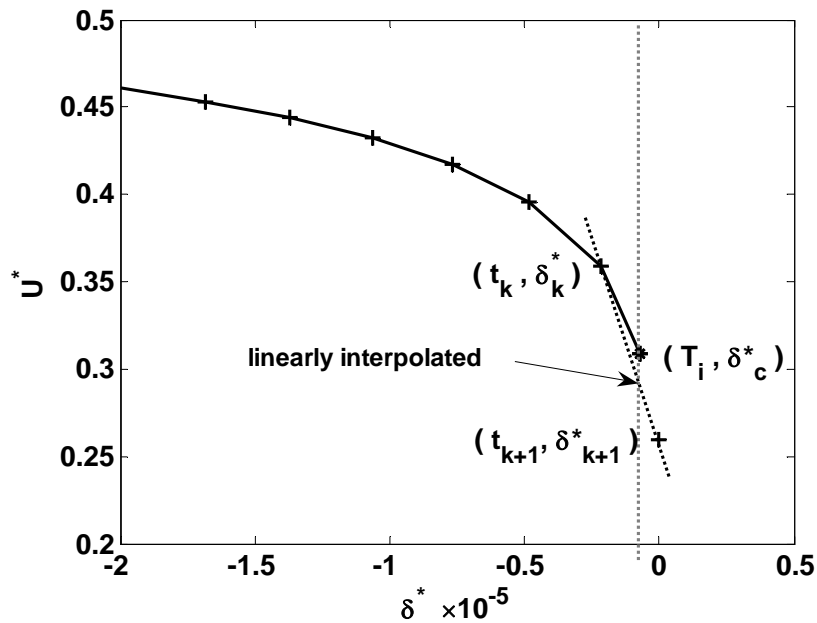


Figure 4.12. Extrapolation of the instant impact velocity is compared with the linearly interpolated value at the rebound distance.

4.3.3 Hertzian contact time and initial rebound condition

Once the sphere reaches the rebound distance, the restitution process commences and at least one Hertzian contact time, τ_H , elapses before the two spheres rebound from each other. If the sphere deformation remains fully elastic, the contact duration can be obtained as:

$$\tau_H = 2.87 \left[\frac{(\pi E^* m_p)^2}{a U_i} \right]^{1/5} .$$

An extended time is expected if plastic deformation occurs (Johnson 1985). When a 12.7 mm diameter steel ball bearing collides on a stationary Zerodur wall with an immediate impact velocity $U_i = 100$ mm/s, the contact duration is $\tau_H \approx 0.04$ ms which is beyond the resolution of the current image acquisition system. Thus, the sphere is made to rebound at T_i with a modified rebound velocity U_r in the simulation. The reversal of the sphere motion in zero time requires infinitely large impulse acting in the rebound direction. Such process takes at least half a Hertzian contact time in a real restitution process and this is not included in the current collision model. The estimated Hertzian contact time corresponds to 2 to 4 of the time steps used in the current simulation.

Moreover, at the point of rebound, the sphere has not yet departed from the wall. The momentarily ceased particle motion thus results in zero viscous drag. The instantaneous added mass force is also zero since the particle is not expelling any liquid. The history force, however, remains nonzero due to its effects accumulated from $t = 0$ to T_i .

4.4 Simulation results

To validate the proposed model for an immersed pendulum collision with a wall, the predicted trajectory was compared with the corresponding experiments conducted by Joseph (2003). In the simulations, all the material properties and the apparatus dimensions were set in accordance with the experiment setups, including the string length, the pendulum release angle, the liquid properties, and the size, the materials, and the surface properties of the spheres. The trajectories from a given simulation were processed in the same manner as in the experiments—a least-square fitting over the same period of time—to estimate the corresponding velocities. The quantity, Re_{exp} , denotes the impact Reynolds number based on an experimentally measured impact velocity. A predicted velocity was used to calculate Re_{sim} . Besides verifying the proposed collision model, the pendulum motions at various impact Reynolds and particle Stokes numbers were also investigated.

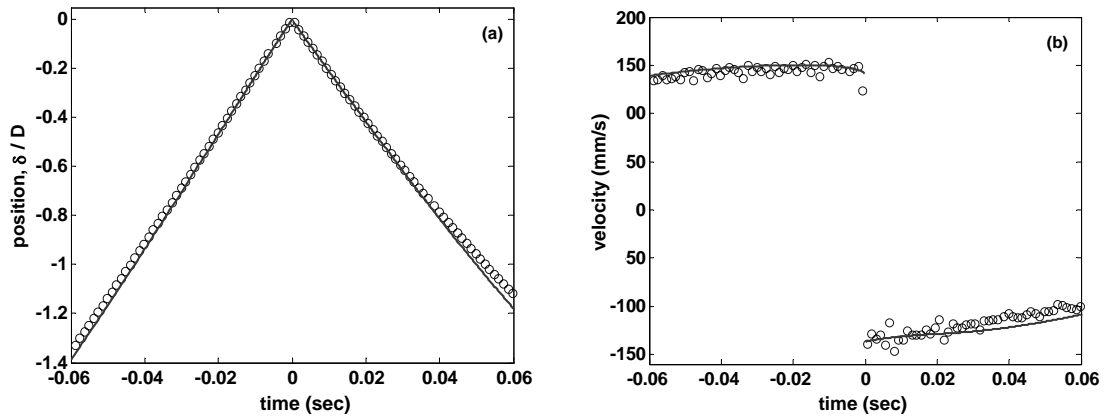
The results are categorized with respect to the contact mechanism: asperity, EHL, or mixed contacts. In each category, different impact Reynolds and particle Stokes number were simulated for those cases in which the experimental data were available. For a more concise documentation, the experiment impact velocity U_i , the liquid viscosity ν_f , and the solid-to-liquid density ratio ρ_s/ρ_f are summarized in a table for each case. Also included are Re_{exp} , Re_{sim} , St_{exp} , and St_{sim} . The predicted impact and rebound velocities were used to estimate the effective coefficient of restitution, $e_{\text{sim}} = -U_r/U_i$, the value of which is compared with the experiment result, e_{exp} , at the end of each subsection.

4.4.1 Asperity Contact at σ_s ; rebound with $U_r = -e_{dry}U_i$ ($e_{dry} = 0.97$)

(a) High impact Reynolds and Stokes numbers: ($Re = 970$, $St = 840$)

In figure 4.13, the collision of a steel ball bearing on a Zerodur wall in pure water ($22.5^\circ C$) is compared with the corresponding simulation result. The sphere is 12.7 mm in diameter and the pendulum release angle is $\theta = 10^\circ$. The steel ball bearing has a root-mean-square surface roughness of $\sigma_s = 2.36 \times 10^{-5}$ mm, which is greater than the estimated minimum approach distance, $\delta_m \approx 6.71 \times 10^{-6}$ mm. Therefore, the surface roughness is used to determine the rebound distance δ_c . The interfacial distance δ is scaled by the sphere diameter D .

U_{imp}^{exp} (mm/s)	viscosity ν_f (mm^2/s)	Re_{imp}^{exp}	Re_{imp}^{sim}	ρ_P / ρ_F	St_{imp}^{exp}	St_{imp}^{sim}
145	0.95	969	971	7.8	840	841.5



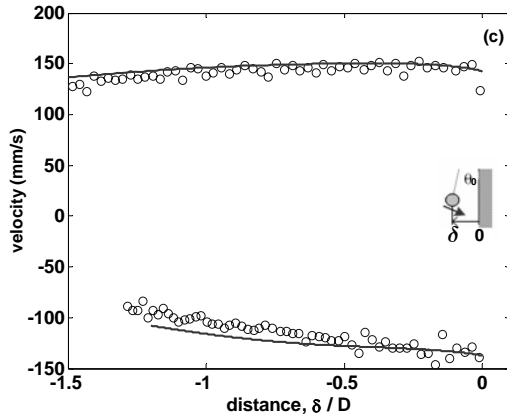


Figure 4.13. Time evolution of (a) sphere trajectory and (b) velocity perpendicular to the wall. (c) Velocity variation versus normalized distance from wall. The simulation result is indicated by the solid line while the experiment data are plotted with open circles.

The current model is able to reproduce the pendulum motion. However, a discrepancy in the rebound motion is observed when the sphere recedes to a distance of about $0.5D$ from the wall. Despite the discrepancy at later times, the predicted trajectory in figure 4.13(a), is in good agreement with the experiment up to 15 milliseconds after the collision, which is sufficient for the calculation of an effective coefficient of restitution. The experiment gives $e_{\text{exp}} = 0.91 \pm 0.005$ and $e_{\text{sim}} = 0.91 \pm 0.0024$ is determined from the model.

(b) High Reynolds number, moderate Stokes number: ($\text{Re} = 745$, $\text{St} = 211$)

A glass sphere of diameter 12.7 mm is released in pure water (25°C) at $\theta_0 = 12^\circ$. An asperity contact is ensured in this case as the surface roughness, $\sigma_s = 1.305 \times 10^{-4}$ mm, compares with minimum approach distance of $\delta_m \approx 1.51 \times 10^{-5}$ mm. The simulation results are plotted in figure 4.14 along with the experiment data.

$U_{\text{imp}}^{\text{exp}}$ (mm/s)	viscosity ν_f (mm^2/s)	$\text{Re}_{\text{imp}}^{\text{exp}}$	$\text{Re}_{\text{imp}}^{\text{sim}}$	ρ_P / ρ_F	$\text{St}_{\text{imp}}^{\text{exp}}$	$\text{St}_{\text{imp}}^{\text{sim}}$
106.7	0.896	756	758	2.55	214	214.8

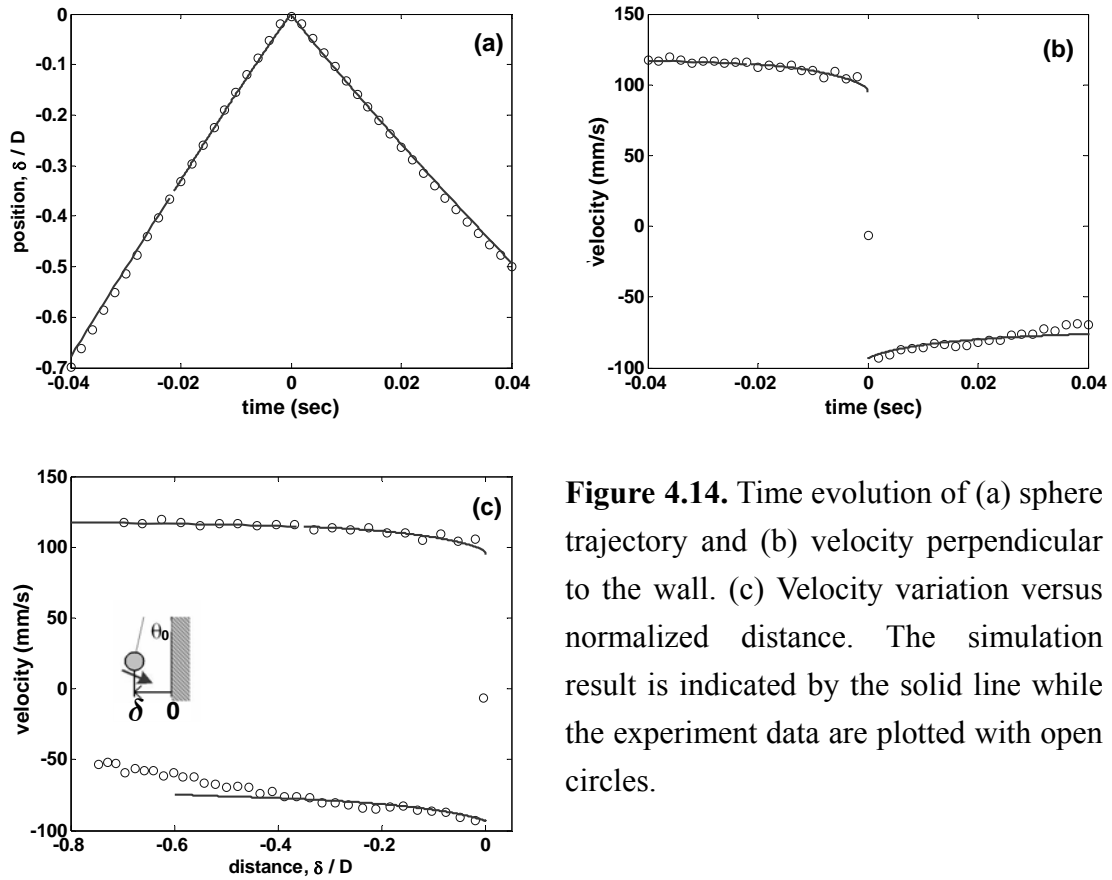


Figure 4.14. Time evolution of (a) sphere trajectory and (b) velocity perpendicular to the wall. (c) Velocity variation versus normalized distance. The simulation result is indicated by the solid line while the experiment data are plotted with open circles.

As the previous case, the incoming pendulum motion is captured by the current model. The simulated rebound motion also agrees with the experiment data until nearly 30 milliseconds after the collision, up to a distance of about $0.4D$ from the wall. The experimental effective coefficient of restitution is $e_{\text{exp}} = 0.83 \pm 0.0032$, which again agrees with the simulation result, $e_{\text{sim}} = 0.83 \pm 0.0015$.

(c) Moderate Reynolds number, low Stokes number: ($Re = 210$, $St = 56$)

A glass sphere ($D = 12.7$ mm) collides on the Zerodur wall in water-glycerol mixture at $24^\circ C$ from $\theta_0 = 20^\circ$. The minimum approach distance, $\delta_m = 1.69 \times 10^{-5}$ mm, is again an

order of magnitude smaller than the surface roughness, $\sigma_s = 1.305 \times 10^{-4}$ mm. Therefore, the asperity contact mechanism is responsible for the rebound of the sphere.

$U_{\text{imp}}^{\text{exp}}$ (mm/s)	viscosity ν_f (mm^2/s)	$\text{Re}_{\text{imp}}^{\text{exp}}$	$\text{Re}_{\text{imp}}^{\text{sim}}$	ρ_P/ρ_F	$St_{\text{imp}}^{\text{exp}}$	$St_{\text{imp}}^{\text{sim}}$
90.98	2.63	220	216	2.34	57.2	56.2

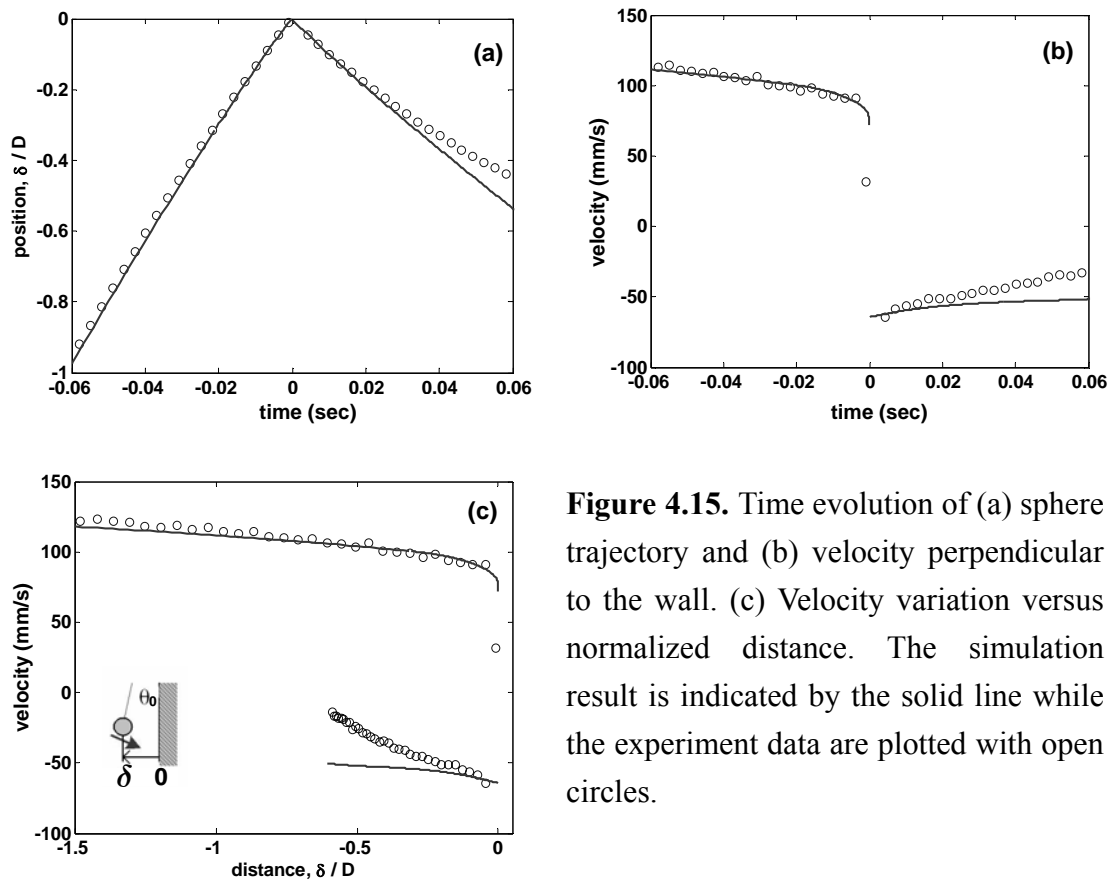


Figure 4.15. Time evolution of (a) sphere trajectory and (b) velocity perpendicular to the wall. (c) Velocity variation versus normalized distance. The simulation result is indicated by the solid line while the experiment data are plotted with open circles.

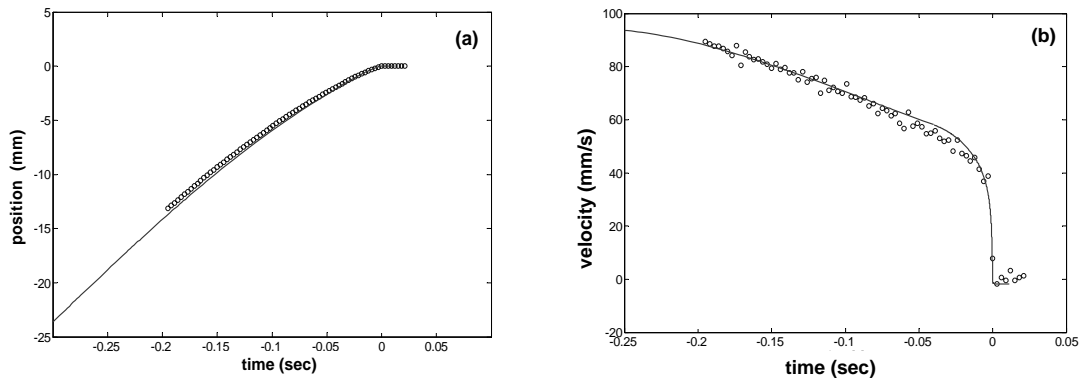
As the cases of higher impact Reynolds numbers, the current model predicts the incoming motion well. The rebound motion is also captured until roughly 10 milliseconds after the collision. However, the model underestimates the hydrodynamic forces and yields a velocity higher than the actual rebound motion, as shown in figures 4.15(b) and 4.15(c).

Possible explanations for this discrepancy will be presented in section 4.5. Nevertheless, the simulation gives an effective coefficient of restitution of $e_{\text{sim}} = 0.69 \pm 0.0033$ which is only 1.47 % higher than the experimental value of $e_{\text{exp}} = 0.68 \pm 0.0081$.

(d) Low Reynolds and Stokes numbers ($\text{Re} = 34$, $\text{St} = 8$)

A 12.7 mm glass sphere is released from $\theta_0 = 20^\circ$ in a viscous water-glycerol mixture at 24°C . An asperity height of $\delta_m = 2.3 \times 10^{-5}$ mm together with a minimum approach distance $\sigma_s = 1.305 \times 10^{-4}$ mm again ensures an asperity contact. As shown in figure 4.16, the pendulum motion is decelerated by the hydrodynamic forces and a full stoppage is predicted from the model, although a slight rebound is observed in the experiment. However, the small reverse velocity is too small to overcome the hindering hydrodynamic force and thus results in zero restitution, as predicted in the model.

$U_{\text{imp}}^{\text{exp}}$ (mm/s)	viscosity ν_f (mm^2/s)	$\text{Re}_{\text{imp}}^{\text{exp}}$	$\text{Re}_{\text{imp}}^{\text{sim}}$	ρ_P / ρ_F	$\text{St}_{\text{imp}}^{\text{exp}}$	$\text{St}_{\text{imp}}^{\text{sim}}$
50	7.46	33.5	35	2.19	8.2	8.5



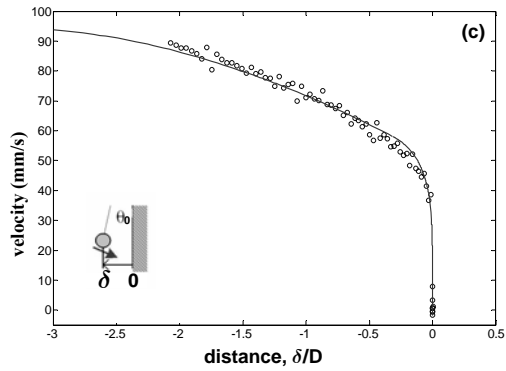


Figure 4.16. Time evolution of (a) sphere trajectory and (b) velocity perpendicular to the wall. (c) Velocity variation versus normalized distance. The simulation result is indicated by the solid line while the experiment data are plotted with open circles.

4.4.2 EHL contact at δ_m ; rebound with $U_r = -U_i$

Moderate Reynolds and Stokes number ($Re = 30$, $St = 21$)

The 12.7 mm steel ball bearing is released in water-glycerol mixture ($24^\circ C$) from $\theta_0 = 18^\circ$. For this particular impact condition, the minimum distance is found to be $\delta_m = 5 \times 10^{-5}$ mm, twice as thick as the dry surface asperity height, $\sigma_s = 2.36 \times 10^{-5}$ mm, resulting in an EHL contact. The simulation is presented with the experimental results in figure 4.17.

$U_{\text{imp}}^{\text{exp}}$ (mm/s)	viscosity ν_f (mm^2/s)	$Re_{\text{imp}}^{\text{exp}}$	$Re_{\text{imp}}^{\text{sim}}$	ρ_P / ρ_F	$St_{\text{imp}}^{\text{exp}}$	$St_{\text{imp}}^{\text{sim}}$
99	21.6	29.1	29.5	6.55	21.2	21.5

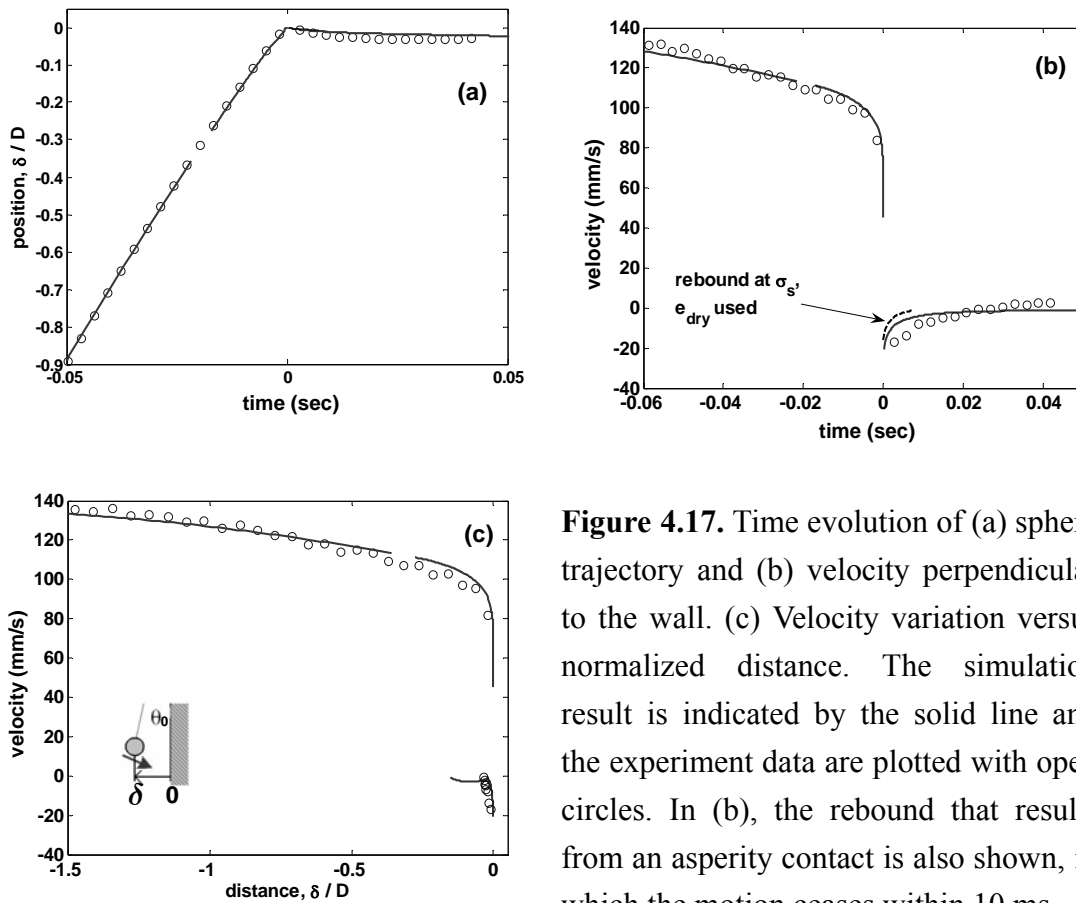


Figure 4.17. Time evolution of (a) sphere trajectory and (b) velocity perpendicular to the wall. (c) Velocity variation versus normalized distance. The simulation result is indicated by the solid line and the experiment data are plotted with open circles. In (b), the rebound that results from an asperity contact is also shown, in which the motion ceases within 10 ms.

Though the calculated impact motion corresponds with the experiment data, the predicted rebound ceases more quickly than the actual motion. This excessive deceleration is due to the singular hydrodynamic force at the wall that may over-decelerate the sphere motion if too small a rebound distance is used. The uncertainty in estimating δ_{i0} results in a questionable usage of δ_m as the rebound distance. An estimation using $\delta_{i0} = 0.01a$, that was suggested for particle motion at low Reynolds number, will result in a δ_m smaller than the estimation using $\delta_{i0} < 0.01a$. If the sphere is made to move to a distance smaller than the actual value in the simulation, the over-estimated hydrodynamic forces will result in an over-decelerated sphere motion. Nevertheless, for this impact condition, the minimum approach distance still exceeds the surface roughness. A complementary simulation made with asperity contact resulted in rebound motion in figure 4.17 (b) that

further deviates from the actual motion. The experimental effective coefficient of restitution is $e_{\text{exp}} = 0.14 \pm 0.023$ which means the prediction made by the simulation, $e_{\text{sim}} = 0.07 \pm 0.026$, is unrealistically small. Since this is the only set of experiments resulting in EHL contact, further investigation is required in order to validate the proposed contact mechanism.

4.4.3 Mixed contact at $(1-k)\sigma_s$; rebound with $U_r = -e_{\text{dry}} \times \eta \times U_i$

(a) Moderate Reynolds number and Stokes numbers ($\text{Re} = 180$, $\text{St} = 136$)

A 12.7 mm steel ball bearing is released from $\theta_0 = 20^\circ$ in a water-glycerol mixture at 24°C . The surface roughness of $\sigma_s = 2.36 \times 10^{-5}$ mm is comparable to the minimum separation, $\delta_m = 3.5 \times 10^{-5}$ mm, yielding a mixed contact. The sphere rebounds at a distance $\delta_c = (1-k)\sigma_s = 7\sigma_s/8$ with velocity $U_r = -e_{\text{dry}} \eta U_i$, where $\eta = 0.91$ from equation (4.11) with $\text{St}_c = 12$.

$U_{\text{imp}}^{\text{exp}}$ (mm/s)	viscosity ν_f (mm^2/s)	$\text{Re}_{\text{imp}}^{\text{exp}}$	$\text{Re}_{\text{imp}}^{\text{sim}}$	ρ_P / ρ_F	$\text{St}_{\text{imp}}^{\text{exp}}$	$\text{St}_{\text{imp}}^{\text{sim}}$
190.3	6.73	179.6	180.8	6.82	136.1	137

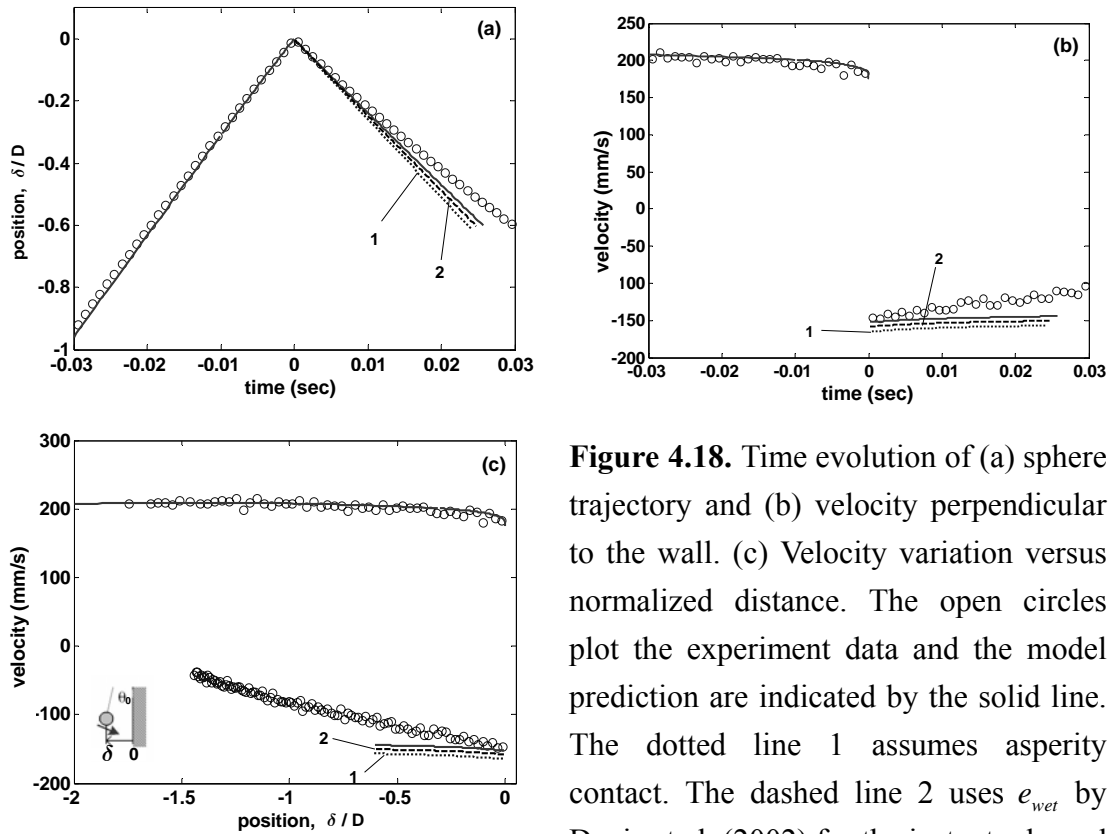


Figure 4.18. Time evolution of (a) sphere trajectory and (b) velocity perpendicular to the wall. (c) Velocity variation versus normalized distance. The open circles plot the experiment data and the model prediction are indicated by the solid line. The dotted line 1 assumes asperity contact. The dashed line 2 uses e_{wet} by Davis et al. (2002) for the instant rebound velocity.

As shown in figure 4.18, good agreement with the incoming pendulum is observed. However, the rebound motion deviates from the experiment data sooner than in the cases with asperity contact. The least-square curve fitting over ten milliseconds yields a value of $e_{sim} = 0.76 \pm 0.004$ that is higher than the experiment data $e_{exp} = 0.73 \pm 0.018$. To illustrate the importance of a proper contact mechanism, the sphere is also made to rebound as in an asperity contact; the results are shown by the dotted line 1, which determines $e_{sim1} = 0.82$ that deviate from e_{exp} . A second comparison is made using Davis coefficient of restitution, $e_{wet} = e_{dry} \times \eta$, to estimate the initial rebound velocity, $U_r = -e_{wet} \times U_{i0}$, in the simulation. The corresponding trajectories are shown by the dashed line 2. A second least-square curve fitting gives $e_{sim2} = 0.79$, which again exceeds the experimental value.

(b) Moderate Reynolds and Stokes numbers (Re = 90, St = 70)

A 12.7 mm steel ball bearing is released from a smaller release angle of $\theta_0 = 8^\circ$ in a water-glycerol mixture at $24^\circ C$. The minimum approach distance, $\delta_m = 2.68 \times 10^{-5}$ mm, is comparable to the surface roughness, $\sigma_s = 2.36 \times 10^{-5}$ mm, ensuring a mixed contact.

$U_{\text{imp}}^{\text{exp}}$ (mm/s)	viscosity ν_f (mm^2/s)	$\text{Re}_{\text{imp}}^{\text{exp}}$	$\text{Re}_{\text{imp}}^{\text{sim}}$	ρ_P/ρ_F	$St_{\text{imp}}^{\text{exp}}$	$St_{\text{imp}}^{\text{sim}}$
93.8	6.44	91.6	93	6.83	69.5	70.6

In figure 4.19, the predicted incoming motion, indicated by the solid line, agrees well with the experimental trajectory. With the mixed contact mechanism, the model is able to capture the rebound motion up to 20 milliseconds after collision. The predicted effective coefficient of restitution, $e_{\text{sim}} = 0.58 \pm 0.007$, agrees well with the experimental value, $e_{\text{exp}} = 0.59 \pm 0.002$. However, at later times, the model is inadequate for the pendulum motion. A simulation with asperity contact, shown by the dotted line 1, gives $e_{\text{sim1}} = 0.74$, the value of which exceeds e_{exp} by 27%. Usage of the Davis coefficient of restitution results in a different rebound trajectory, indicated by the dashed line 2, and the effective coefficient of restitution is found to be $e_{\text{sim2}} = 0.72$, disagreeing with the experimental result. For this impact, $\eta = 0.83$ from equation (4.11) using $St_c = 12$.

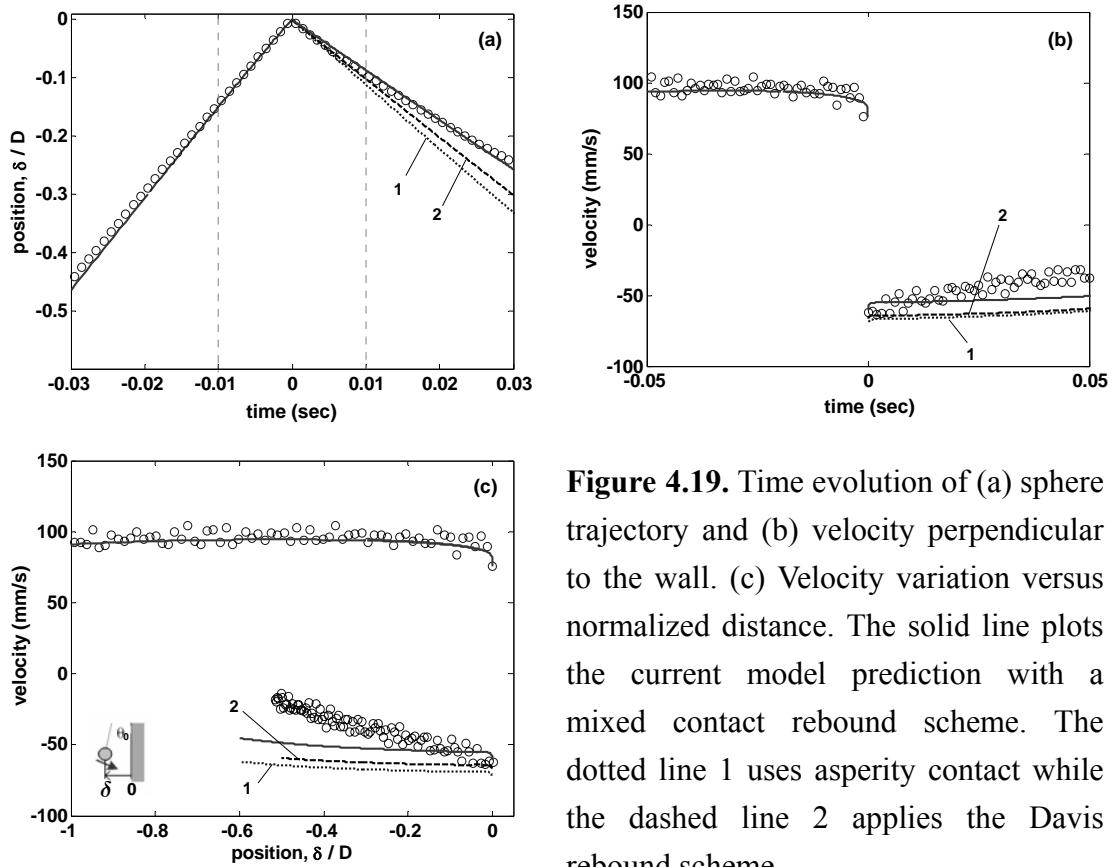


Figure 4.19. Time evolution of (a) sphere trajectory and (b) velocity perpendicular to the wall. (c) Velocity variation versus normalized distance. The solid line plots the current model prediction with a mixed contact rebound scheme. The dotted line 1 uses asperity contact while the dashed line 2 applies the Davis rebound scheme.

The large deviation from the experimental trajectory using asperity contact illustrates the importance of a correct contact model when the interstitial fluid is non-negligible. The proposed model, which assumes a quiescent ambient flow, cannot predict the long-term rebound trajectory. However, the near-wall post-collision trajectory is captured satisfactorily, which enables a reliable estimation of the effective coefficient of restitution that is important in real engineering problems.

4.5 Wake Structure

The main deficiency of the current model is the overestimated rebound speed when the sphere reverses its direction, which was observed in all the cases regardless of the rebound scheme. The discrepancy may be attributed to the assumption of a quiescent ambient flow that differs from the actual flow field.

As shown in figure 4.20, during the impact, an attached vortex ring is generated and attaches to the rear sphere surface. When the sphere collides with the wall, the vortex ring will move forward, stretch, and wrap around the sphere due to its own inertia. Therefore, the sphere rebounds into a wake in which the fluid motion is far from quiescent. Higher viscous dissipation is expected in the real flow than the value estimated in the current hydrodynamic model. The effects of the ambient wake and the induced flow field on the rebound trajectory will be more pronounced when the sphere rebounds with less inertia. The model prediction hence deviates increasingly from the real rebound trajectory with decreasing particle Stokes number.

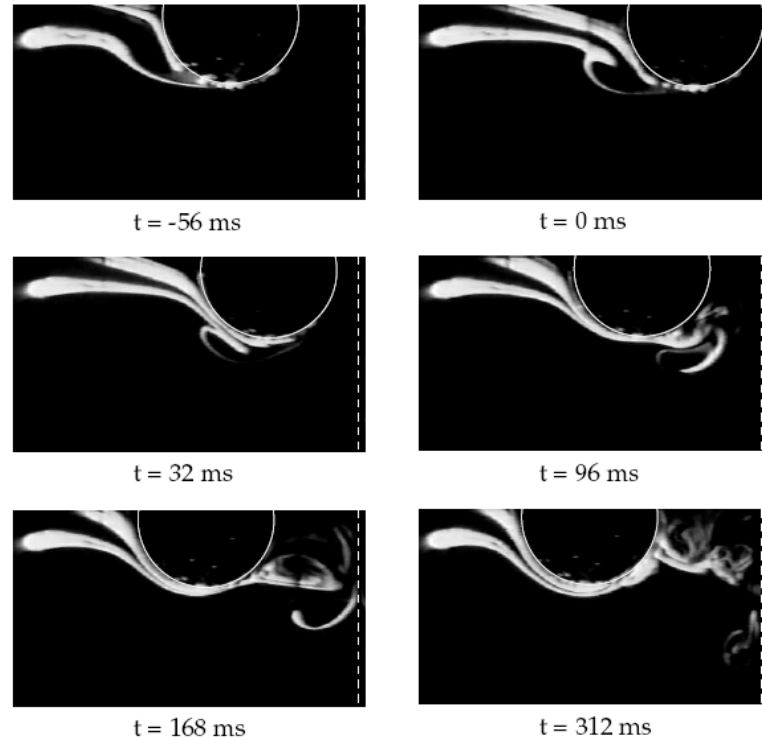


Figure 4.20. Flow visualization of a particle-wall immersed collision. A 12.7mm diameter Delrin collides on the Zerodur wall at $St_i \approx 210$ and $Re_i \approx 770$. The wall is indicated with the dashed line on the right of each frame. A complicated vortical flow structure around the sphere is observed after collision at $t = 0$ (Joseph 2003).

4.6 Prediction of the effective coefficient of restitution

In section 4.4, the general agreement between the simulation results and the corresponding experiment data validated the hydrodynamic model described in chapter 3 as well as the proposed contact mechanisms. The model can then be applied to estimate the effective coefficient of restitution in a general immersed collision, which is the ultimate goal of the current work. By changing the liquid viscosity, the solid to liquid density ratio, the particle size, and the pendulum release angle, various impact Stokes numbers were achieved in the current computation. Since the contact mechanism is

highly dependent on the solid elasticity and the particle surface property, the comparison is made for a glass or steel impact sphere separately.

4.6.1 Collision of glass spheres on the Zerodur wall

The first comparison with the experiment data is made using glass spheres of diameter 4.00, 6.00, and 6.35 mm. The root-mean-square surface roughness is $\sigma_s \approx 0.051\mu\text{m}$ for the 4.00 mm sphere and $0.135\mu\text{m}$ for the other two (Joseph 2003). The simulation was conducted using an asperity height and a radius that together yielded an asperity ratio of $\sigma_s/a = 2 \times 10^{-5}$, corresponding to that of the actual glass spheres. The predicted effective coefficient of restitution is plotted with the experiment data in figure 4.21. Also shown is the prediction by the EHL collision model, namely equation (4.17) with $e_{dry} = 0.97$. Since the glass spheres possess high surface roughness, an asperity contact was used to rebound the sphere. No further efforts were made to verify the contact mechanism by comparing the minimum approach distance with the asperity height prior to collision.

As shown in figure 4.21, the prediction from the current model (Δ) is in acceptable agreement with the experiment data (\circ , \square , and \diamond). The e_{EHL} predictions are plotted in dashed lines for different δ_c/δ_{i0} ratios. Joseph (2003) comments that using a value of $\delta_c/\delta_{i0} = 10^{-3}$ provides the best fit to the experiment data. When the impact Stokes number is greater than 50, the EHL collision model with $\delta_c/\delta_{i0} = 10^{-3}$ predicts a higher restitution than both the experimental data and the current model findings. The reason for this overestimation of e in the EHL collision model may result from the neglecting of the wall-modified added mass force. Hence, less kinetic energy is lost in the EHL collision model than in the current model, which results in a higher restitution. At lower particle Stokes numbers, the e_{EHL} prediction drops below the experimental data while the current

collision model predicts a matching restitution. The fluid affects the particle motion and surface deformation more significantly at a smaller particle Stokes number, where mixed contact may occur besides of the investigated asperity contact.

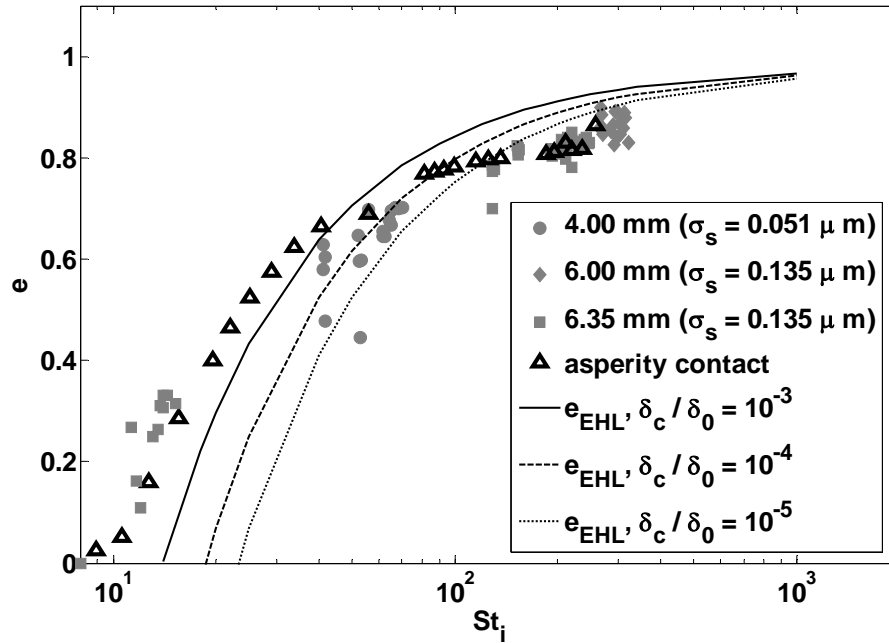


Figure 4.21. Comparison of the predicted effective coefficient of restitution for fully immersed collisions between glass spheres and the Zerodur wall.

4.6.2 Collision of steel spheres on the Zerodur wall

Due to the small surface roughness, $\sigma_s = 0.024 \mu\text{m}$, of the steel ball bearings, both asperity and mixed contact rebound schemes were examined with the experimental data in figure 4.22. Under identical impact conditions, asperity contact results in higher restitution than mixed contact. The comparison with the experimental data suggests the presence of different contact mechanisms at different particle Stokes numbers.

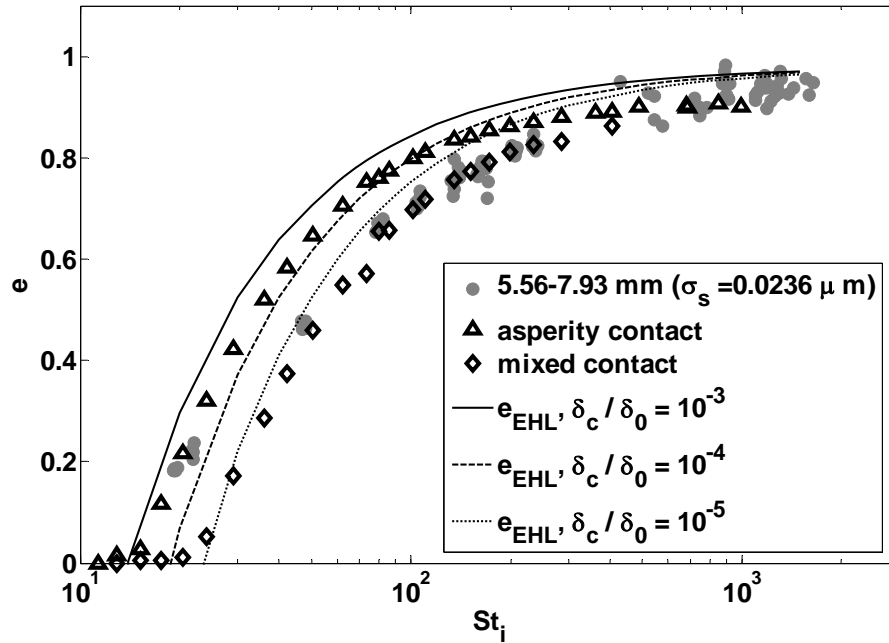


Figure 4.22. Comparison of the predicted effective coefficient of restitution for fully immersed collisions between steel ball bearings and the Zerodur wall. Both asperity and mixed contact rebound schemes are applied.

As shown in figure 4.22, for $St_i > 400$, the model predictions with asperity contact shows reasonable agreement with actual collisions, as in the case of glass collisions. Between $St_i = 50 - 400$, the lubrication layer may become comparable to the asperity height and using a mixed contact rebound scheme provides a better fit than using asperity contact. At $St \approx 20$, asperity contact begins to occur, as indicated by the collapse of the experiment data with the model predictions at low particle Stokes numbers. This might be attributed to δ_m decreasing with decreasing impact velocity, the dependence of which can be found as $\delta_m \sim U_i^{7/5}$ using equations (4.6) and (4.7) if all other parameters are kept the same.

It has been noted in both chapter 2 and in the experimental literature that a general trend of the correlation between the effective coefficient of restitution and the particle Stokes

number is found from the experiments. Such monotonic dependence is predicted in both the EHL and the current collision model. However, a careful examination of the current simulation results reveals the importance of the rebound scheme. Employed with identical impact conditions, the rebound velocity from a mixed contact is always lower than that from an asperity contact due to the additional energy loss in the inter-asperity liquid. When the simulation results are plotted together, as in figure 4.23, it may be seen that glass spheres retain higher restitution than steel ball bearings at the same particle Stokes number. Comparing the two asperity contacts, glass spheres with rougher surfaces than steel ball bearings rebound at greater interstitial distances. Since the hydrodynamic forces are singular at zero gap, rebound at a larger separation assures less hindering forces. Therefore, for asperity contact, a higher restitution should be expected for rough particles than polished ones if the impacts occur at identical particle Stokes numbers.

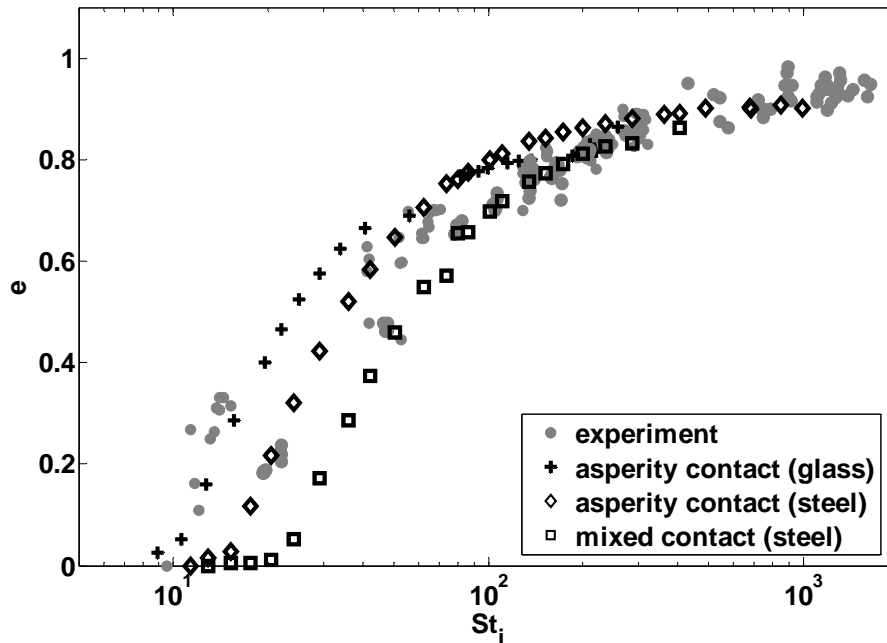


Figure 4.23. The experimental effective coefficient of restitution is compared with the predictions from the current model with different rebound schemes.

4.7 Summary

A set of equations is proposed for the collision of a fully immersed pendulum sphere on a stationary flat wall. Good agreement is observed between the model prediction and the experiment data, indicating that the model is adequate to describe the incoming sphere motion over a wide range of Reynolds and particle Stokes numbers. Three rebound mechanisms are proposed by comparing the dry surface asperity height with the EHL minimum approach distance. When a pseudo-dry contact is ensured by large surface roughness, the sphere rebounds at a velocity that is reduced by the dry coefficient of restitution. The resulting rebound trajectory compares well with experiments, validating the prediction of the effective coefficient of restitution using the current collision model.

However, when the EHL minimum approach distance exceeds or equals the surface roughness, an EHL or a mixed contact occurs. When the surface asperity deforms by the compression impulse, additional particle kinetic energy is lost into the inter-asperity liquid. In addition to the loss in the solid phase, a dissipation parameter, which depends on the ratio of the critical Stokes number to the impact Stokes number, is proposed to characterize such dissipation. The actual rebound trajectory is captured over a period long enough to obtain a reasonable estimate of the effective coefficient of restitution. The predicted rebound motions deviate more at later times than those for an asperity contact, due to less rebound inertia. Despite this discrepancy in the far-field velocity profile, the predicted effective coefficient of restitution is in general agreement with the experimental findings over a wide range of impact conditions for smooth particles.

A possible explanation for the over-estimated rebound velocity in the current model, regardless of the contact mechanism, is the neglecting of the actual flow structure induced by the impact motion. For a real collision in liquid, a vortex ring is formed by the

impact sphere motion and its interaction with the rebound sphere generates a complicated flow structure in the surrounding liquid. This induced flow field contradicts the quiescent ambient flow condition assumed in the current hydrodynamic model. The neglecting of the actual vortical flow underestimates the viscous dissipation and results in a faster rebound speed in the long term. A good model for such additional dissipation should improve the predicted rebound motion. Besides the omission of the ambient flow structure, the proposed collision model does not incorporate the time required for solid deformation. The Hertz elastic contact time determines the least duration and is found to be small enough to validate the zero time approximation in the current collision model, for collisions between steel and glass materials. However, longer contact duration than a Hertzian time should be expected when plastic deformation commences. Under such circumstances, a better estimation of the contact time is required and in the simulation, the rebound time should be shifted to accommodate the occurrence of such a slow solid deformation.

Chapter 5

Oblique Collision Between Two Spheres in a Liquid

The immersed normal collision between two solid surfaces was investigated in the previous chapters. The experimental apparatus was specifically designed to ensure an in-plane collision where the contact force goes through the sphere centers affecting only the sphere translation that is constrained to two dimensions. However, such a controlled interaction seldom occurs in reality, where the impact sphere can impart torque on the target resulting in the sideways motion or rotation of the target sphere. Thus oblique collisions between identical spheres were experimentally investigated in this chapter in an attempt to understand the rich behavior of a general inter-particle immersed collision.

5.1 Background

5.1.1 Normal component of motion

Joseph and Hunt (2004) conducted the experiments of fully immersed oblique collisions between a sphere and a stationary wall. At the sphere center of mass, the sphere motion was decomposed into a normal and a tangential component with respect to the normal of the wall in figure 5.1. They define the normal coefficient of restitution, $e_n = -U_m/U_{in}$, as

the ratio of the normal components of the rebound and the impact velocities. The normal particle Stokes number, $St_n = St \cos \theta_i$, is calculated by equation (2.9) using the normal component of the impact velocity.

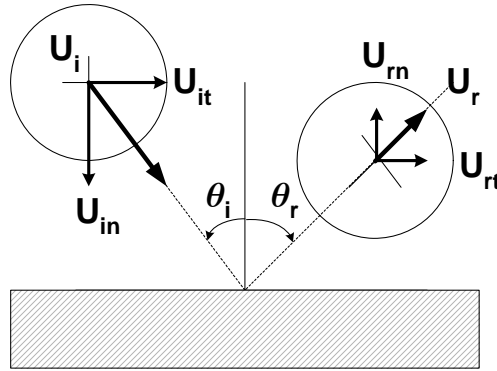


Figure 5.1. Schematic representation of the sphere-on-wall oblique collision and the relevant parameters. For both the impact and the rebound motion, indicating by $j = i, r$, $U_{jn} = U_j \cos \theta_j$ and $U_{jt} = U_j \sin \theta_j$.

The correlation between the two parameters exhibits similar behavior to that discovered in head-on collisions, the correlation of which is reproduced in figure 5.2. The same trend was also observed by Kantak and Davis (2004) where a sphere was dropped onto a tilted wall layered with a lubricant film. Within the range of normal Stokes number examined in their work, $0 < St_n < 30$, the normal coefficient of restitution was also found to decrease monotonically with diminishing normal particle Stokes number without noticeable effects from the impact angle θ_i . Kantak and Davis (2004) thus concluded that the normal component of an oblique collision is independent of the tangential motion. This experimental finding may be used to support the assumption by Joseph and Hunt (2004) that the tangential interaction between the two surfaces is not significantly affected by the surface deformation in the normal direction.

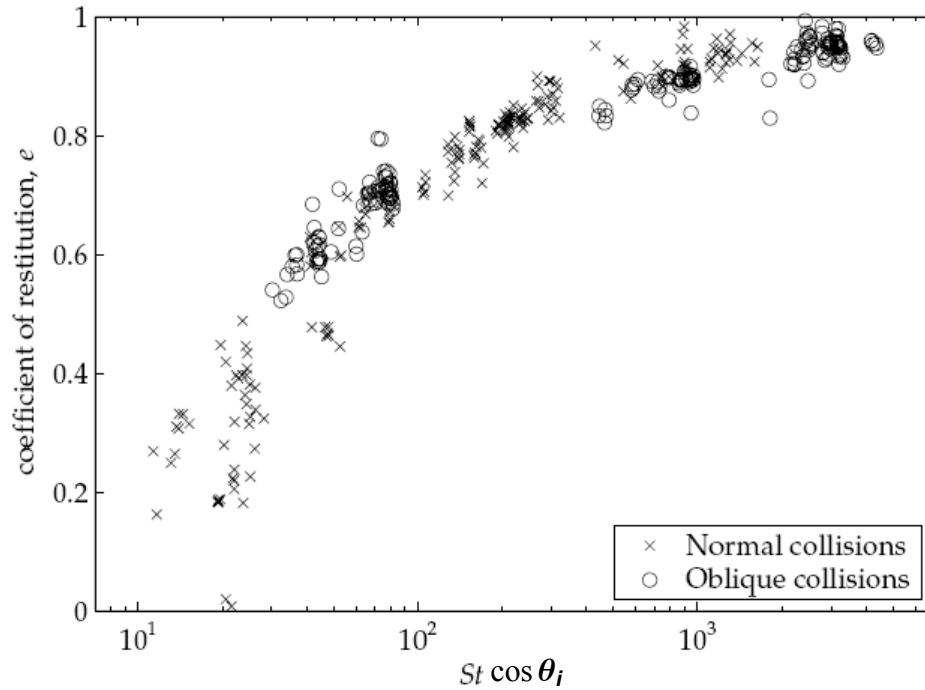


Figure 5.2. Normal coefficient of restitution as a function of normal particle Stokes number for oblique collisions in aqueous solutions of glycerol (Joseph and Hunt 2004).

5.1.2 Tangential component of motion

(a) At the contact point

To characterize the tangential interaction during impact, Joseph and Hunt (2004) compared their experimental results to a dry collision model by Maw et al. (1976). Two dimensionless parameters are proposed in the model to characterize the dependence of the rebound angle on the tangential compliance developed over the contact area for a general dry oblique collision. The first parameter is the *modified radius of gyration*,

$$\chi = \frac{(1-\nu)(1+1/K^2)}{(2-\nu)},$$

where the radius of gyration, $K = (I/m_p a^2)^{1/2}$ depends on the moment of inertia I , the mass m_p , and the characteristic radius a of the object. The second parameter, the *non-dimensional angle of incidence*, is defined as

$$\psi_i = \frac{2(1-\nu)}{\mu_C(2-\nu)} \frac{U_{it,cp}}{U_{in}}, \quad (5.1a)$$

which depends on the Poisson's ratio ν , the Coulomb friction coefficient μ_C , the impact normal and the tangential velocities, U_{in} and $U_{it,cp}$, at the *contact point* upon impact. The impact tangential velocity, $U_{it,cp} = U_{it} + a\omega_i$, depends on both the tangential and angular velocities at the sphere center of mass, U_{it} and ω_i . Similarly, the *non-dimensional angle of reflection* can be calculated as

$$\psi_r = \frac{2(1-\nu)}{\mu_C(2-\nu)} \frac{U_{rt,cp}}{U_{in}}, \quad (5.1b)$$

using the tangential rebound velocity, $U_{rt,cp} = U_{rt} + a\omega_r$, at the contact point using the rebound tangential and angular velocities at sphere center. By plotting ψ_r with respect to ψ_i , Maw et al. found general agreement between their three-dimensional numerical simulation and the nearly two-dimensional experiments on the dry oblique collision between a disk and a wall. Kharaz et al. (2001) experimentally investigated the collision of an elastic sphere on a wall whose rebound motion corresponds to Maw's prediction and is illustrated in figure 5.3.

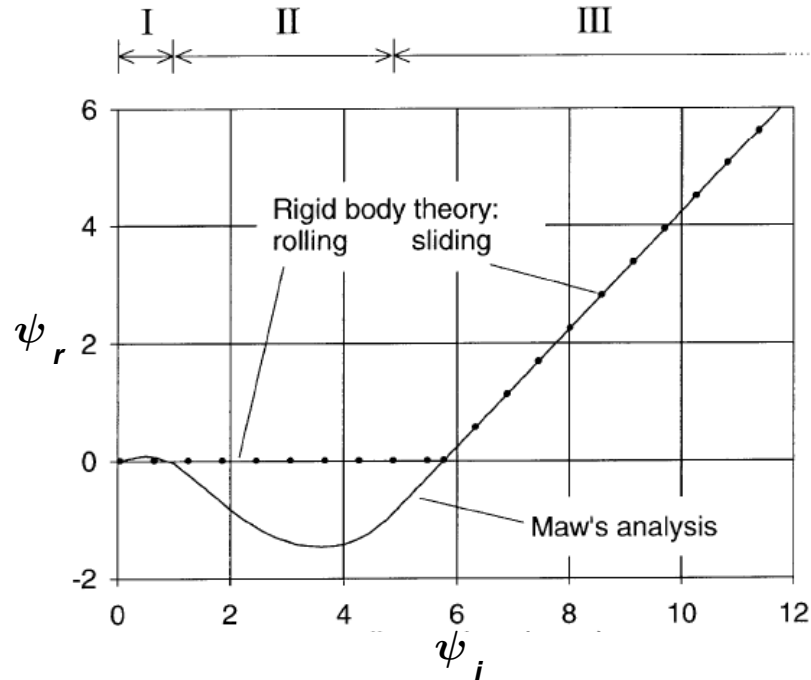


Figure 5.3. Non-dimensional angle of reflection, ψ_r , as a function of the angle of incidence, ψ_i . This is a reproduction of Figure 3 in Kharaz et al (2001).

For an oblique collision with $\psi_i \leq 1$, which corresponds to regime I in figure 5.3, the sphere sticks to the wall when the surface is deformed by the normal compression impulse. After the maximum compression, the elastic strain is recovered causing the sphere to rebound in the normal direction. During the restitution process, the tangential compliance results in an annulus of micro-slip that spreads inwards until it covers the whole contact area establishing gross slip. If the sphere collides with an incidence angle $1 < \psi_i < 4\chi - 1$ in regime II, the impact commences with tangential gross slip. Under the Coulomb friction, the relative velocity between the two surfaces decreases to zero and the tangential contact mechanism changes immediately from gross slip to complete sticking. The subsequent surface interaction then follows the process in regime I. For a collision in regime III where $\psi_i \geq 4\chi - 1$, unidirectional gross slip continues through the whole collision process corresponding to a rigid body sliding. The dry friction coefficient can be estimated by solving the equation of motion at the contact

point in the tangential direction with respect to different tangential contact mechanisms. When impact occurs with gross slip, $\psi_i \geq 4\chi - 1$, the friction coefficient can be estimated by:

$$\mu_C = \frac{U_{rt,cp} - U_{it,cp}}{2(1 + 1/K^2)U_{in}}, \quad (5.2)$$

using the tangential velocities at the contact point before and after the collision, $U_{it,cp}$ and $U_{rt,cp}$ (Maw et al. 1981). For impact involving sticking, the friction coefficient can be estimated by

$$\mu_C = \frac{U_{rt,cp} - U_{t,cp}(t^*)}{2(1 + \cos(\omega_t t^*))U_{in}},$$

with a characteristic time t^* that depends on the surface deformation, the normal and the tangential compliances within the contact area, the radius of gyration, and the mass of the sphere. The friction coefficient also depends on the characteristic frequency ω_t which is another function of the sphere mass and the tangential compliance in the contact area. More details can be found in Maio and Renzo (2004) where a linearized collision model for a frictional-elastic dry collision between spheres is developed.

However, when oblique collisions occur in a liquid, the effective friction coefficient μ_C can change dramatically. Joseph and Hunt measured the *effective angle of incidence and rebound*, $\Psi_i = U_{it,cp}/U_{in}$ and $\Psi_r = U_{rt,cp}/U_{in}$, to estimate μ_C for immersed oblique collisions using equation (5.2). The friction coefficient is in general lower than the value between the corresponding dry surfaces due to the interstitial liquids. The dry friction coefficient between Zerodur wall and the same steel ball bearing used in the current work was measured to be $\mu_{dry} = 0.11 \pm 0.003$. The coefficient drops to $\mu_C \approx 0.02$ when the

collision occurs in liquid. A slight increase in the friction coefficient is observed with increasing tangential Stokes number, $St_t = St \sin \theta_i$, as shown in figure 5.4. Since the shearing lubrication force depends linearly on the surface relative velocity, a more frictional interaction is observed at higher St_t due to greater relative tangential velocity. Joseph (2003) also attributed the rising lubrication force to a thinner liquid film due to a greater impact angle. For collisions of rough glass particles, the liquid may be confined between the surface asperities. Upon the squeezing surface motion, the hydrodynamic pressure of the trapped liquid increases locally changing μ_c dramatically to a value that corresponds to the measurements between dry glass surfaces.

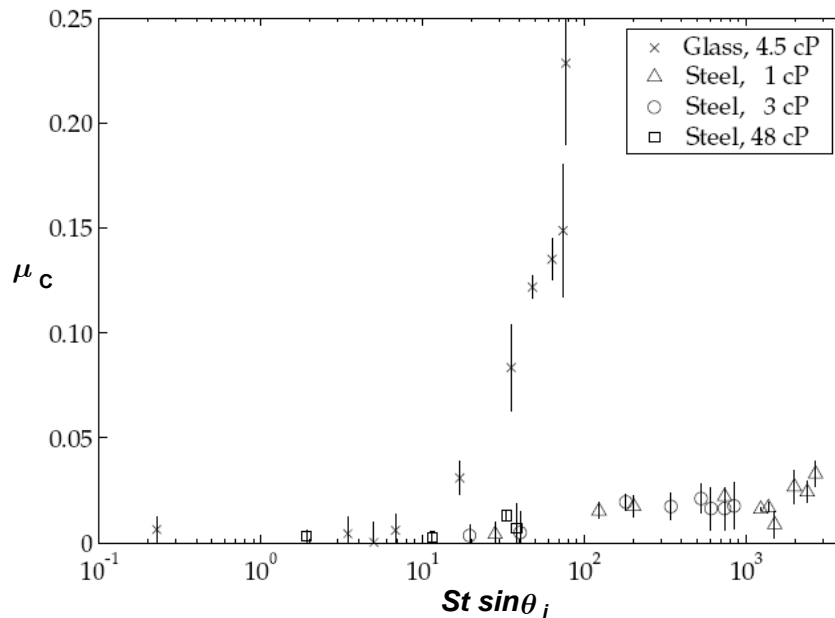


Figure 5.4. Effective friction coefficient, μ_c , as a function of tangential impact Stokes number, $St_t = St \sin \theta_i$, for an immersed oblique collision of different spheres. This is a reproduction of Figure 4.16 of Joseph (2003).

With the effective friction coefficient, Joseph and Hunt (2004) discovered a similar dependence of ψ_r on ψ_i to that observed in a dry system, as shown in figure 5.5. The agreement suggests that the tangential surface interaction during an immersed oblique

collision can be described as a dry system with the premise that the effective friction coefficient, μ_c , can be properly estimated for the interstitial liquid effects.

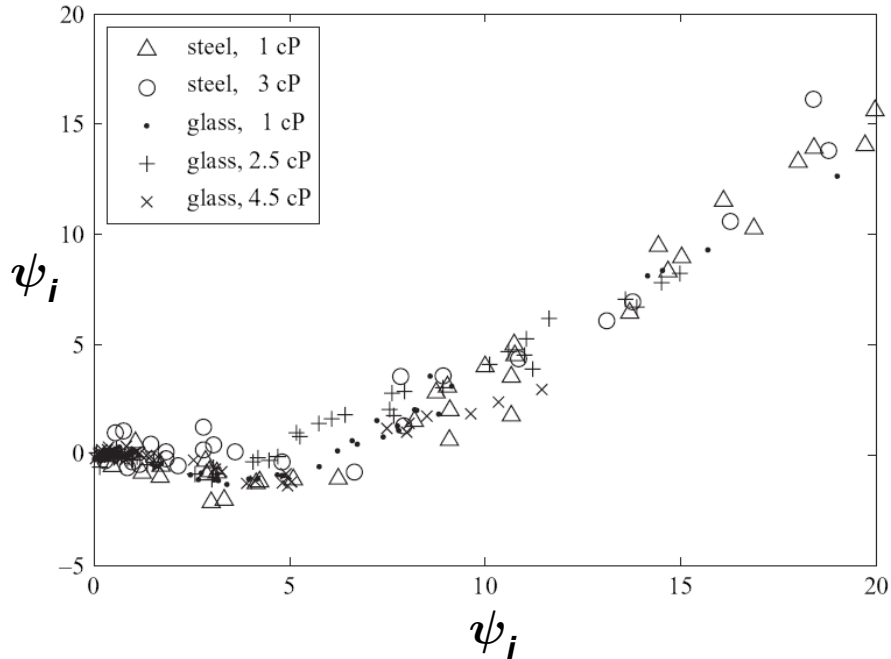


Figure 5.5. Non-dimensional angle of reflection, ψ_r , as a function of incidence angle, ψ_i , for an oblique particle-wall collision in a glycerol-water mixture. This is reproduced from Figure 12 of Joseph and Hunt (2004).

(b) At the center of mass

Besides the properties at the contact point, the tangential motion at the sphere center of mass provides a second method to investigate the tangential surface interaction. Conventionally, the *contact normal* is defined by the line of centers upon impact, as shown in figure 5.6, which serves as the reference for motion decomposition. The normal and tangential impulses act at the contact point and alter the linear and angular velocities of each sphere at their centers of mass. As delineated in chapter 2, the sphere motion after

a head-on dry collision can be fully described using Poisson's hypothesis as the required additional equation. However, for an oblique collision, the normal and the tangential components of motion are coupled through Coulomb's friction law. The two spheres may interact with initial sticking or sliding in the tangential direction resulting in different normal and tangential compliances in the contact area. Thus the two spheres rebound at different velocities and angles correspondingly. As shown in figure 5.6, when the lower sphere impacts a stationary target with velocities U_{i1} and ω_{i1} at an impact angle θ_{i1} from the contact normal, the rebound angles of each sphere can be found as follows (Goldsmith 1961).

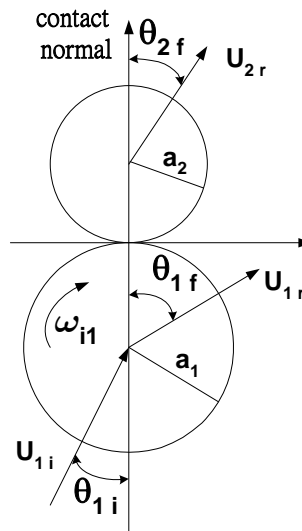


Figure 5.6. Impact of two spheres in a plane motion.

If the surface motion involves sticking, which corresponds to a contact point motion in regime I or II of Maw's model, the post-collision normal and tangential velocities can be found as:

$$U_{r1n} = \frac{M - e}{M + 1} U_{i1n}, \quad (5.3a)$$

$$U_{r2n} = \frac{M}{M+1}(1+e)U_{in}, \quad (5.3b)$$

$$U_{r1t} = \frac{M + \frac{5}{7}}{M+1}U_{it} - \frac{2}{7} \frac{a\omega_{i1}}{M+1}, \quad (5.3c)$$

$$U_{r2t} = \frac{2}{7} \frac{M}{M+1}(U_{it} + a\omega_{i1}). \quad (5.3d)$$

The rebound motion depends on the normal impact velocity U_{in} , the impact angular velocity ω_{i1} , and the mass ratio $M = m_1/m_2$. The quantity e is the dry normal coefficient of restitution. Dividing the tangential velocity by the normal component yields the tangents of the rebound angle for both spheres as:

$$\tan \theta_{r1} = \frac{M + \frac{5}{7}}{M - e} \tan \theta_{i1} - \frac{2}{7(M - e)} \frac{a_1 \omega_{i1}}{U_{in}}, \quad (5.3e)$$

$$\tan \theta_{r2} = \frac{2}{7(1+e)} \left[\tan \theta_{i1} + \frac{a_1 \omega_{i1}}{U_{in}} \right], \quad (5.3f)$$

which also depend on the impact angle θ_{i1} . This sticking contact will be referred as *GS1 collision model* hereafter.

For collision at greater impact angle, the sphere surfaces slide on each other corresponding to a contact point motion in Maw's regime III. The friction force changes the tangential velocities and the rebound angle after collision into:

$$U_{r1t} = U_{it} - \mu_C \frac{1+e}{M+1} U_{in}, \quad (5.4a)$$

$$U_{r2t} = \frac{M}{M+1} \mu_C (1+e) U_{in}, \quad (5.4b)$$

$$\tan \theta_{r1} = \frac{M+1}{M-e} \tan \theta_{i1} - \mu_C \frac{1+e}{M-e}, \quad (5.4c)$$

$$\tan \theta_{r2} = \mu_C, \quad (5.4d)$$

involving a friction coefficient μ_C ; this model will be denoted as *GS2 collision model*.

The normal rebound velocities, U_{r1n} and U_{r2n} , are the same from both models.

5.2 Experiment setup

5.2.1 Apparatus

The fixture plate used in the experiment of particle-on-particle immersed normal collision was modified to allow oblique collisions. Along the slot for the target sphere, five consecutive holes were drilled 1.5 mm apart, as depicted in figure 5.7(a). By locating the target string in different positions, oblique collisions could be achieved in a specific orientation. The 0-position was located along the plate centerline, resulting in the configuration for normal collisions as used in chapter 2. As shown in figure 5.7(b), the smallest impact angle in the current setup was achieved by a 0-1 formation where the impact sphere swings along the plate center line while the target sphere was suspended 1-position. The largest impact angle, $\theta_{i1} \approx 60^\circ$, was achieved using a 0-3 formation. The bottom view of the particles was recorded for the lateral motion. The marker on the bottom surface was used to track the sphere rotation necessitating direct illumination. A typical image is shown in figure 5.7(c).

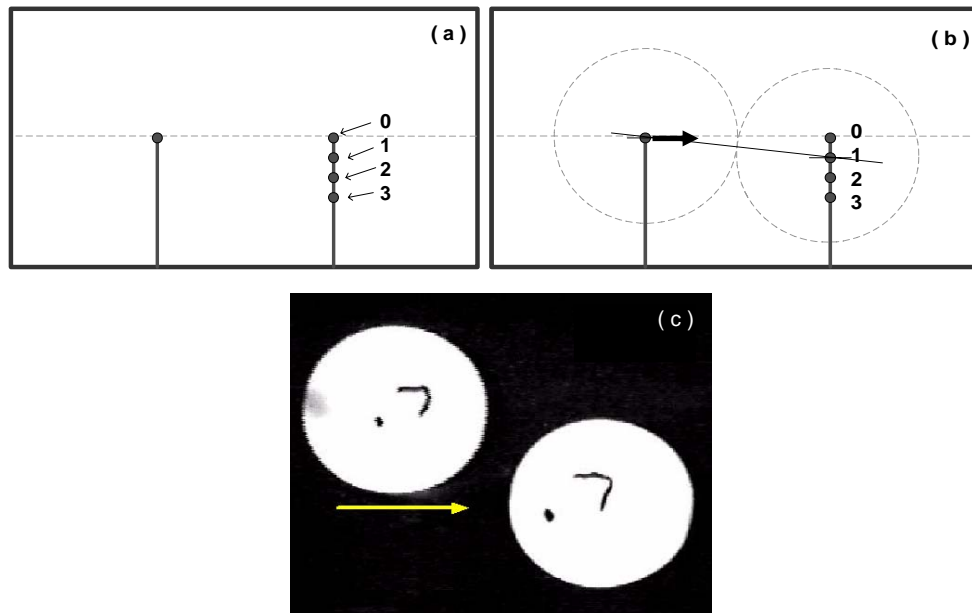
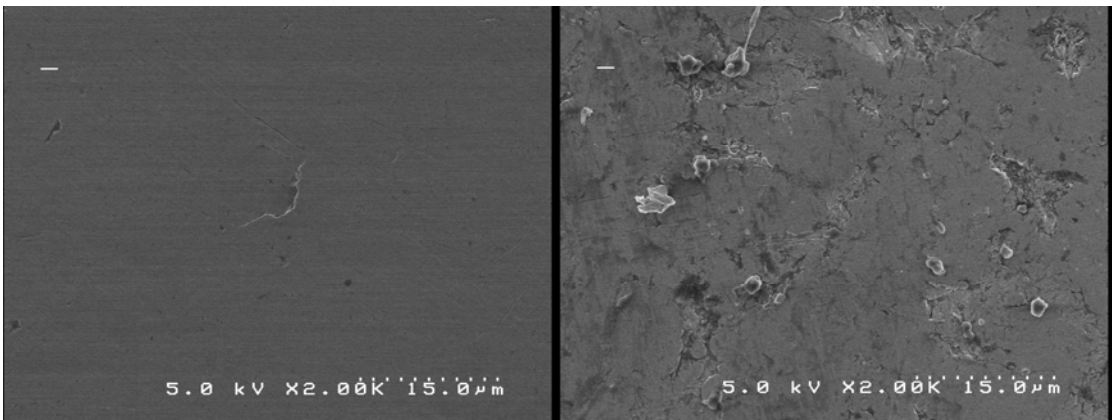
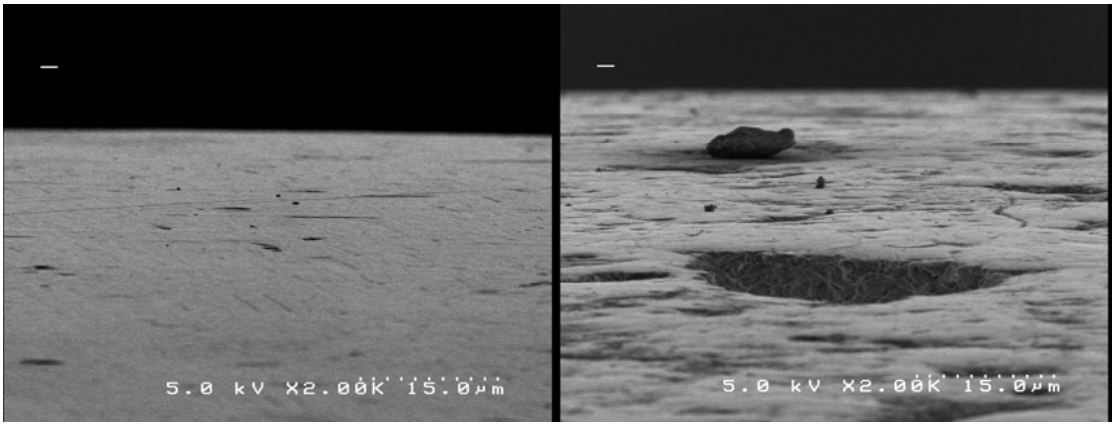
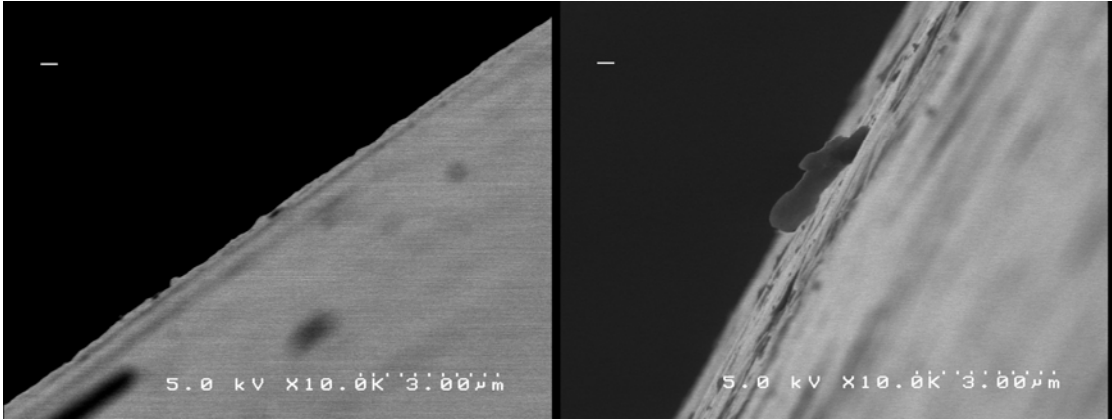


Figure 5.7. (a) Modified fixture plate. (b) Oblique collision in a 0-1 sphere formation. (c) Bottom view of a sphere pair in a 0-3 formation.

5.2.2 Sphere surface properties

Besides Delrin and glass particles, two kinds of steel spheres were used. The steel ball bearings used previously are categorized as *class 1 steel* while *class 2 steel* is used to indicate unpolished steel spheres. The surface roughness of class 2 steel was estimated to be $0.272\mu\text{m}$ based on its SEM surface images. When the two steel surfaces are compared in figure 5.8, the surface of class 2 steel, presented in the right column, contrasts sharply with the smooth steel ball bearing on the left column.



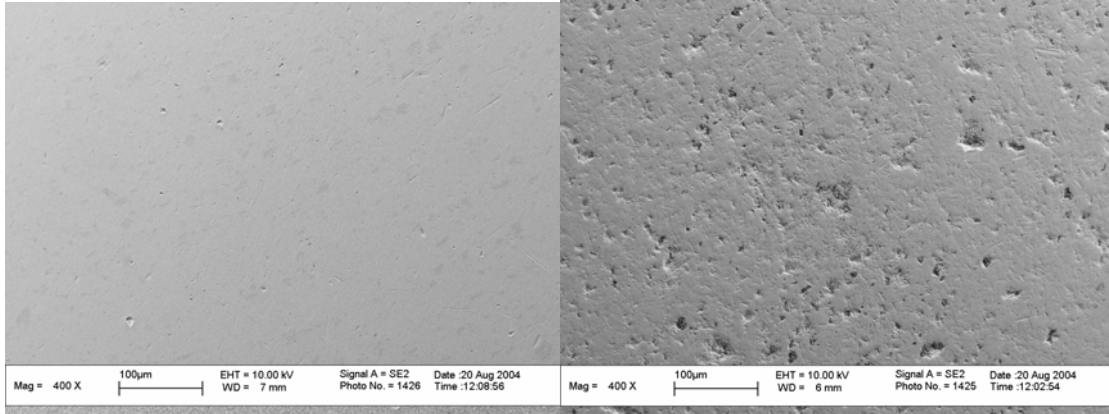


Figure 5.8. SEM images of the two classes of steel particles. The left column presents the results for class 1 steel (ball bearing) and the surfaces of class 2 steel (unpolished sphere) are shown in the right column. Both are of diameter 12.7mm .

5.2.3 Image processing

The motion of each sphere center was tracked in ImageJ as described in section 2.1.3 and indicated with C_1 and C_2 in figure 5.9(a). On each frame, the centroid of the marker was estimated, as denoted by the triangle A or B on each sphere. The arctangent of the slope of line $\overline{AC_1}$ measured the inclination angle α_{i1} of the impact sphere. Line $\overline{BC_2}$ was used to measure α_{i2} for the target sphere. With the time evolution of the inclination angles, a line was fitted over 15 milliseconds before the collision to estimate the corresponding angular velocities. When in contact, the line $\overline{C_1C_2}$ defined the contact normal as shown in figure 5.9(b). Prior to the collision, the impact angle θ_{i1} was defined by the contact normal and the line fitted through 15 position points of the impact sphere. The other angles were estimated similarly. The target sphere remained stationary before collision under most of the investigated impact conditions. Thus the target impact angle θ_{i2} was set to zero. The translational velocities of each sphere were calculated by the distance a sphere travels from the previous frame. The mean value of 15 consecutive frames before

and after collision were calculated for U_{i1} , U_{r1} , U_{i2} , and U_{r2} . A typical result depicting the trajectories of an oblique collision is shown in figure 5.9(c).

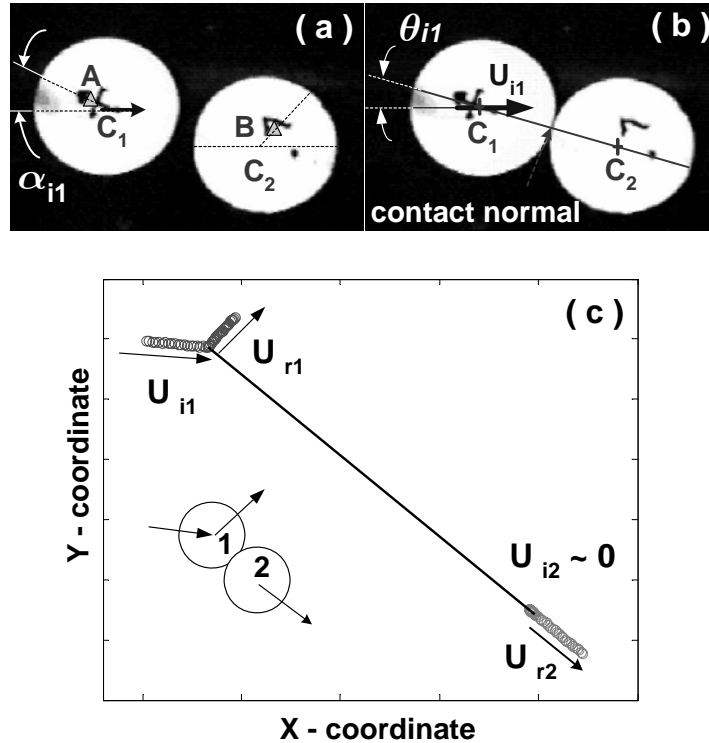


Figure 5.9. Bottom view of an oblique collision between two Delrin spheres in water for (a) the marker centroid and the inclination angle of the impact sphere, (b) the contact normal and the impact angle. (c) Time evolution of the particle trajectory. The sphere velocities are $U_{i1} = 11.94$ cm/s, $U_{i2} \approx 0.95$ cm/s, $U_{r1} = 4.48$ cm/s, and $U_{r2} = 8.24$ cm/s. For this collision, the effective coefficient is $e \approx 0.39$ while $St_B = 22.3$.

5.2.4 Parameters

Analogously to an immersed particle-on-wall oblique collision, an inter-particle oblique collision is decomposed into a normal and a tangential component with respect to the contact normal. The normal and the tangential components motion of the impact sphere

are $U_{in} = U_{i1} \cos \theta_{i1}$ and $U_{it} = U_{i1} \sin \theta_{i1}$ as shown in figure 5.10 and the post-collision velocities are calculated similarly as $U_{r1n} = U_{r1} \cos \theta_{r1}$ and $U_{r1t} = U_{r1} \sin \theta_{r1}$. The target velocities are estimated likewise.

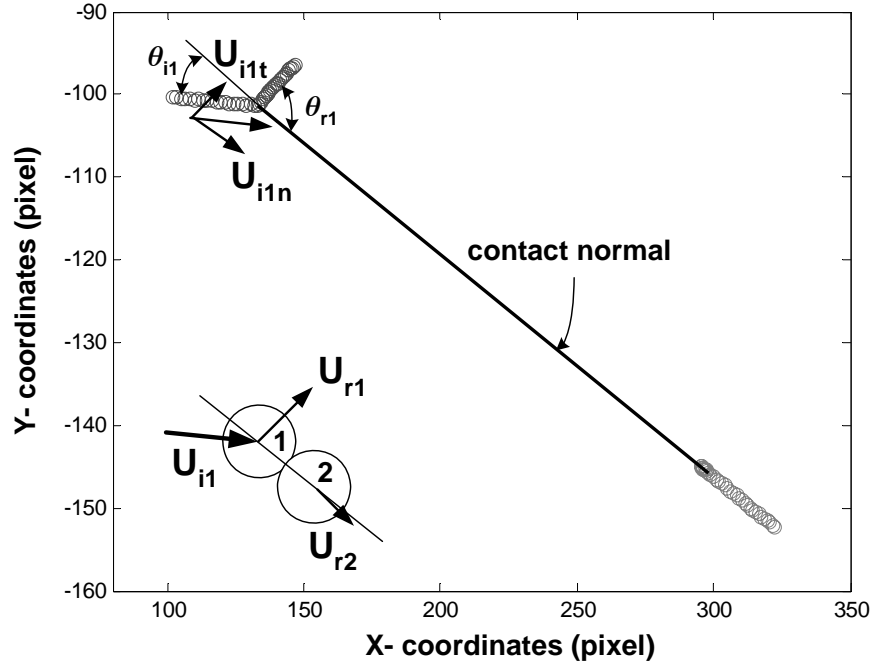


Figure 5.10. Decomposition of the impact motion with respect to the contact normal into a normal and a tangential components as $U_{in} = U_{i1} \cos \theta_{i1}$ and $U_{it} = U_{i1} \sin \theta_{i1}$.

With the decomposed velocity components, the effective normal coefficient of restitution for an immersed inter-particle oblique collision is defined as

$$e_n = -\frac{U_{r1n} - U_{r2n}}{U_{i1n} - U_{i2n}}. \quad (5.5)$$

The correlation between the normal coefficient of restitution, $e_n = -U_m/U_{in}$, and the normal particle Stokes number, $St_n = m_p U_{in} / 6\pi\mu a^2$, for an immersed particle-on-wall

collision suggests the *normal binary Stokes number*:

$$St_n = \frac{m^* (U_{r1n} - U_{r2n})}{6\pi\mu a^{*2}}, \quad (5.6)$$

for inter-particle oblique collision using the relative normal velocity.

5.3 Normal component of motion

In figure 5.11, the effective normal coefficient of restitution, equation (5.5), is plotted against the normal binary Stokes number, equation (5.6), for oblique collisions between identical spheres. A monotonic decrease in e_n is observed with decreasing normal binary Stokes number St_n . Zero restitution is observed at a critical number around $St_n = 6 \sim 8$ where the spheres possess nearly identical normal velocities after collision. The two classes of steel spheres resulted in nearly the same e_n when the collision occurred at $10 < St_n < 30$.

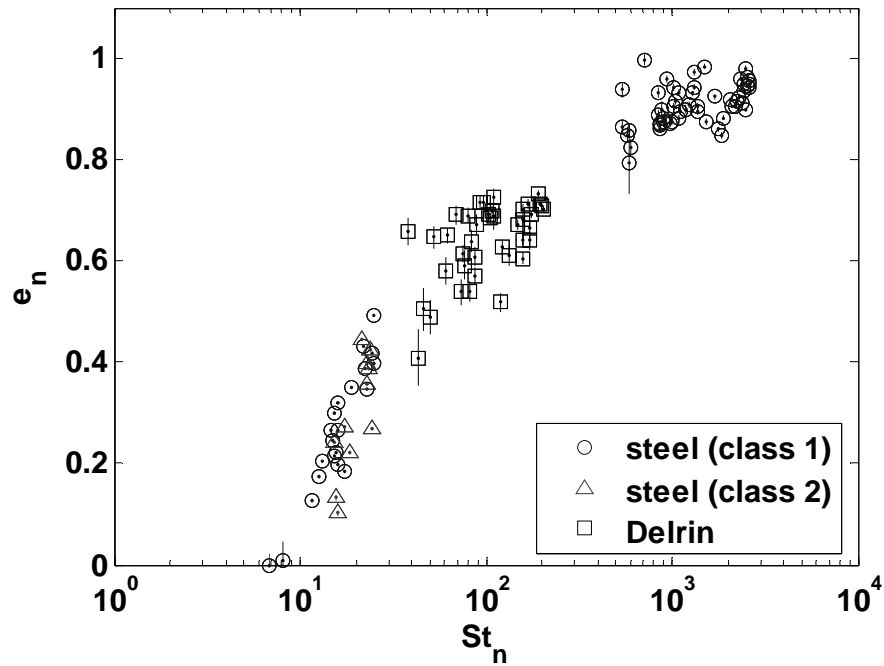


Figure 5.11. Normal coefficient of restitution as a function of normal binary Stokes number for immersed oblique collisions between identical spheres.

In figure 5.12, the current measurements are compared with the data from fully immersed normal collisions, including particle-wall impact and inter-particle collisions between identical or dissimilar pairs of spheres. Since the experiment covered a wide range of impact angle, the general agreement between the oblique and the normal data should validate the assumption that the normal component of motion can be decoupled from the tangential component during an immersed oblique collision, despite the size and the mobility of the target. In other words, the knowledge of the immersed normal inter-particle collision, as developed in the previous chapters, can be used to describe the normal component of motion of an immersed oblique collision in terms of e_n and St_n .

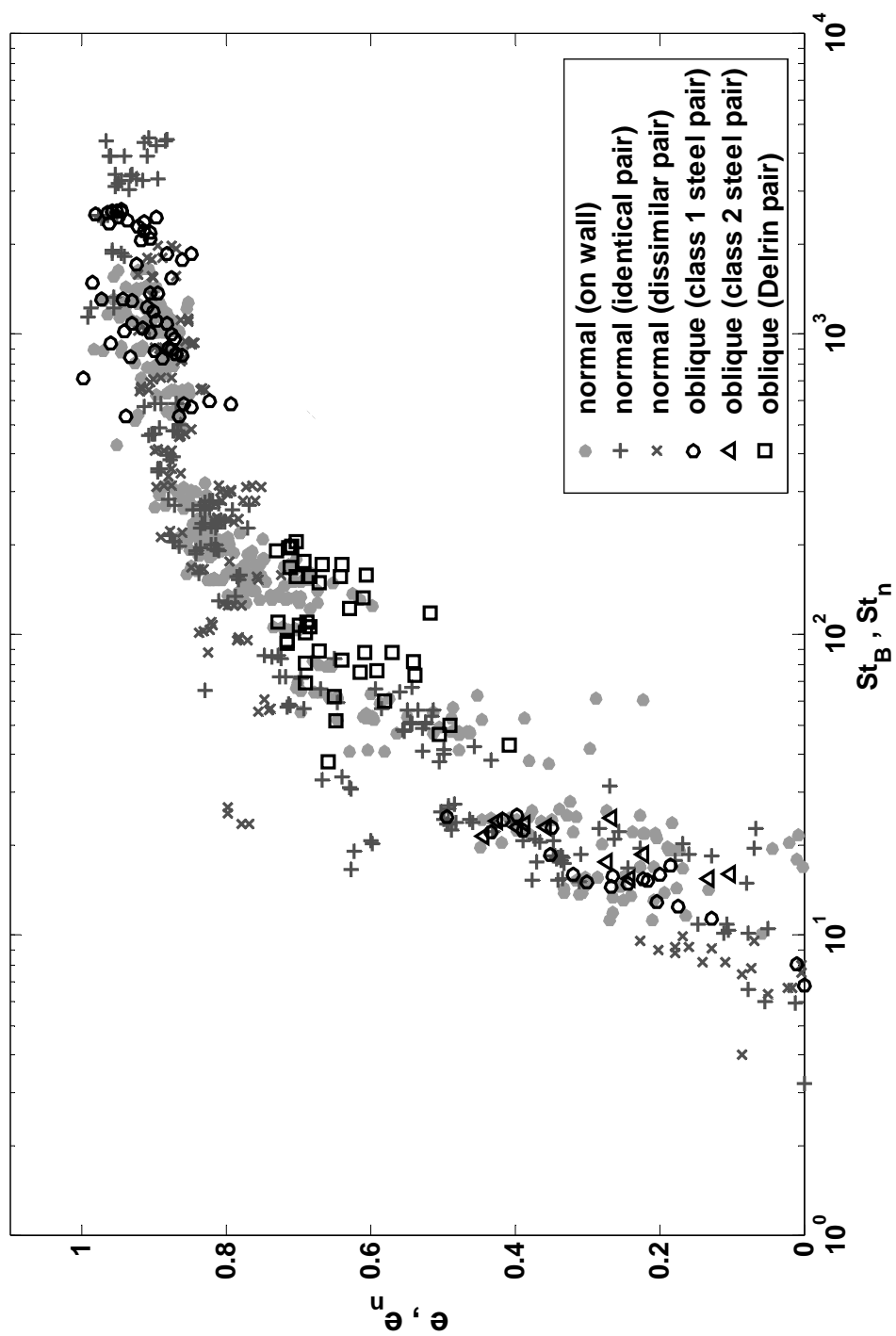


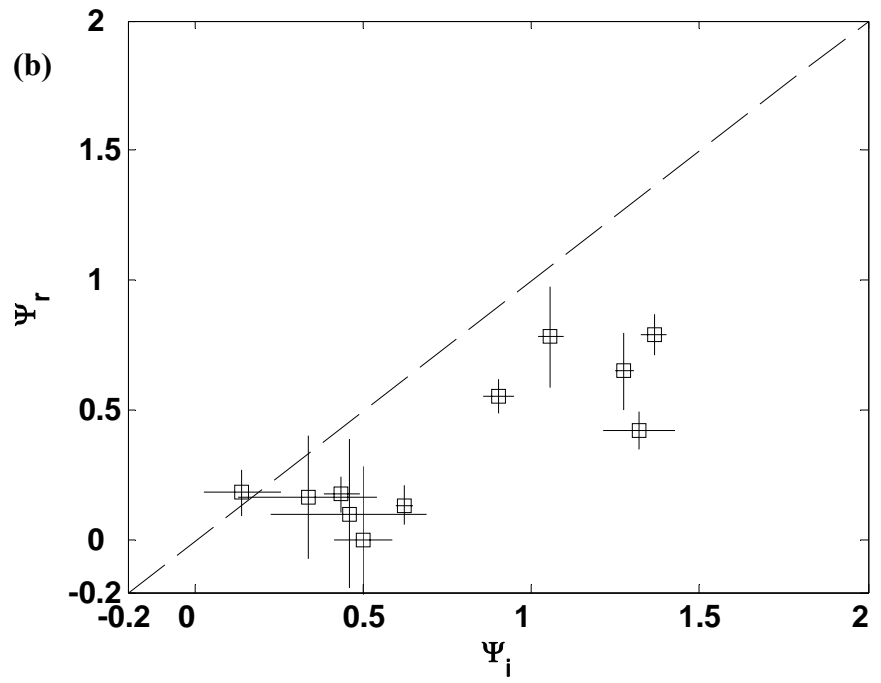
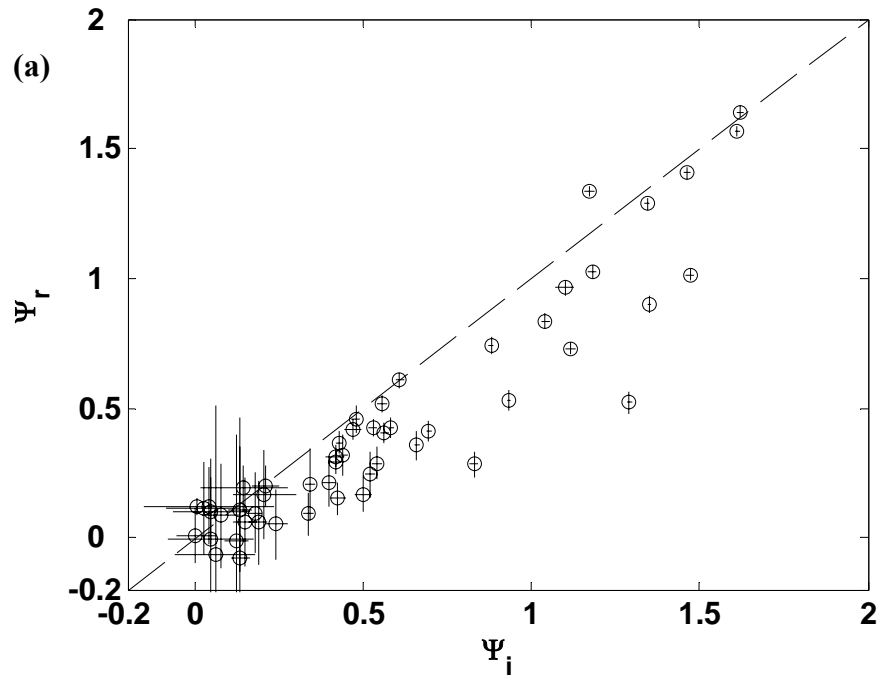
Figure 5.12. The comparison of (e_n, St_B) and (e_n, St_n) between normal and the normal component of oblique collision data.

5.4 Tangential component of motion

The normal component of motion of immersed oblique inter-particle collisions has been shown to follow the behavior of a normal collision, which is in agreement with the experimental findings for particle-wall oblique collisions (Joseph and Hunt 2004; Kantak and Davis 2004). These investigations suggest that the normal component of motion is independent of the tangential surface interaction. In order to completely describe an oblique collision, the tangential component of motion is required. The tangential contact mechanism is first examined at the contact point by comparing the effective angles of incidence and rebound, Ψ_i and Ψ_r , with Maw's collision model followed by the investigation at the sphere center of mass.

5.4.1 Properties at the contact point

With a stationary wall, the impact takes place at nearly the same location ensuring consistent target surface condition. However, the mobility of the target sphere may change the surface orientation and result in contact at different locations yielding more scatter in measuring μ_c between two colliding spheres. Since the effective angles, Ψ_r and Ψ_i , correlate to Maw et al.'s non-dimensional angles by a constant, $2(1-\nu)/\mu_c(2-\nu)$, the dependence of Ψ_r on Ψ_i should reveal the same contact mechanism. Figures 5.13(a)–(c) present the results with respect to the dashed diagonal that indicates a specular reflection for frictionless surfaces.



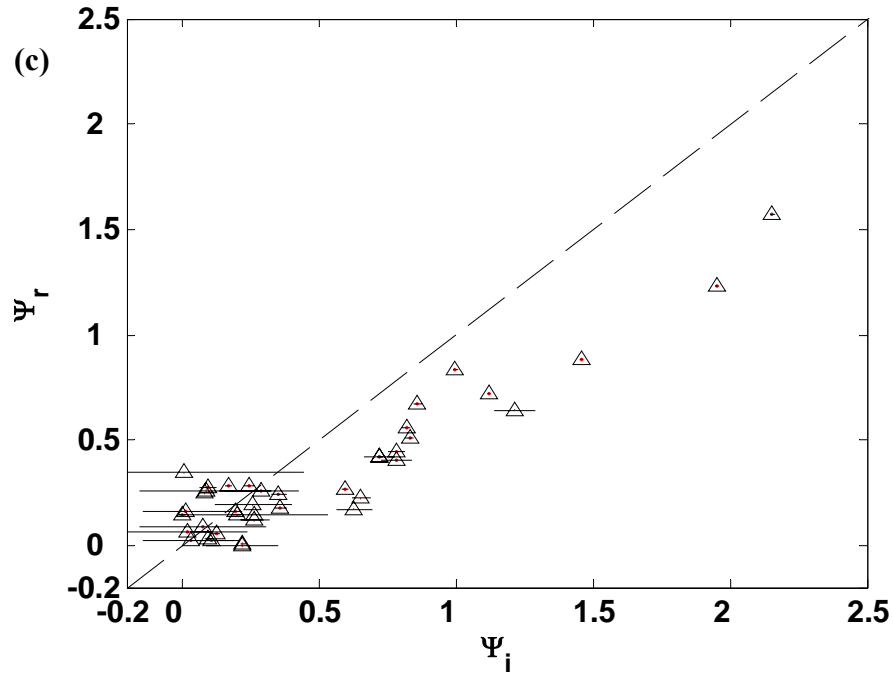


Figure 5.13. Effective angle of reflection as a function of the effective incidence angle for immersed oblique collisions between: (a) steel ball bearings, $\sigma_s \approx 0.02\mu\text{m}$ and $500 < St_n < 2400$; (b) unpolished steel spheres, $\sigma_s \approx 0.2\mu\text{m}$ and $St_n < 25$; (c) Delrin spheres, $\sigma_s \approx 0.1\mu\text{m}$ and $40 < St_n < 200$.

Only the collisions between smooth steel ball bearings result in rebounds close to a specular reflection in figure 5.13(a). The measurements with class 2 steel exhibit a similar rebound to that observed using Delrin particles, as shown in figures 5.13(b) and (c). Both deviate from specular reflection indicating frictional surface contact due to their rough surfaces. When the sphere impacts at $0 < \Psi_i \leq 0.5$, the effective reflection angles reveal a regime that may correspond to an initial sticking at the contact point as observed in regimes I of Maw's model. In particle-wall oblique collisions, a negative reflection angle is clearly observed, as shown in figure 5.5, indicating the reverse tangential motion of the impact particle, a motion of which requires large tangential contact impulse. The mobility of the target sphere and the presence of interstitial liquid reduce both the asperity contact

and the contact duration resulting in weak tangential contact impulse. Thus a negative Ψ_r is rarely seen in an immersed inter-particle collision.

To see more clearly how the surface asperity change the tangential interaction, the reflection angles for the two classes of steel spheres are compared in figure 5.14. By comparing the data at different normal Stokes numbers, more specular reflection with less scatter is observed for collisions at $St_n > 500$ than the ones for $St_n \leq 25$ since the particle has higher inertia to overcome the hydrodynamic forces. When the sphere impacts at $St_n \leq 25$ and $\Psi_i > 1.0$, the rebound between class 2 rough steel spheres deviate further from specular reflection than between a ball bearing pair, which can be attributed to the large surface roughness.

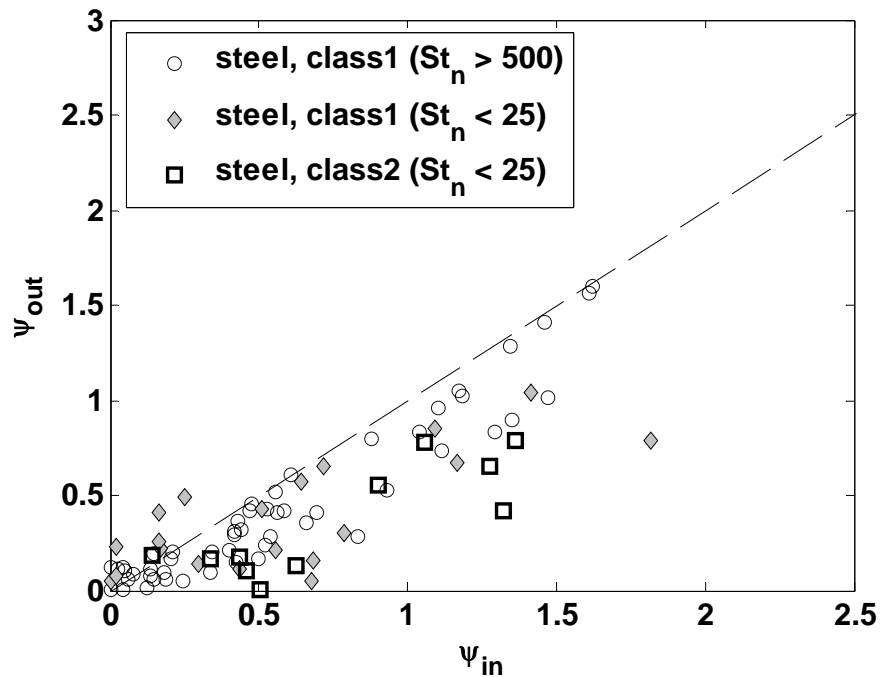


Figure 5.14. Comparison of the effective reflection angle as a function of effective angle of incidence for oblique collisions between different steel spheres at two ranges of normal Stokes numbers.

5.4.2 Properties at the sphere centers of mass

(a) Rebound angle

Since the tangential contact is short for an inter-particle collision, the particle angular velocities remain nearly zero through the collision process with the current experimental setup. Thus the rebound motion at the sphere centers of mass should capture the principal dynamics. The impact and rebound angles, θ_{i1} , θ_{r1} , θ_{i2} , and θ_{r2} , were measured at the sphere center of mass with respect to the contact normal for both particles. Recall that $\theta_{i2} \approx 0$ for most of the current impact conditions. Figure 5.15 presents the rebound angle of the impact sphere. For collisions between two ball bearings at $St_n > 500$, the rebound angle changes abruptly when the impact angle drops below 10 degrees. However, if the smooth ball bearings collide at $St_n < 25$, a smooth transition is observed. Due to the lack of particle inertia, their relative motion in the tangential direction may be synchronized by the action of the interstitial viscous liquid. As for collisions of class 2 steel or Delrin pair of particles, the rebound angle also changes continuously with decreasing impact angle. The smooth trend can be explained by physical asperity interaction in the tangential direction.

The rebound angle of the target sphere is also plotted against the impact angle, θ_{i1} , in figure 5.16. Though the data scatter more than the rebound of the impact sphere, the target rebound angle, θ_{r2} , decreases with diminishing θ_{i1} . The nearly zero rebound angles for steel collisions at $St_n < 25$ can be attributed to weak tangential impulse. For the collisions between the ball bearings at higher normal Stokes number, non-zero rebound angle is observed with less scatter, due to the larger particle inertia and the smoother surface property. The intermittent asperity interaction may be the reason for the larger scatter of Delrin data than the other particle pairs.

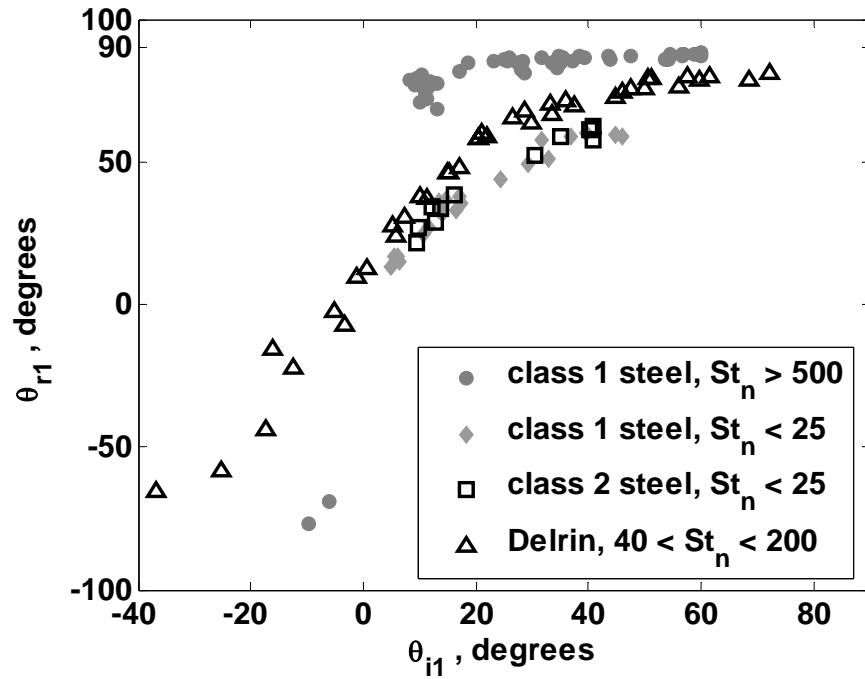


Figure 5.15. Rebound angle of the impact sphere as a function of the impact angle at the sphere centers of mass.

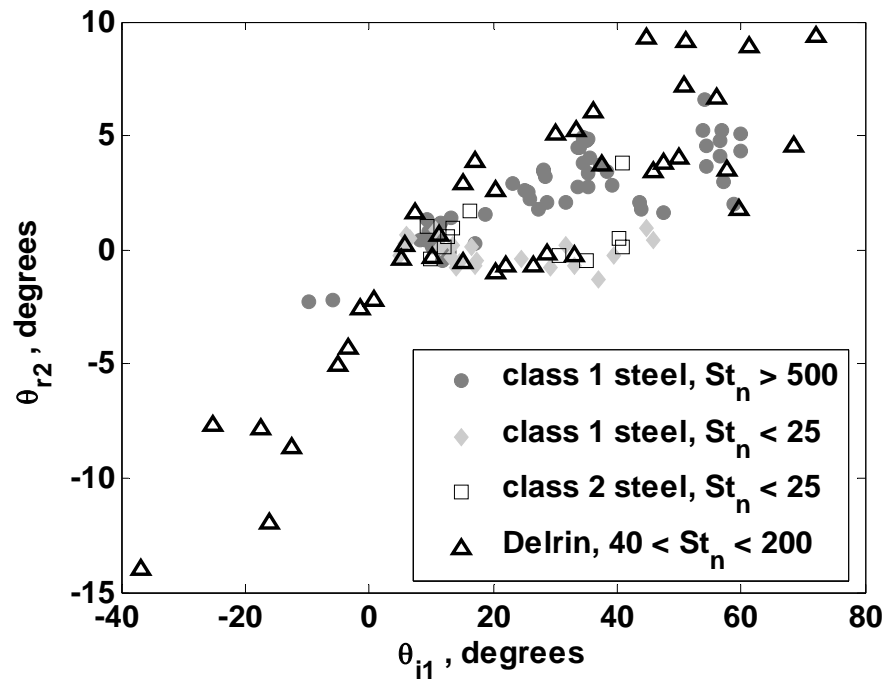


Figure 5.16. Rebound angle of the target sphere as a function of the impact angle at the sphere centers of mass. This is a complementary result to figure 5.15.

If two dry colliding surfaces are perfectly smooth, their post-collision trajectories will form a 90-degree angle. When an oblique collision occurs in liquid, the interstitial fluid layer affects the tangential surface interaction resulting in a smaller angle. An *effective rebound angle* can be defined

$$\Pi_{rbd} = \frac{|\theta_{r2} - \theta_{r1}|}{\pi/2}, \quad (5.7)$$

as the ratio of the measured included angle, $|\theta_{r2} - \theta_{r1}|$, to the dry frictionless rebound angle, $\pi/2$. A small value should indicate strong hydrodynamic forces that dissipate the total tangential momentum in the solid phase. To characterize the fluid effects, the tangential binary Stokes number, St_t , is used instead of the normal component. The St_t measures the particle tangential inertia with respect to the shearing hydrodynamic forces and can be calculated as

$$St_t = \frac{m^* |U_{i1t} - U_{i2t}|}{6\pi\mu a^{*2}}, \quad (5.8)$$

using the relative tangential velocity at the sphere centers. The result is plotted in figure 5.17 where a nearly 90-degree angle, indicated by unity $\Pi_{rbd} = 1$, is observed at high St_t . With large tangential Stokes number, the fluid is negligible and the effects of asperity contact are also minor to the rebound motion. The measurements with Delrin particles show larger scatter due to greater asperity height and a greater number density across the surface (Joseph and Hunt 2004).

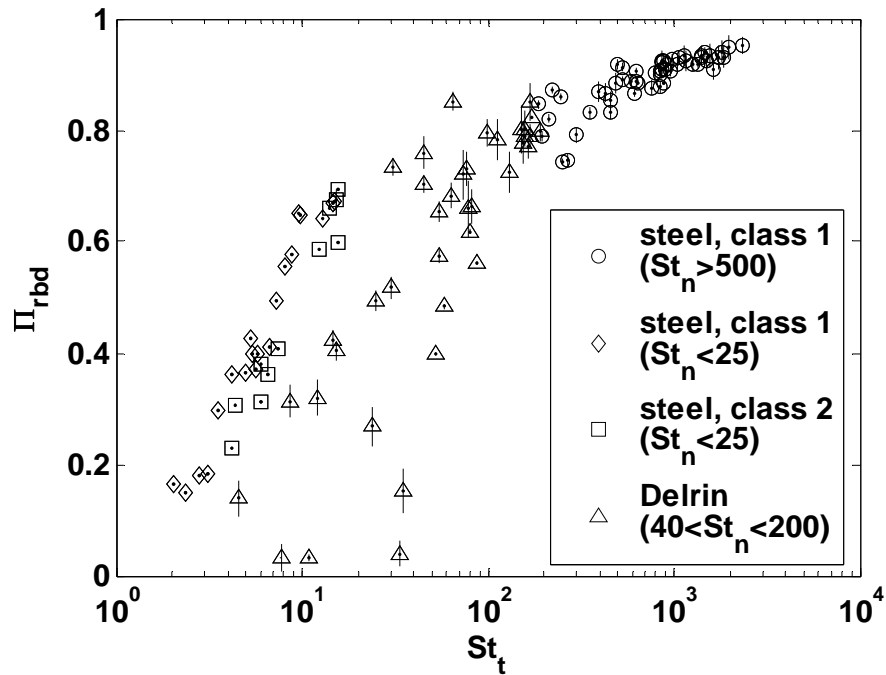


Figure 5.17. Effective rebound angle as a function of the tangential Stokes number. Unity Π_{rbd} indicates a 90-degree angle between the rebound trajectories.

The effective rebound angle is also plotted with the impact angle in figure 5.18. Impacts at higher Stokes number result in rebounds closer to $\Pi_{rbd} = 1$, indicating negligible hydrodynamic effects. The deviation becomes large when the impact angle decreases. At lower impact angle, the surface asperity interacts more thoroughly due to greater normal compression impulse. The weaker shearing motion also diminishes the lubrication of the interstitial liquid. Thus, oblique collision at smaller impact angle and lower particle inertia would undergo more frictional surface interaction resulting in rebound trajectories that deviate further from 90 degrees.

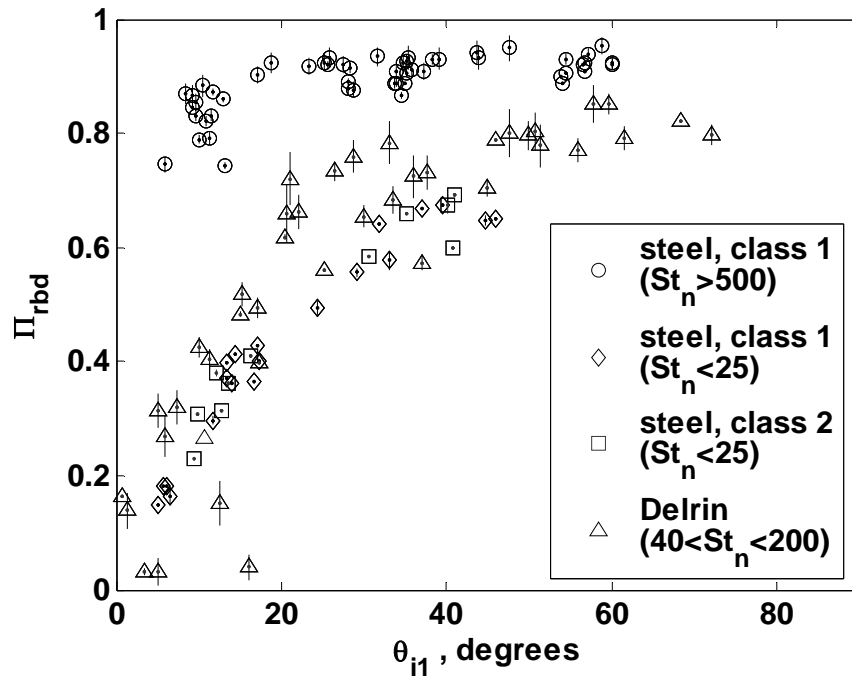


Figure 5.18. Effective rebound angle as a function of impact angle.

(b) Rebound velocity

To further examine the tangential contact mechanisms, the experimentally measured rebound velocities are compared to the predictions from *GS1* and *GS2* collision models using equations (5.3a)–(5.3f) and equations (5.4a)–(5.4d). Recall that *GS1* model involves initial sticking in the tangential surface interaction while *GS2* considers initial sliding. Since both models require the normal coefficient of restitution, the measured e_n are used. The rebound angle of the impact sphere is first examined as a comparison to the observation in figure 5.15. The measured e_n is averaged over the corresponding data in certain ranges of St_n as a function of impact angle θ_{i1} .

For an immersed oblique collision between steel ball bearings at $500 < St_n < 2400$, the averaged normal coefficient of restitution is $\bar{e}_n = -0.0017\theta_{i1} + 0.96$. To examine *GS2*,

the friction coefficient measured by Joseph and Hunt (2004) is supplemented in addition to \bar{e}_n . The prediction from *GS1* model is compared with the actual measurements in figure 5.19 while *GS2* is applied with \bar{e}_n and $\mu_c = 0.02$, as well as \bar{e}_n and $\mu_{dry} = 0.11$. A general agreement is found between the actual rebound angle and the predictions from $e_n - GS1$ and $e_n - \mu_c - GS2$ models. Both models capture the drop of θ_{r1} when $\theta_{i1} < 20^\circ$. This supports the hypothesis that the tangential motion during an immersed oblique collision can be described by an existing collision model, as long as the model parameters, e_n and μ_c , are estimated with the hydrodynamic effects. Using μ_{dry} in *GS2* results in a smaller rebound angle due to overestimated surface friction indicating the significance of lubricating effects especially when θ_{i1} drops below 30 degrees.

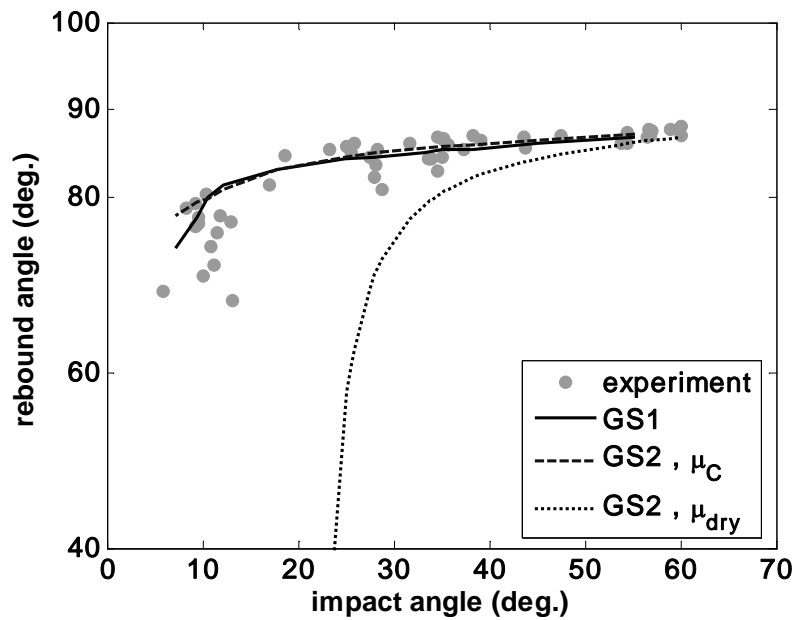


Figure 5.19. Rebound angle at impact steel ball bearing center as a function of impact angle when $500 < St_n < 2400$.

If the ball bearing collides at $St_n < 25$, the averaged effective normal coefficient of restitution is $\bar{e}_n = -0.0076\theta_{i1} + 0.41$. The discrepancy between the experimental data measurements and the predictions using dry model constants is more pronounced. A

high e_{dry} requires sufficient elastic surface deformation for large restitution impulse, which seldom occurs for impact with small particle inertia. The interstitial liquid lubricates the surfaces diminishing the physical contact further decreasing the surface deformation. Using μ_{dry} in *GS2* again overestimates the surface interaction and results in a rebound angle smaller than the actual findings, as shown in figure 5.20. When compared with the nearly constant θ_{r1} in figure 5.19, the rebound angle decreases with decreasing θ_{i1} for collisions at $St_n < 25$. At small impact angle, the slow tangential component of motion is further decelerated by the shearing lubrication force. The interstitial liquid motion may further synchronize the surface motion due to the lack of particle inertia, which explains the smooth decline.

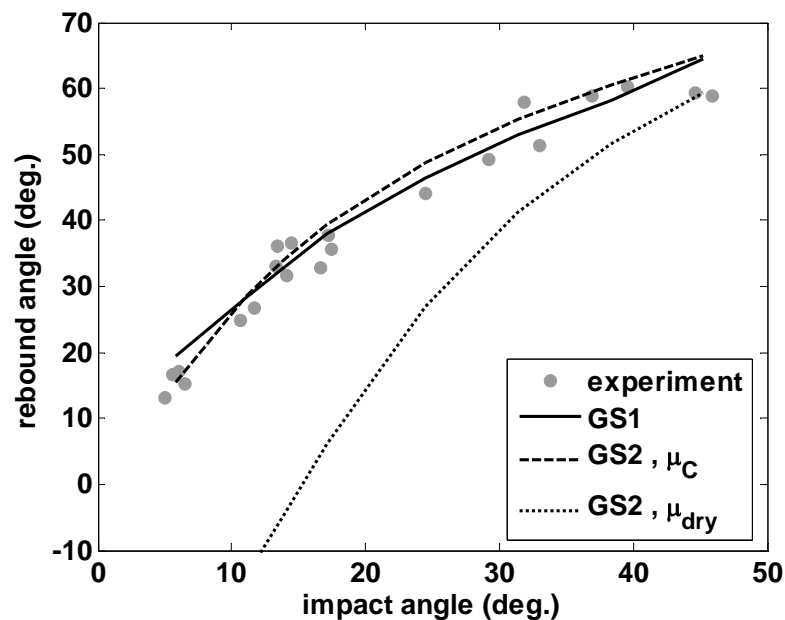


Figure 5.20. Rebound angle at impact steel ball bearing center as a function of impact angle when $St_n < 25$.

The significance of a pertinent friction coefficient is demonstrated when the rebound angle of a Delrin impact sphere is investigated in figure 5.21. For collisions between $40 < St_n < 200$ and $\theta_{i1} < 50^\circ$, the averaged normal coefficient of restitution is

$\bar{e}_n = -0.0011\theta_{i1} + 0.68$ while $\bar{e}_n = -0.0066\theta_{i1} + 0.96$ if $\theta_{i1} \geq 50^\circ$. The factory specification of the dynamic friction coefficient for Acetal Homopolymer (Delrin), $\mu_{dry} = 0.2$, is adopted and the value, $\mu_C = 0.1$, measured for a pair of lubricated Nylon rollers is used. As the previous two cases, both $e_n - GS1$ and $e_n - \mu_C - GS2$ collision models capture the experimental findings but using μ_{dry} in $GS2$ results in erroneous prediction including a reverse motion that seldom occurs in an immersed inter-particle collision. Similar to the collision between steel ball bearing collisions at $St_n < 25$, the diminishing particle inertia explains the decrease of θ_{r1} with decreasing θ_{i1} . A slightly higher rebound angle is observed when comparing figure 5.21 to figure 5.20, which can be attributed to both higher particle inertia and more asperity interaction in the tangential direction for a rougher Delrin surface.

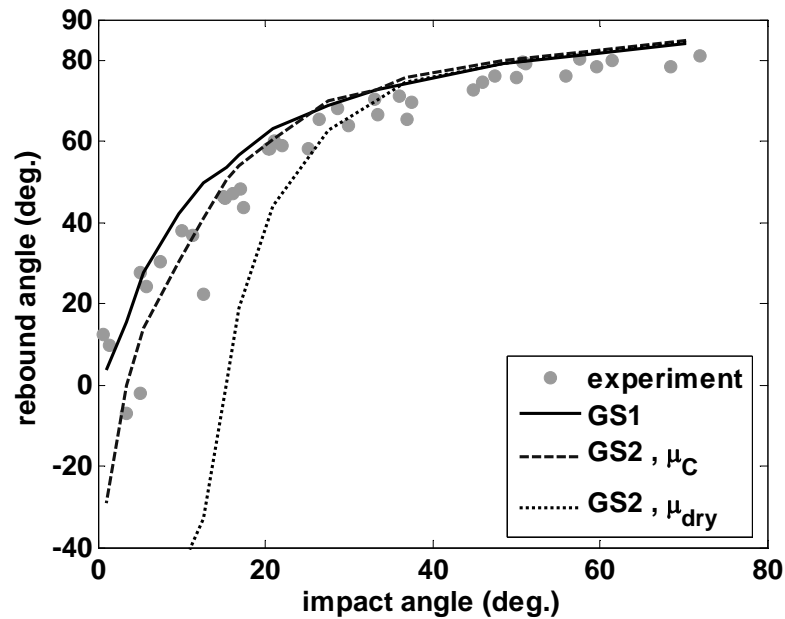


Figure 5.21. Rebound angle at the impact Delrin sphere center as a function of impact angle when $40 < St_n < 200$.

The prediction of the target rebound angle is examined in figure 5.22. Unlike the success in estimating θ_{r1} , the predicted θ_{r2} seldom agrees with the experimental measurements

except at small θ_{i1} . The discrepancy may be attributed to the pre-collision target motion that contradicts the stationary condition assumed in the model. It is also noted that the target rebound angle never exceeds 10 degrees, which is a consequence of weak tangential impulse due to the mobility of the target sphere and the lubricating interstitial liquid.

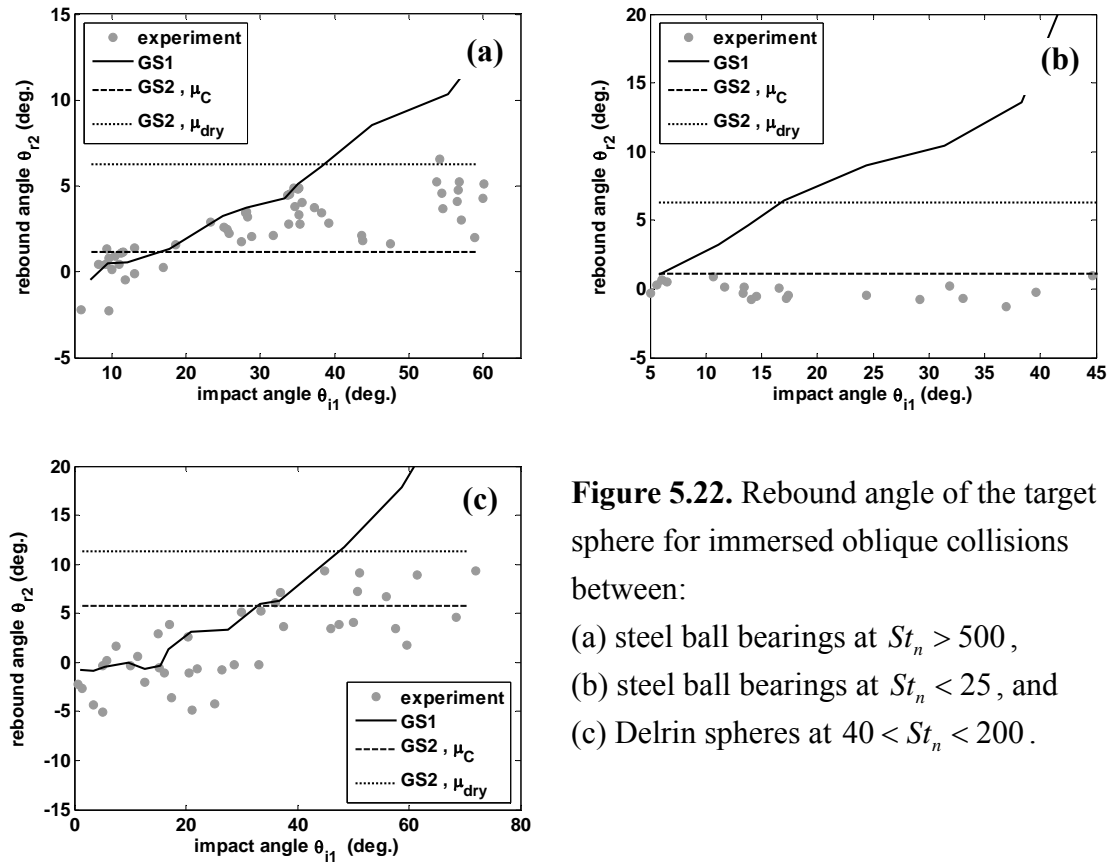


Figure 5.22. Rebound angle of the target sphere for immersed oblique collisions between:

- (a) steel ball bearings at $St_n > 500$,
- (b) steel ball bearings at $St_n < 25$, and
- (c) Delrin spheres at $40 < St_n < 200$.

The collision models are further examined in figure 5.23 where the predicted tangential rebound velocity of the impact sphere is compared with the experimental data. The diagonal solid line plots $y = x$. Both models have comparably good prediction for collisions at $St_n < 500$ but GS1 outperforms GS2 for collisions at high St_n .

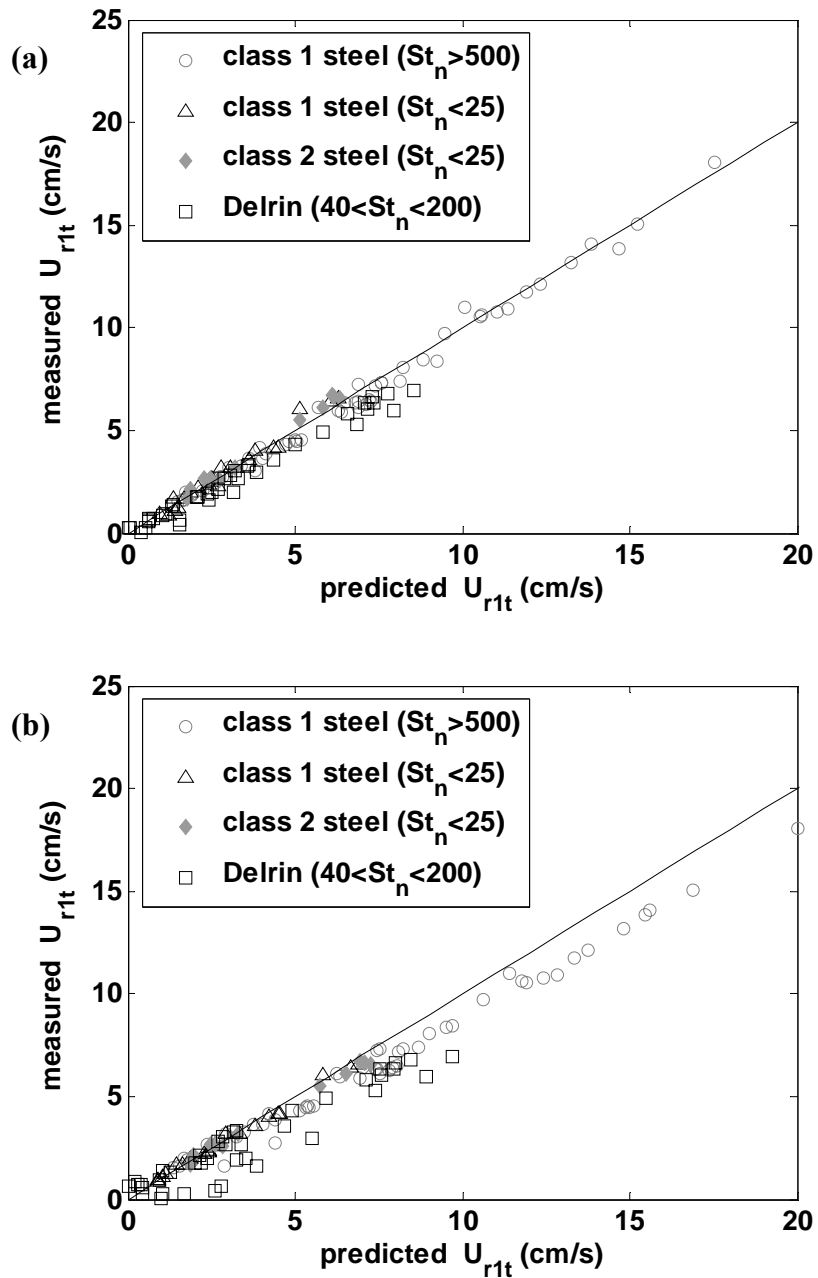


Figure 5.23. Comparison of the predicted post-collision velocity of the impact sphere using (a) $GS1$ and (b) $GS2$ ($\mu_c = 0.02$).

The value $\mu_c = 0.02$ was measured between a steel ball bearing and a Zerodur wall, a target of which has a smoother surface, $\sigma_s = 0.016\mu\text{m}$, than the current ball bearing target. If a friction coefficient is chosen higher than $\mu_c = 0.1$, a more realistic prediction from

GS2 is observed in figure 5.24 illustrating again the importance of a proper model constant. Having model constants modified for the hydrodynamic effects, the two models provide comparable predictions to the actual measurements. Though different tangential surface interactions are considered in the two models, their predictions collapse due to the short contact duration and the lubricating interstitial liquid, whose effects are included in the effective model constants. However, the measurement of μ_C for a rapid collision process is usually difficult and prone to errors, especially with an unconstrained target. Hence the e_n -GS1 model is proposed to be a more practical model than the $e_n - \mu_C$ -GS2 collision model that requires an accurate μ_C .

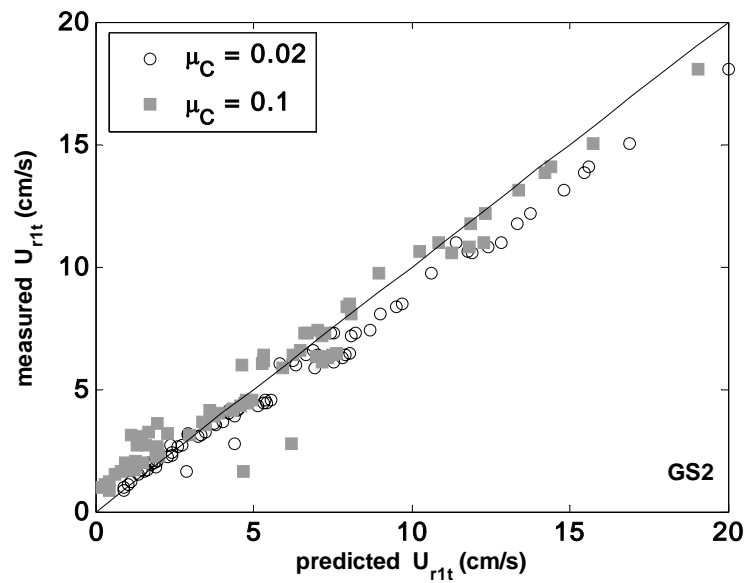


Figure 5.24. GS2 prediction with a higher lubricated friction coefficient.

The model performance on predicting the tangential target rebound velocity is examined in figure 5.25. The weak tangential impulse yields a slow target motion that scatters more than the impact sphere rebound motion. The asperity contact for Delrin particles and the high particle inertia of steel ball bearing may result in rebound faster than the model prediction, which corresponds to the data above the solid line.

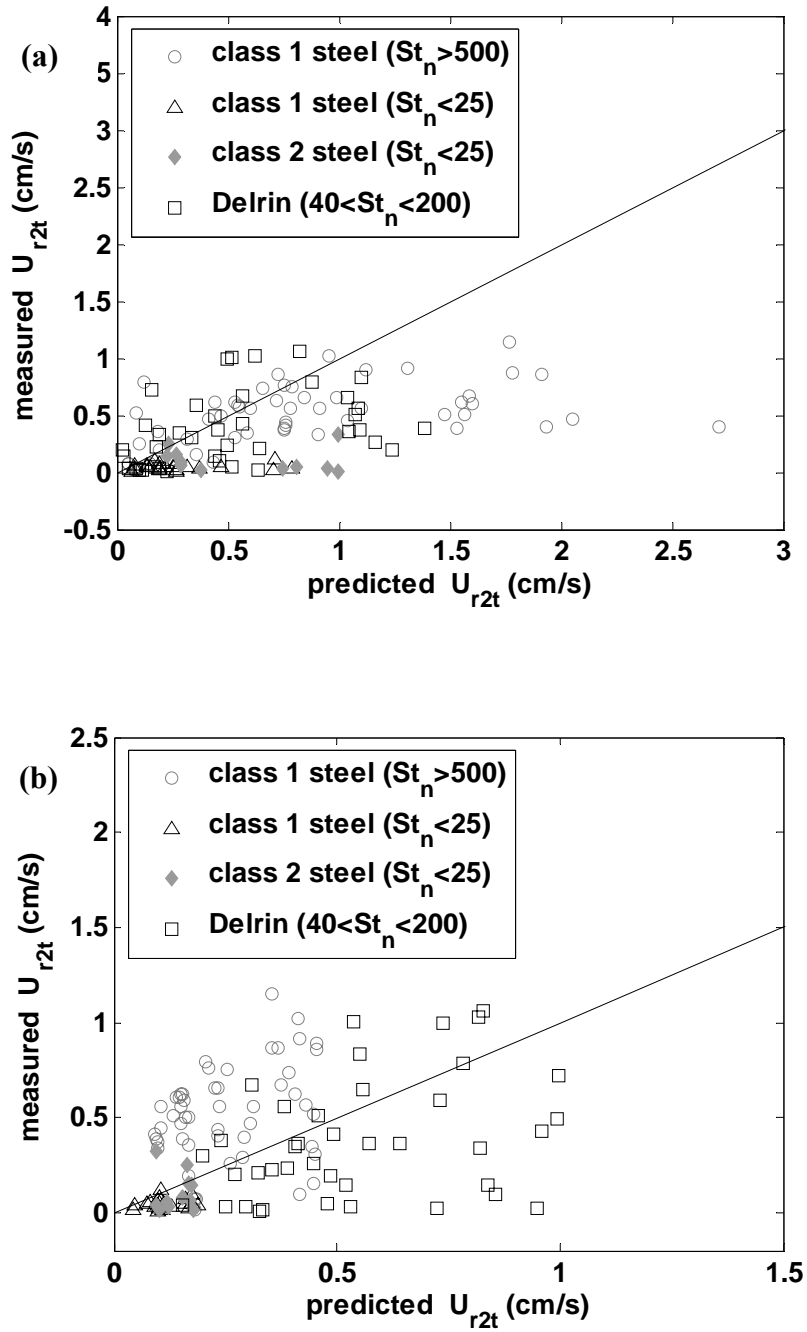


Figure 5.25. Comparison of the predicted tangential rebound velocity of the target sphere using (a) *GS1* and (b) *GS2* ($\mu_c = 0.02$) collision models.

5.5 Conclusion

Fully immersed inter-particle oblique collisions were investigated between identical spheres, including smooth steel ball bearings, unpolished steel spheres, and Delrin spheres. The collision was decomposed into a normal and a tangential component with respect to the contact normal defined by the line of centers when the spheres are in contact. The relevant parameters for an immersed normal collision, namely the effective coefficient of restitution and the binary Stokes number, were modified using the normal component of the sphere velocity. The correlation between the modified parameters, e_n and St_n , exhibits the same trend as a head-on normal collision. Thus, the model that has been developed in chapters 3 and 4 can be used to describe the normal component of motion of an oblique collision.

The tangential component of motion was examined in greater detail. In general, the tangential motion can be captured by the existing collision models as long as the model parameters, such as the effective friction coefficient and the normal coefficient of restitution, are properly modified for the hydrodynamic effects. The effective friction coefficient is sensitive to both the impact conditions and the surface properties. For the current impact conditions, the measurement of an effective friction coefficient is usually noisy due to the mobility of the target sphere and the difficulty in tracking the nearly zero sphere rotation. Thus Goldsmith's second contact model that requires an accurate effective friction coefficient is of less practical value. Fortunately, the prediction with Goldsmith's first model, requiring only the effective normal coefficient of restitution, in general agrees with the experimental data. The $e_n - GS1$ collision model is proposed to be the relevant tangential contact model that can be integrated with the proposed collision model for the normal component of motion. The mobility of the target sphere dramatically changes the rebound motion of the target sphere that requires further

investigations.

The tangential motion at the contact point was also compared to Maw's theory that describes the dry surface tangential interaction. Because of the interstitial lubricating layer and the mobility of the target, pure sticking contact was rarely observed in the current experiments. With higher effective incidence angle, a sliding mechanism better describes the experimental findings and collisions at smaller angle may be captured by a sticking-then-sliding process.

Chapter 6

Wall Influence Distance

In chapter 4, the approach of an immersed pendulum predicted by the collision model was compared with various experimental measurements, and the good agreement obtained validated the model. In the comparisons, only the total hydrodynamic forces, rather than the individual components, were examined. For unsteady particle motion, real-time measurement of the fluid force is a challenging task and precise force decomposition is nearly impossible. The validated flow model can thus be used to investigate the detailed hydrodynamic forces, circumventing the experimental difficulties. In the first section of this chapter, the importance of each hydrodynamic force is examined at different impact conditions. Subsequently, a length scale should be defined to characterize the spatial interaction between the sphere and the wall due to the coupling of the surface motion with the interstitial liquid flow. This length scale can be used to indicate the distance to which the sphere's motion can be described with the conventional fluid forces without any wall modification.

6.1 Examination of the three hydrodynamic forces

The flow model that describes the circumferential motion of a pendulum, ds/dt , during its approach to a wall is:

$$\begin{cases} \frac{ds}{dt} = U \\ m_p \frac{dU}{dt} = F_G - F_D(\text{Re}, \delta^*) - F_{AM}(\delta^*) - F_H(\text{Re}, \delta^*). \end{cases} \quad (6.1)$$

Three hydrodynamic forces are included-the steady viscous drag, $F_D(\text{Re}, \delta^*)$, the added mass force, $F_{AM}(\delta^*)$, and the history force, $F_H(\text{Re}, \delta^*)$. For each hydrodynamic force, the dependence on the non-dimensional gap, $\delta^* = \delta/a$, indicates a wall modification factor and the correction for the higher Reynolds number effects resides in the dependence on Re . It has been concluded that the prediction using the full flow model generally agrees with the experimental measurements. An additional set of simulations was conducted in which different hydrodynamic forces were set to zero. The resultant velocity profile was compared with the actual measurements to examine the importance of each fluid force. Through out this chapter, the forces are presented in their magnitudes.

First, the motion of a sphere of density $\rho_p = 2.54\rho_f$, impacting at particle Stokes number of $St = 214$, is simulated. As before, the particle motion predicted from the full flow model agrees with the experimental results, as indicated by the matching solid line and the open circles in figure 6.1. However, if either of both of the history and the added mass forces were excluded from equation (6.1), the velocity is overestimated. The neglecting of the history force results in a prediction that deviates further from the actual measurements than the exclusion of the added mass force.

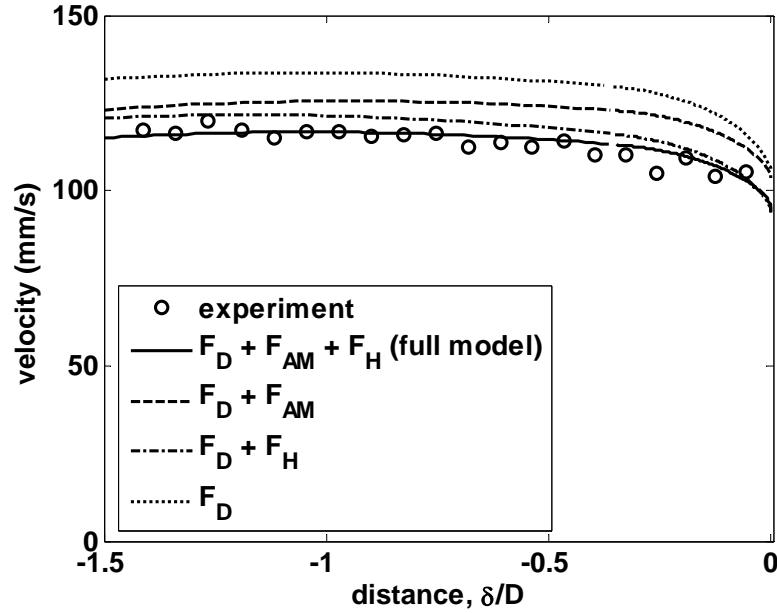


Figure 6.1. Comparison of the predicted pendulum motion using the full or the partial flow model with $\rho_p/\rho_f = 2.55$, at $St = 214$.

A second comparison is made with $\rho_p = 2.0 \rho_f$ as a glass sphere in a water-glycerol mixture. For an impact at a lower particle Stokes number of $St = 50$, the result from the full flow model compares well with the experimental profile, as shown in figure 6.2. Without the history force, the velocity is overestimated. However, the exclusion of the added mass force results in an underestimation, suggesting a force, $F_{AM}(t, \delta^*)$, that assists the sphere motion towards the wall. This phenomenon can be explained by the competition between the two terms in the wall-modified added mass force, as given in equation (3.7). This expression is reproduced below:

$$F_{AM}(t, \delta^*) = -\frac{1}{2} m_f \left[1 + 3W(\delta^*) \right] \frac{dU}{dt} - \frac{3}{4} m_f U^2 \frac{dW(\delta^*)}{d\delta^*}. \quad (6.2)$$

Since the wall correction term $W(\delta^*)$ remains a positive value for all δ^* and its derivative is always negative and the second term in equation (6.2) may exceed the first

tem, resulting in a positive force that assists the pendulum motion towards the wall. When compared with the result in figure 6.1, for an immersed pendulum motion at a smaller particle Stokes number, the hydrodynamic forces decelerate the particle motion more easily resulting in faster decaying particle acceleration, dU/dt , which yields a positive $F_{AM}(t, \delta^*)$ more likely.

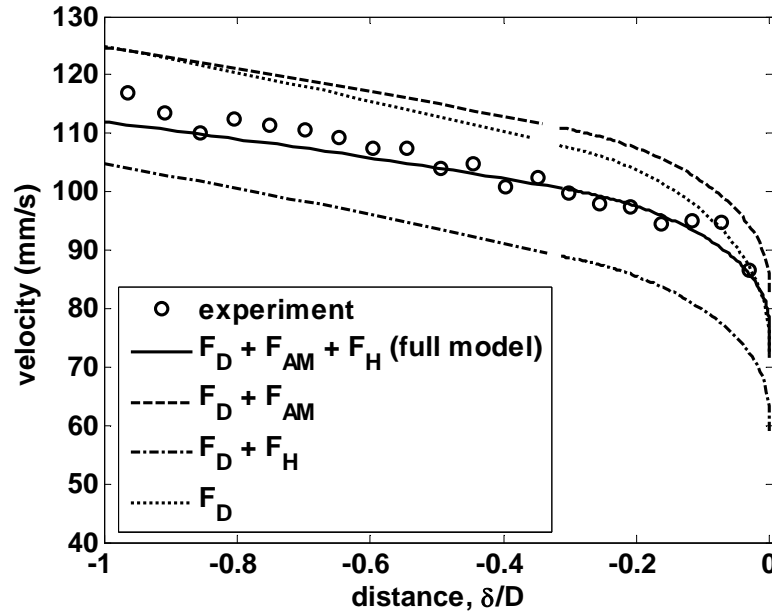


Figure 6.2. The influence of each hydrodynamic force in determining the motion of a solid sphere of, $\rho_p/\rho_f = 2.0$, that approaches the wall at $St = 50$.

Figure 6.3 shows the simulation results for a pendulum motion at $St = 60$, similar to the case examined in figure 6.2, but at a higher solid-to-liquid density ratio of $\rho_p/\rho_f = 6.83$. In addition to the observation that an incomplete flow model, especially without $F_H(t, \delta^*)$, predicts an erroneous profile, the wall-modified added mass force becomes less important in assisting the pendulum motion towards the wall due to a higher solid-to-liquid density ratio. Also noted is the sudden deceleration of the particle when it moves to a distance of about $0.3D$. The abrupt change is not observed for the lighter sphere in figure 6.2, which decelerates steadily throughout the observed particle motion. In contrast,

the particle motion in figure 6.1, which impacts at a higher St , exhibits no significant deceleration until $0.1D$.

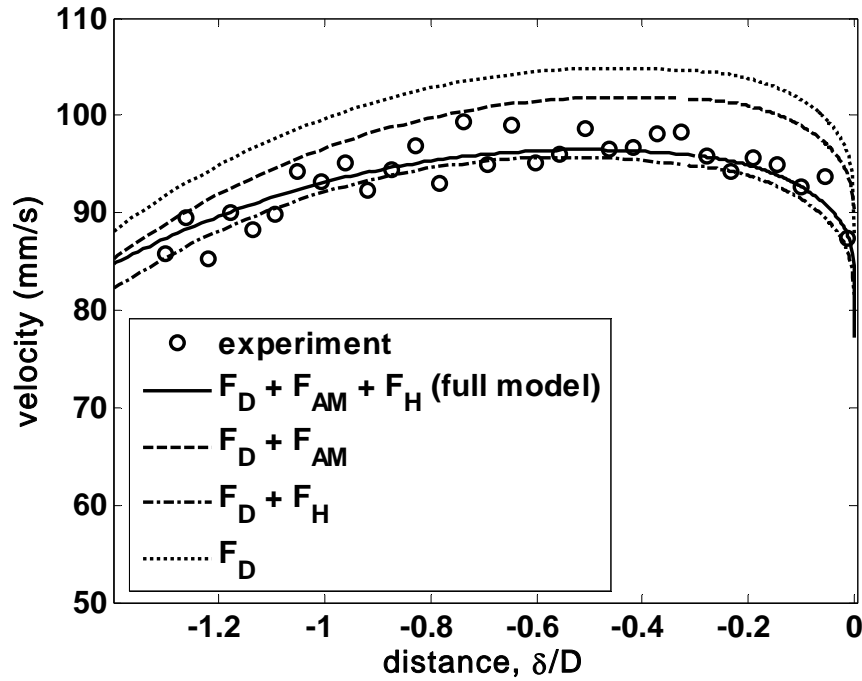
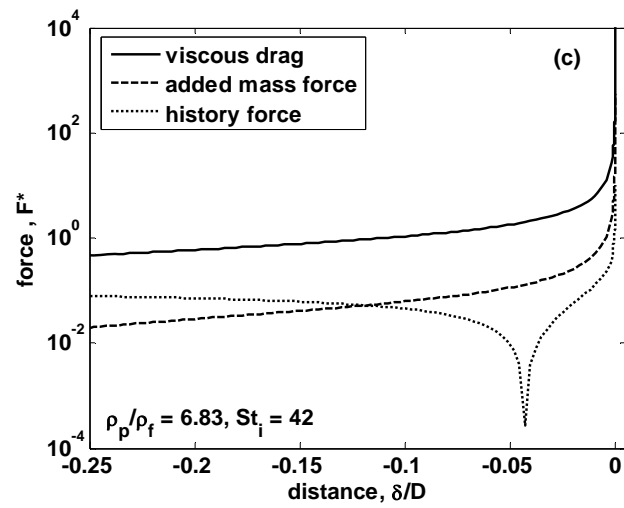
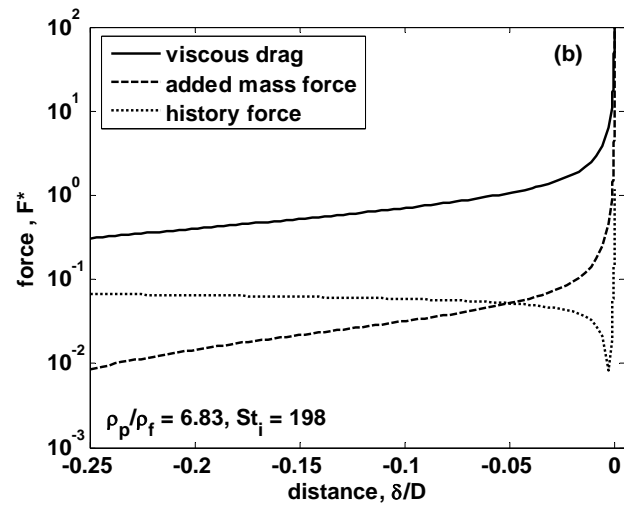
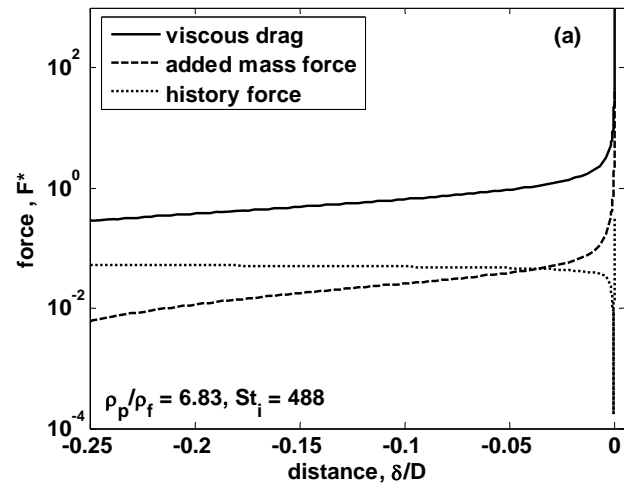


Figure 6.3. The influence of each hydrodynamic force on the approach of a dense solid sphere of $\rho_p/\rho_f = 6.83$, that impacts at $St = 68$.

To examine the effects of the three fluid forces on the particle motion, their evolution as a function of the scaled gap, $\delta^* = \delta/D$, is compared at different impact Stokes numbers in figures 6.4(a)–(d). In these simulations, the sphere diameter, the solid-to-liquid density ratio, and the pendulum release angle are kept the same. Only the liquid viscosity is being increased to achieve a lower impact Stokes number.



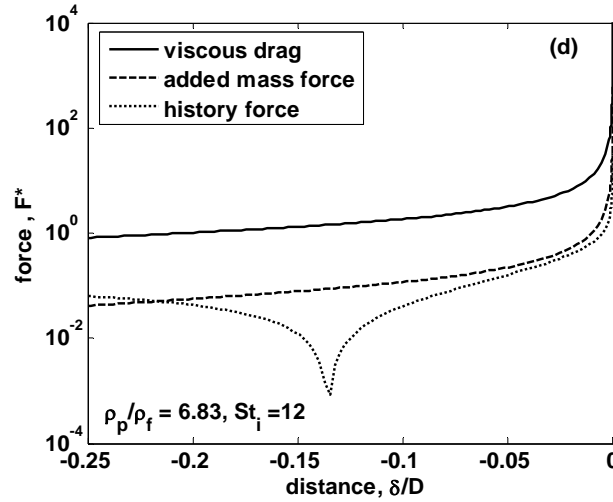


Figure 6.4. The three hydrodynamic forces as a function of the scaled gap, δ/D , for the impact of a steel pendulum, $\rho_p/\rho_f = 6.83$, at (a) $St_i = 488$, (b) $St_i = 198$, (c) $St_i = 42$, and (d) $St_i = 12$.

For all the investigated impact particle Stokes numbers, the steady viscous drag, F_D , dominates the hydrodynamic forces throughout the impact. The wall-modified added mass force is small relative to the drag because both of the canceling of the two terms in equation (6.2) and of the large density ratio. Part of the impact motion, the history force exceeds the wall-modified added mass force. The added mass and the history force become comparable when the particle Stokes number drops to $St_i = 12$ in figure 6.4(d). The sign change of the history force, indicated by the flip of the profile, is observed in all cases for the following reasons. During the early stages of the pendulum motion, the sphere accelerates due to the effective gravity, resulting in an opposing history force. The hydrodynamic forces decelerate the pendulum as it moves towards the wall and eventually change the sign of (dU_i/dt) in the time integral. The history force may then accumulate into a positive force that drives the pendulum. This sign inversion occurs sooner for a pendulum motion at smaller particle Stokes number, as suggested by the current simulation results.

If scaled by the viscous force, the added mass force is in general of two orders of magnitude smaller than unity, as shown in figure 6.5. These results also indicated that this force becomes more important for impacts at smaller St_i .

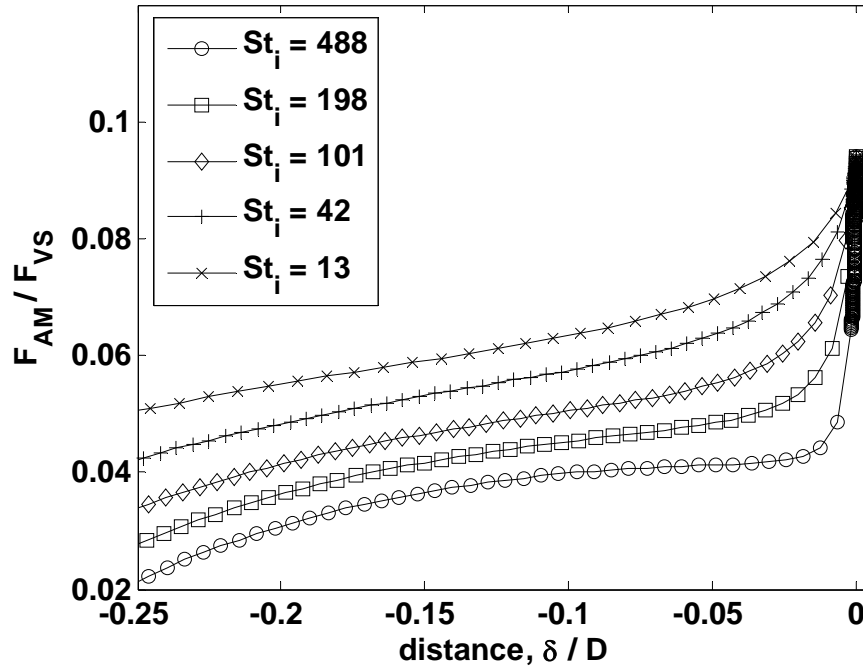


Figure 6.5. The local added mass force scaled by the steady viscous force, as a function of scaled gap and impact particle Stokes number with $\rho_p / \rho_f = 6.83$.

To obtain a general idea of how the added mass and the history force compare to the local viscous force, a series of simulation was performed over a range of impact particle Stokes numbers and different solid-to-liquid density ratios. The size, the string length, and the release angle of the pendulum were kept identical in these simulations. Different impact Stokes numbers were achieved by varying the liquid viscosity. The density ratios examined are $\rho_p / \rho_f = 1.5, 2.54, \text{ and } 7.6$. The comparisons are made at different locations from the wall.

The ratio of the local added mass force to the local viscous force, F_{AM}/F_D , is first shown in figure 6.6. In general, this force ratio increases with decreasing gap and density ratio. The dependence on the impact particle Stokes number exhibits a richer behavior than a monotonic relation. For an impact with a density ratio as high as 7.6, a monotonic increase of F_{AM}/F_D is observed as St drops. However, with decreasing density ratio, an inversion of the correlation between F_{AM}/F_D and St is observed at around $St = 100$. This might be attributed again to the canceling two terms in the wall-modified added mass force, one of which is sensitive to the local pendulum velocity and the other depends on the pendulum acceleration.

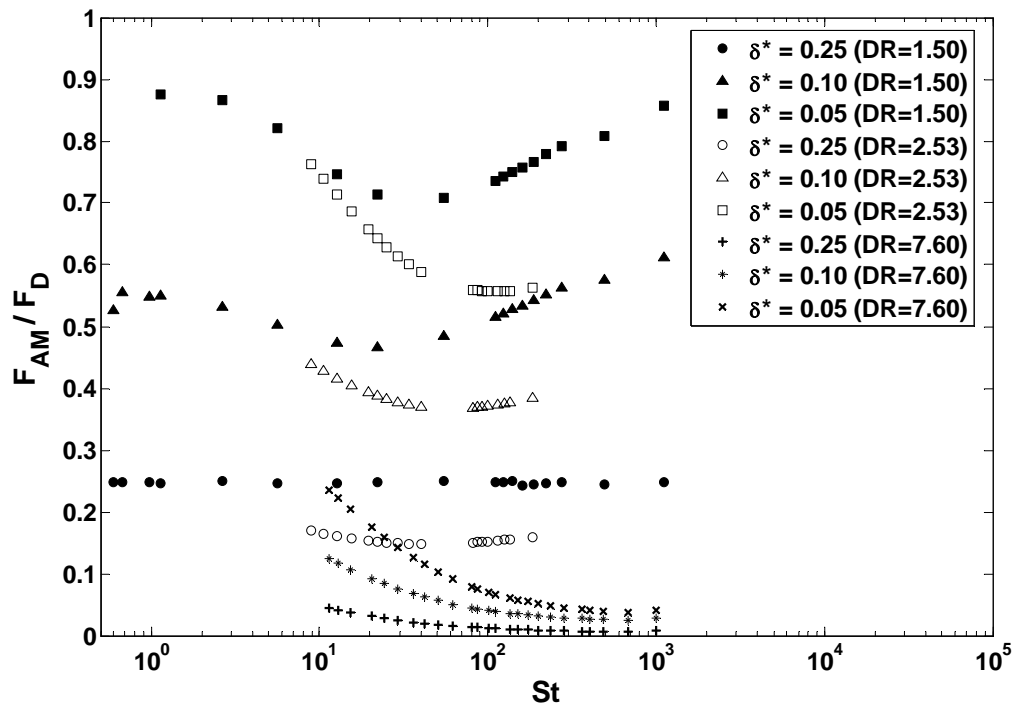


Figure 6.6. The local force ratio between the added mass force and the steady viscous force as a function of impact Stokes number, St , the gap width, $\delta^* = \delta/D$, and the solid-to-liquid density ratio, DR.

As for the local force ratio between the history and the viscous forces, F_H/F_D , a more uniform correlation with the investigated parameters is observed, in figure 6.7. The inversion in the dependence of F_H/F_D on St is again observed around $St = 100$, but in a convex manner rather than the concave inversion for F_{AM}/F_D . Instead of being a result of the immediate particle motion as in F_{AM}/F_D , this inversion is an accumulated consequence of the whole forcing history. From these sets of comparison, the local added mass and the history force are in general more important for a sphere that possesses a smaller density relative to the ambient liquid.

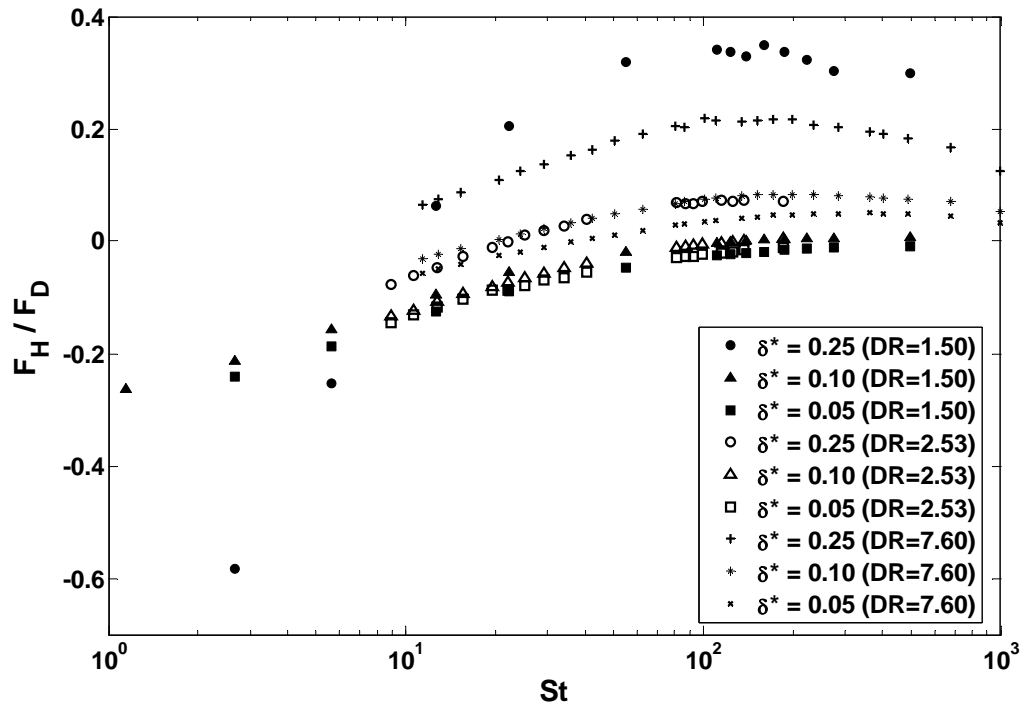


Figure 6.7. The local force ratio of the history mass force to the steady viscous force, as a function of impact Stokes number, St , the scaled gap width, $\delta^* = \delta/D$, and the solid-to-liquid density ratio, DR.

6.2 Influence distance

In order to address the interaction between the two approaching solid surfaces when the effects of the interstitial liquid are non-negligible, a set of experiments was conducted by Joseph et al. (2001). By keeping all the pendulum setups and the solid and the liquid properties nearly identical, they were able to compare experimentally the wall-decelerated velocity profile with that without wall. The two velocity profiles were scaled by the value when the sphere was of a distance of 1.5 diameters from the wall and a selection of their results is reproduced in figure 6.8. It is found that with decreasing particle Stokes number, the wall increasingly decelerates the sphere motion. It is also observed that the distance at which the deceleration becomes noticeable increases with decreasing St . It is this influence distance between the wall and the sphere that the following section addresses.

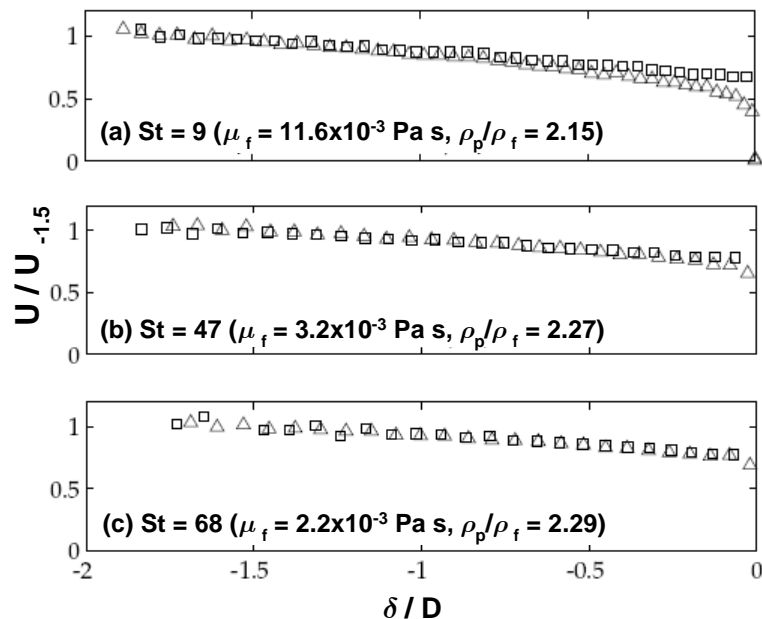


Figure 6.8. Comparison of the scaled velocity profile between a free swinging pendulum (\square) and a pendulum motion towards a wall (\triangle) (Joseph 2003).

To define a length scale that quantifies the wall effects in a simulation, two computations are performed. The first one calculates the free pendulum motion and a second simulation is made with the full flow model that accounts for the presence of the wall. Since there is no impact velocity that can be defined for a free pendulum motion, the characteristic Reynolds number, Re_c , is used to define the particle Stokes number, $St = (\rho_p/\rho_f)Re_c/9$, in this section. The *influence distance*, δ_f , is defined to be the gap where the velocity with the presence of the wall drops 1 % from the no-wall value. After the velocity profile of a free pendulum, U_{NW} , is obtained, a reference profile $0.99U_{NW}$ can be found, as shown by the dashed and the dotted-dashed line respectively in figure 6.9. The predicted velocity for the impact pendulum, $U(\delta^*)$, is calculated next, as shown by the solid line. The influence distance can be determined by the crossing of $0.99U_{NW}$ and $U(\delta^*)$. The case shown in figure 6.9 is for a pendulum of $\rho_p/\rho_f = 7.6$ with $Re_c = 488$.

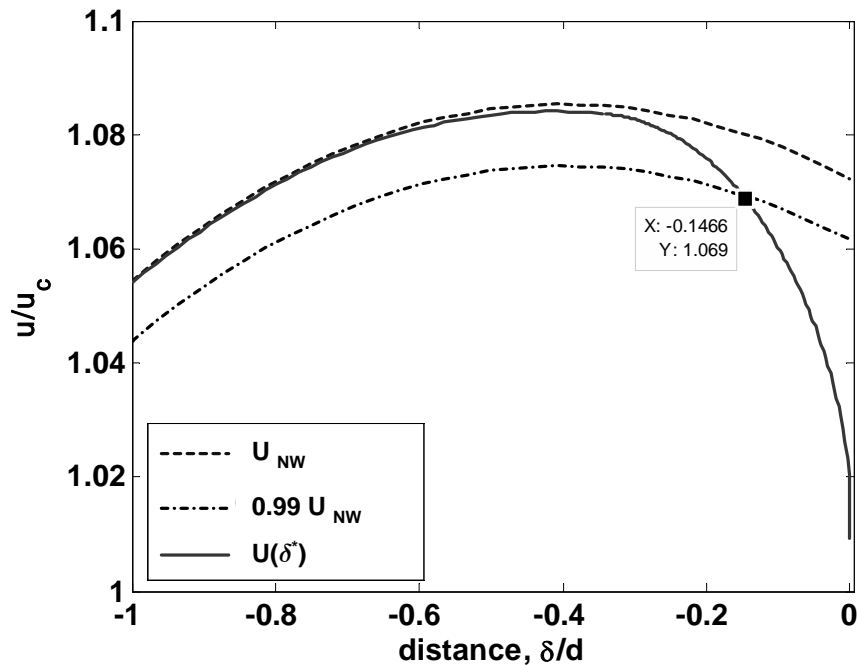


Figure 6.9. Determination of the influence distance by the intersection of $U(\delta^*)$ and $0.99U_{NW}$.

To show the ability of capturing the wall effects in a simulation, the first comparison is made at $Re_c = 530$ but with different density ratios. The free pendulum motion in each case, U_{NW} , is plotted along with the wall-inclusive profile, $U(\delta^*)$, in figure 6.10. It is observed that at smaller particle Stokes numbers, the wall-modified velocity deviates from U_{NW} at a greater distance than the one observed for higher St . This observation agrees qualitatively with the experimental findings in figure 6.8.

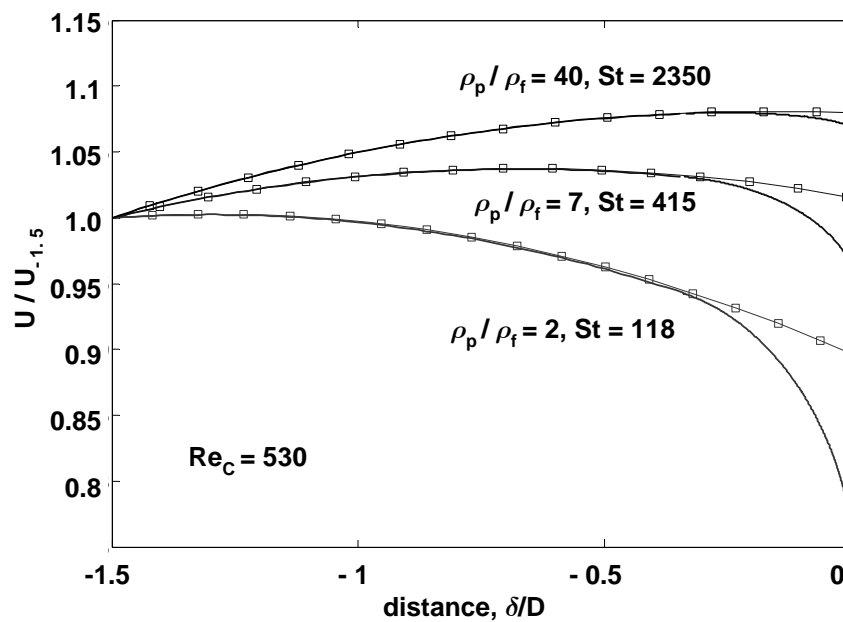


Figure 6.10. The scaled velocity profile for three pendulum motion at identical Re_c but different ρ_p/ρ_f . The free swing pendulum motion is plotted by the solid line with squares. The profile with the wall is indicated by the solid line.

The effect of the density ratio is more pronounced when comparing the results between $\rho_p/\rho_f = 100$ and $\rho_p/\rho_f = 2.5$ at the same Re_c in figure 6.11. Different sphere diameters are used for this particular simulation. The sphere trajectory with $\rho_p/\rho_f = 100$ resembles a pendulum motion in air, where no significant wall effects are predicted. However, for the case with a density ratio as low as $\rho_p/\rho_f = 2.5$, the particle decelerates significantly at a gap $\delta \approx 0.3D$. The latter motion simulates the motion of a

glass sphere at $St = 48$, corresponding to the case (c) in figure 6.8. The predicted velocity profile qualitatively agrees with the experimental observation.

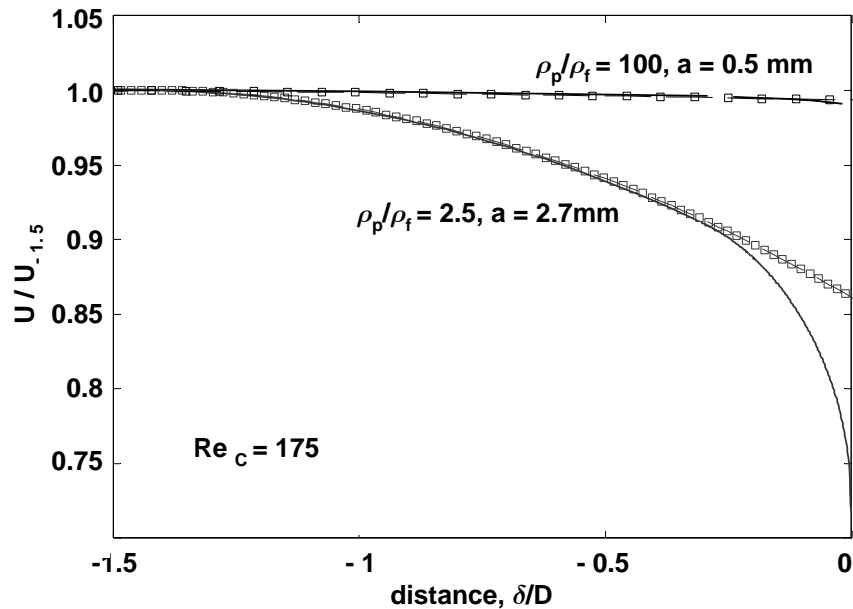


Figure 6.11. The scaled velocity profile for pendulum motion at identical Re_c but different ρ_p/ρ_f . The free pendulum motion is plotted by the solid line with squares. The profile with the wall is indicated by the solid bold line.

Similar computations were conducted for three density ratios, $\rho_p/\rho_f = 7.8, 2.5,$ and $1.5,$ for the approach of steel, glass, and Delrin spheres respectively. An additional set of computations with a nearly matching solid-to-liquid density ratio, $\rho_p/\rho_f = 1.1,$ was also performed. The pendulum string length is kept the same throughout the four sets of simulations. In order to achieve impacts over roughly the same range of particle Stokes numbers, $10 \leq St_B \leq 10^3,$ different particle sizes and pendulum release angles were used for each material. A larger particle and a greater release angle are used for impacts at a lower density ratio, and vice versa. The results are plotted in figure 6.12.

Except in the case of a nearly matching solid-to-liquid density ratio, $\rho_p/\rho_f = 1.1$, there exists a critical particle Stokes number that gives a minimum influence distance. For the case of $\rho_p/\rho_f = 7.6$, this critical Stokes number occurs at $St = 100 - 200$. For $\rho_p/\rho_f = 2.54$ and 1.5, the minimum occurs around $St = 10 - 30$ and $St \approx 10$. In the last extreme case, the influence distance shows a monotonic decrease with diminishing particle Stokes number. Within the investigated range of particle Stokes numbers, the data for $\rho_p/\rho_f = 1.1$ appears to reach either a plateau or a minimum. Further simulation at low St_B would be needed to determine the δ_f trend for a particle motion at such a low density ratio.

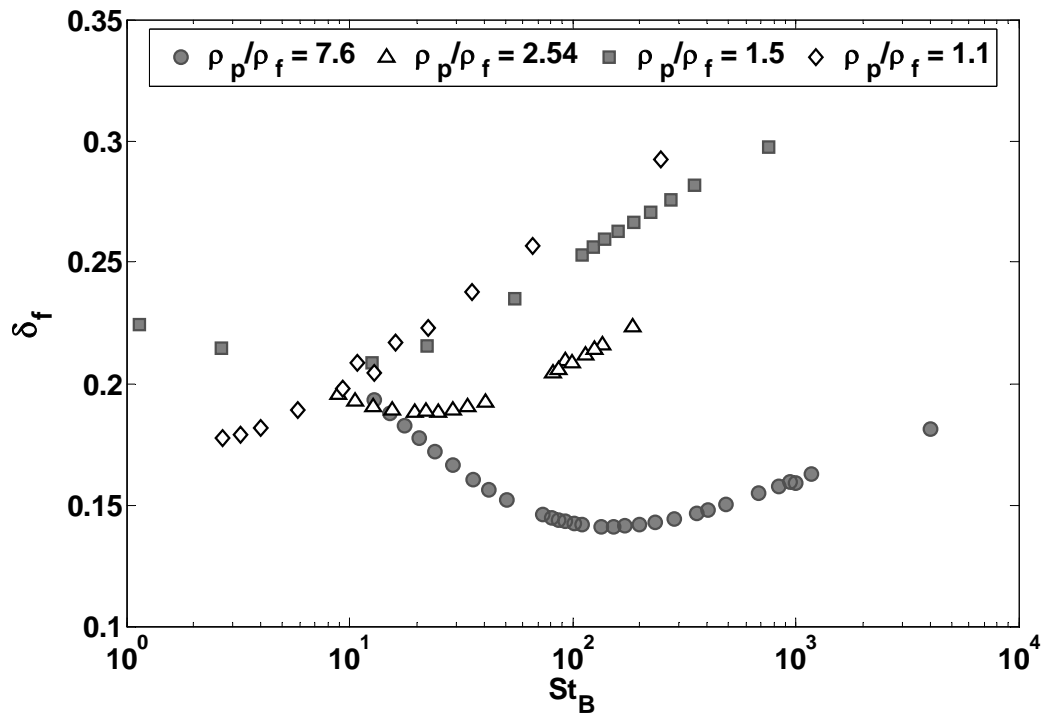


Figure 6.12. The dependence of the influence distance on the impact particle Stokes number and the solid-to-liquid density ratio.

This inversion may be related to the concave and convex variations observed in the correlation between F_{AM}/F_D , F_H/F_D and St . In general, F_{AM}/F_D changes with St faster

than F_H/F_D does. Thus, when the particle Stokes number starts to decrease from the critical value for the inversion in force ratios, F_{AM}/F_D increases more than the decrease in F_H/F_D . The resultant impact pendulum motion will thus deviate from the no-wall value at a greater distance yielding an increase in δ_f . However, since the two unsteady hydrodynamic forces are sensitive to the forcing history, the different pendulum configurations adopted in the current simulation may bring to the problem new factors that need to be addressed, including the pendulum release angle and the size ratio of a/L -the ratio between the particle size and the string length.

Over the investigated range of particle Stokes numbers, the influence distance in general increases with decreasing solid-to-liquid density ratio, which is in qualitative agreement with the experimental observations. A critical particle Stokes number is observed for a minimum δ_f for $\rho_p/\rho_f \geq 1.5$. This critical number decreases with decreasing density ratio while the resultant minimum influence distance increases with decreasing density ratio.

6.3 Summary

The proposed flow model was applied to investigate the local hydrodynamic forces during a pendulum impact on a wall. Since a collision process is intrinsically unsteady, the inclusion of the added mass force and the history force in the flow model is crucial for an accurate prediction. The two forces were shown to be of the same order of magnitude in the proximity of the wall. For a sphere of high solid-to-liquid density ratio, the added mass force is less important than for a light particle. Since both the added mass force and the history force depend strongly on the sphere forcing history, a rich behavior was observed in their dependences on the particle Stokes number and the density ratio.

An influence distance was defined to characterize the spatial interaction between the approaching surfaces. The full flow model was used to investigate how the particle Stokes number and the density ratio affect this length scale. Since the influence distance depends on the interstitial fluid motion, it exhibits complex correlation between the investigated parameters, which is in accordance with the observations for the fluid forces. However, a general trend was found that the influence distance decreases with increasing solid-to-liquid density ratio. Also noted is the existence of a critical impact Stokes number that results in a minimum influence distance for the investigated pendulum configuration. This critical value generally decreases with the density ratio.

Chapter 7

Conclusion

In the current work, the physics of an immersed collision have been investigated including the pre-collision and post-collision trajectories. Defining the normal along the line of centers when two spheres are in contact, the motion can be decomposed into its normal and tangential components of motion which are considered in this work with non-negligible hydrodynamic effects.

The experiments on the inter-particle immersed normal collision revealed two pertinent parameters that characterize the dynamic process. First, the effective coefficient of restitution serves as a measure of the particle momentum loss during one collision, taking into account the dissipation in both the solid and the liquid phases. The second parameter, the binary Stokes number, characterizes the particle inertia in terms of its ability to overcome the hydrodynamic forces sustaining the particle motion. The correlation between the two parameters exhibits a trend as observed in the experiments of particle-wall immersed collisions. As the binary Stokes number decreases, the effective coefficient of restitution drops from unity. Zero restitution was found when the binary Stokes number decreases to a critical value, below which the particle pair possesses no relative motion after collision.

The tangential component of motion for an inter-particle oblique collision has been examined at the sphere centers of mass and also at the contact point where the particle rotation is considered. The mobility of the target particle and the interstitial liquid layer prevent a pure sticking contact while sliding motion is often observed at the contact point. It was shown that the rebound motion at the particle center of mass can be predicted by an existing contact model, as long as the model parameters can be modified for the liquid effects. Using the measured effective normal coefficient of restitution and a proper lubricated friction coefficient, the contact model is able to predict the rebound motion of the impact sphere, enabling a description of the post-collision motion of the impact sphere. Due to the mobility of the target sphere, the prediction of the rebound angle of this sphere needs modifications. However, a qualitative description is possible within the frame of this work.

The normal effective coefficient of restitution has been determined to be the crucial parameter for an immersed collision. A general dependence on the binary Stokes number has been revealed for various immersed collisions—including the inter-particle collisions between identical or dissimilar spheres, as investigated in the current work, and the particle-wall collisions reported in the literature. The experimental finding motivated theoretical work that developed a flow model for the particle collision towards a wall and a feasible contact scheme.

To build the flow model, three conventional hydrodynamic forces—the steady viscous drag, the added mass force, and the history force—are considered and they all require modifications for the presence of the wall. Besides Brenner's wall correction on the steady viscous drag, the potential flow theory has been applied to modify the added mass force in this thesis. The presence of the wall introduces two new terms to the conventional added mass force—the first one behaves as an extra fluid mass that the

sphere needs to expel when accelerating and a second term affects the sphere motion like an additional dynamic pressure force. A modification on the history force is also proposed by considering the interplay of the unsteady boundary layer development and the wall-modified pressure field of the potential flow outside the boundary layer. All three forces diverge when the gap drops to zero, which is responsible for the near-wall deceleration of the particle motion. Such wall-amplified effect has been confirmed by a general agreement between the actual velocity profile and the model prediction.

As the last step of the building of the collision model, a rebound scheme has been developed that considers an asperity contact, an elstohydrodynamic contact, and a new mixed contact that considers the coupling between the first two schemes. Though no experimental evidence is available to validate the actual contact mechanism with the presence of interstitial liquid, the current collision model has been shown to better predict the effective coefficient of restitution than the existing EHL collision model, especially for an impact of a binary Stokes number about 100–400.

In the extent of the current work, the characteristics of a fully immersed inter-particle collision have been developed. The seemingly simple geometry exhibits a rich phenomenon suggesting a complex bulk behavior that is still poorly understood. The scope of this research is to provide a more realistic interaction law found in most of the current simulations by either using the current experimental findings as an empirical relation or adopting the collision model developed in this thesis. The targeted flow problems are those mixtures with equally important liquid and solid effects.

Bibliography

1. Bagchi, P. and Balachandar, S., 2003. Inertial and viscous forces on a rigid sphere in a straining flow at moderate Reynolds numbers, *J. Fluid Mech.* **481**, 105–148.
2. Barnocky, G. and Davis, R. H., 1988. Elastohydrodynamic collision and rebound of spheres: experimental verification, *Phys. Fluids* **31**, 1324–1329.
3. Basset, A. B., Treatise on hydrodynamics, Vol.2 1888. New York: Dover Publication Inc.
4. Batchelor, G. K., An introduction to fluid dynamics, 1967. New York: Cambridge University Press.
5. Boussinesq, 1885. ‘Sur la resistance qu’ oppose un liquide indefini en repos...’, *Comptes Rendu, Acad. Sci., Paris* **100**, 935–937.
6. Brenner, H., 1961. The slow motion of a sphere through a viscous fluid towards a plane surface, *Chem. Eng. Sci.* **16**, 242–251.
7. Campbell, C. S., 1990. Rapid granular flows, *Annu. Rev. Fluid Mech.* **22**, 57–92.
8. Chang, E. J. and Maxey, M. R., 1995. Unsteady flow about a sphere at low to moderate Reynolds number. Part 2. Accelerated motion, *J. Fluid Mech.* **303**, 133–153.
9. Clift, R., Grace, J. R., and Weber, M. E., Bubbles, drops, and particles 1978. New York: Academic Press.
10. Cox, R. and Brenner, H., 1967. The slow motion of a sphere through a viscous fluid towards a plane surface II: Small gap widths, including inertial effects, *Chem. Eng. Sci.* **22**, 1753–1777.
11. Crowe, C., Sommerfeld, M., and Tsuji, Y., Multiphase flows with droplets and particles 1998. Boca Raton, Florida: CRC Press.

12. Davis, R. H., Rager, D. A. and Good, B. T., 2002. Elastohydrodynamic rebound of spheres from coated surfaces, *J. Fluid Mech.* **468**, 107–119.
13. Davis, R. H., Serayssol, J.-M., and Hinch, E. J., 1986. The elastohydrodynamic collision of two spheres, *J. Fluid Mech.* **163**, 479–497.
14. Di Maio, F. P. and Di Renzo, A., 2004. Analytical solution for the problem of frictional-elastic collisions of spherical particles using the linear model, *Chem. Eng. Sci.* **59**, 3461–3475.
15. Einstein, A., 1906. The theory of the Brownian motion, *Annalen der Physik* **19(2)**, 371–381.
16. Gohar, R., *Elastohydrodynamics*, 2nd ed., 2001. London: Imperial College Press.
17. Goldsmith, W., *Impact: the theory and physical behaviour of colliding solids*, 1961. New York: Dover Publications.
18. Gondret, P., Lance, M., and Petit, L., 2002. Bouncing motion of spherical particles in fluids, *Phys. Fluids* **14(2)**, 643–652.
19. Iverson, R. M., 1997. The physics of debris flows, *Rev. Geophys.* **35(3)**, 245–296.
20. Johnson, K. L., *Contact mechanics*, 1985. New York: Cambridge University Press.
21. Joseph, G. G., 2003. Collisional dynamics of macroscopic particles in a viscous fluid, PhD thesis, California Institute of Technology, Pasadena, California.
22. Joseph, G. G. and Hunt, M. L., 2004. Oblique particle-wall collisions in a liquid, *J. Fluid Mech.* **510**, 71–93.
23. Joseph, G. G., Zenit, R., Hunt, M. L., and Rosenwinkel, A. M., 2001. Particle-wall collisions in a viscous fluid, *J. Fluid Mech.* **433**, 329–346.
24. Kantak, A. A. and Davis, R.H., 2004. Oblique collisions and rebound of spheres from a wetted surface, *J. Fluid Mech.* **509**, 63–81.
25. Kharaz, A. H., Gorham, D. A. and Salman, A. D., 2001. An experimental study of the elastic rebound of sphere, *Powder Technol.* **120**, 281–291.
26. Kim, I., Elghobashi, S. and Sirignano, W. A., 1998. On the equation for spherical-particle motion: effect of Reynolds and acceleration numbers, *J. Fluid Mech.* **367**, 221–253.

27. Lamb, H., *Hydrodynamics*, 6th ed., 1932. New York: Dover Publications.
28. Landau, L. D. and Lifshitz, E. M., *Fluid mechanics*, 2nd ed. 1987. London: Elsevier.
29. Maw, N., Barber, J. R. and Fawcett, J. N., 1976. The oblique impact of elastic spheres, *Wear* **38**, 101–114.
30. Maw, N., Barber, J. R. and Fawcett, J. N., 1981. The role of elastic tangential compliance in oblique impact, *Trans. ASME F: J. Lubric. Tech.* **103**, 74–80.
31. McLaughlin, M. H., 1968. An experimental study of particle-wall collision relating to flow of solid particles in a fluid, Engineer degree thesis, California Institute of Technology, Pasadena, California.
32. Mei, R., 1994. Flow due to an oscillating sphere and an expression for unsteady drag on the sphere at finite Reynolds number, *J. Fluid Mech.* **270**, 133–174.
33. Mei, R. and Adrian, R. J., 1992. Flow past a sphere with an oscillation in the free-stream velocity and unsteady drag at finite Reynolds number, *J. Fluid Mech.* **237**, 323–341.
34. Michaelides, E. E., 1997. Review—The transient equation of motion for particles, bubbles, and droplets, *Trans, ASME: J. Fluids Eng.* **119**, 223–247.
35. Milne-Thomson, L. M., *Theoretical hydrodynamics*. 5th ed., 1968. New York: Dover Publications.
36. Nguyen, N. Q. and Ladd, A. J. C., 2002. Lubrication corrections for lattice-Boltzmann simulations of particle suspensions, *Phys. Rev. E* **66(4)**, Art. No. 046708 Part 2.
37. Nott, P. R. and Brady, J. F., 1994. Pressure-driven flow of suspensions: simulations and theory, *J. Fluid Mech.* **275**, 157–199.
38. Odar, F. and Hamilton, W. S., 1964. Forces on a sphere accelerating in a viscous fluid, *J. Fluid Mech.* **18**, 302–314.
39. Panton, R. L., *Incompressible flow*, 1995. New York: John Wiley & Sons.
40. Potapov, A. V., Hunt, M. L. and Campbell, C. S., 2001. Liquid-solid flows using smoothed particle hydrodynamics and the discrete element method, *Powder Technol.* **116(2-3)**, 204–213.
41. Press, W. H., Teukolsky, S. A., Vetterling, W. T., and Flannery, B. P,

Numerical Recipes, Vol.1 1996. New York: Cambridge University Press.

42. Schlichting, H. and Kestin, J., Boundary layer theory, 4th ed., 1960. New York: McGraw-Hill.
43. Stokes, G. G., 1845. On the theories of internal friction of the fluids in motion, *Trans. Cambridge Phil. Soc.* **8**, 287–319.
44. Stokes, G. G., 1851. On the effect of internal friction of fluids on the motion of pendulum, *Trans. Cambridge Phil. Soc.* **9**, 8–106.
45. Zenit, R. and Hunt, M. L., 1998. The impulsive motion of a liquid resulting from a particle collision, *J. Fluid Mech.* **375**, 345–361.
46. Zhang, D. Z. and Prosperetti, A., 1994. Averaged equations for inviscid disperse two-phase flow, *J. Fluid Mech.* **267**, 185–219.

Appendix

This appendix provides the Fortran program used in chapter 4 for an immersed pendulum motion towards a wall.

```

c-----Immersed Pendulum with wall [beyond creeping flow]-----
c
c factor on length scale (f_N:=Ltheta/2a)
c History force: Kim's kernel
c e_dry used (0.97 for steel and glass beads)
c sign convention (u+,s- for approach)(u-,s- for rebound)
c wall @ +a
c Neville's algorithm for extrapolation
c ** ds/dt = U
c ** MpdU/dt = G -(Mp+Mf*/2)dU/dt -Fp-Fd-Fh
c
c-----fuling Jan/27/2006-----
      IMPLICIT DOUBLE PRECISION (A-H,O-Z)
      parameter (delt = 1.0D-3)
      parameter (len = 1000/ delt, no=4)
      parameter (conv =1.0D-5,mo1=5,mo2=200,mo3=1)
      parameter (conv2 =1.0D-8 )
      parameter (pi = 3.1415926D0)
      real(8) dudt(len),u(len),t(len)
      real(8) yprv(no),zprv(no),aprv(no)
      open (1,file='PDW3A_a.txt')
      open (2,file='PDW3A_b.txt')
      open (3,file='PDW3A_c.txt')

c--input parameter-----
c Ton: cha. conv. time, ReT: cha. Reynolds number
c DR: density ratio, ang_ini: release angle, pd: particle diameter
c sL: string length, xc: rebound position
c-----
      Ton = 1.4127D0
      ReT = 198.952D0
      DR = 7.6D0
      ang_ini = 10.D0
      pd = 6.35D0

```

```

test = 0.6D0
sL = 105.D0
aL = 0.5D0*pd/sL
thre = conv
xc = 1.29D-6
e_dry = 0.97D0
c--e_wet: dissipation parameter
c    e_wet = 1.D0
    e_wet = 1.D0-12.D0/12.8934D0
c--initial angle in radians
    s0 = ang_ini*pi/180.D0
c--testing distances
    p1 = 0.6D0
    p2 = 0.1D0
c--y: circumf. position, z: velocity
    tini = 0.D0
    yini = -1.D0
    zini = 0.0
c--uter field PD file
    step = delt*10.D0
    write (1,*) 'dia=',pd,'DR=',DR
    write (1,*) 'Re=',ReT,'Ton=',Ton
    write (1,*) 'aL=',aL,'iniang=',ang_ini
    write (1,*) 'edry=',e_dry,'e_wet=',e_wet
    write (1,*) 'xc=',xc
    write (1,80) '1-tn','2-pos','3-h*','4-vel','5-vh','6-fg','7-fd',
&    '8-fa','9-fh','10-fp','11-dudt','12-ems','13-cd1','14-HF'
    re = abs(zini) * ReT
    cd = 1.D0 + 0.15D0 * re**(0.687D0)
    hist = 0.D0
    tn = tini
    yn = yini
    zn = zini
    dudt = 0.D0
c--Added mass subroutine (outer)
    call amout(yn,aL,s0,w0,dw0)
    aa = DR + 0.5D0*(1.D0 + 3.D0*w0)
    dzdt = -(DR-1.D0)*(Ton**2.D0)*dsin(yn*s0)/aa/s0

    m = 1
    u(m) = zn
    dudt(m) = dzdt
    t(m) = tn
c--impact motion (out-regime)-----
do 10 i=1,9999999
    call rk4 (tn,yn,zn,t,u,dudt,len,m,Ton,DR,aL,s0,ReT,

```

```

&      step,ynn,znn)
      yn = ynn
      zn = znn
      tn = tn + step

      call histKim(tn,t,u,dudt,len,m,aL,s0,ReT,hist)
      call Hfact(yn,aL,s0,H_N)
      hist = hist * H_N
      call derivg (yn,zn,Ton,DR,aL,s0,ReT,hist,ems,
&      fg,fd,fp,fh,dzdt)
      yh = dsin(yn*s0)/(2.D0*aL)

      if (mod(i,mol).eq.0) then
      fa = -dzdt*(ems-DR)/ems + fp
c--output yh : gap/D
      vh = zn*dcos(yn*s0)
      write (1,87) tn,yn,yh,zn,vh,fg,fd,fa,fh,fp,dzdt,ems,cd,H_N
      end if
      m = m + 1
      u(m) = dabs(zn)
      dudt(m) = dzdt
      t(m) = tn
c--matching of outer/inner viscous drag
      if (yh .ge. -p1) then
      if (yh .le. -xc) then
      re = ReT * dabs(zn)
      sc = dsin(yn*s0)/aL
      be = 1.D0/dabs(sc) - 0.2D0*(1.D0+0.25D0*re)*dLOG(dabs(sc))
      cd = 1.D0 + 0.15D0 * (re**0.687D0)
      print *,be,cd
      if (dabs(be-cd) .le. test) then
      goto 30
      end if
      else
      goto 90
      end if
      end if
      if (zn .le. conv2) then
      print *, 'stop in outer regime'
      goto 90
      end if
10  continue
*****
*      !Near Wall regime!
*****
30  print *, 'near-wall regime'

```

```

c--Re_imp for Brenner's correction factor
  Re_imp = ReT * dabs(zn)
  step = delt/10.D0
  mo4 = 5
  write (2,*) 'dia=',pd,'DR=',DR
  write (2,*) 'Re=',ReT,'Ton=',Ton
  write (2,*) 'aL=',aL,'iniang=',ang_ini
  write (2,*) 'edry=',e_dry,'e_wet=',e_wet
  write (2,*) 'xc=',xc,'Re_imp',Re_imp
  write (2,80) '1-tn','2-pos','3-h*','4-vel','5-vh','6-fg','7-fd',
  & '8-fa','9-fh','10-fp','11-dudt','12-ems','13-lamda','14-H_F'
c--Added mass (inner regime)-----
  call amin(yn,aL,s0,w0,dw0)
  aa = DR + 0.5D0*(1.D0 + 3.D0*w0)
  sc = dsin(yn*s0)/aL
  be = 1.D0/dabs(sc) - 0.2D0*(1.D0+0.25D0*Re_imp)*dLOG(dabs(sc))
c-----
  dzdt = - (DR-1.D0)*(Ton**2.D0)*dsin(yn*s0)/aa/s0
  & - 9.D0*s0*dabs(be*zn)/aL/ReT/aa
  & - 0.75D0*s0*dabs(dw0)*zn*zn/aL/aa
  & - 9.0D0*s0*hist/aL/ReT/aa
c--velocity, acceleration history string
  u(m) = zn
  dudt(m) = dzdt
  t(m) = tn
c--Neville's
  yn05 = 0.D0
  zn05 = 0.D0
  yn04 = 0.D0
  zn04 = 0.D0
  yn03 = 0.D0
  zn03 = 0.D0
  yn02 = 0.D0
  zn02 = 0.D0
  yn01 = 0.D0
  zn01 = 0.D0

do 40 i=1,99999999
  yn05 = yn04
  zn05 = zn04
  yn04 = yn03
  zn04 = zn03
  yn03 = yn02
  zn03 = zn02
  yn02 = yn01

```

```

    zn02 = zn01
    yn01 = yn
    zn01 = zn
    call rk41W(tn,yn,zn,t,u,dudt,len,m,Ton,DR,aL,s0,ReT,Re_imp,
&      step,ynn,znn)
    yn = ynn
    zn = znn
    tn = tn + step
    call histKim(tn,t,u,dudt,len,m,aL,s0,ReT,hist)
    call Hfact(yn,aL,s0,H_N)
    hist = hist * H_N

    call deg1(yn,zn,Ton,DR,aL,s0,ReT,hist,Re_imp,
&  ems,fg,fd,fp,fh,bre,dzdt)

c--output forces: viscous drag(fd), pressure(fp),history force(fh)-----
    if (yn .le. -xc) then
        if (yn .ge. -10.D0*xc) then
            step = delT / 100.D0
            mo4 = 1
        end if
        if (zn .ge. conv2) then
            if (mod(i,mo4) .eq. 0) then
                fa = -dzdt*(ems-DR)/ems + fp
                yh = dsin(yn*s0)/(2.D0*aL)
                vh = zn*dcos(yn*s0)
                write (2,87) tn,yn,yh,zn,vh,fg,fd,fa,fh,fp,dzdt,ems,bre,H_N
            end if
            m = m + 1
            u(m) = zn
            dudt(m) = dzdt
            t(m) = tn
        else
            print *, 'stop before wall'
            goto 90
        end if
    else
c-----extrapolate velocity, acceleration at xc-----
        write (3,87) tn,yn,yh,zn,vh,fg,fd,fa,fh,fp,dzdt,ems,bre,H_N
        aprv = (/dudt(m-4), dudt(m-3), dudt(m-2), dudt(m-1)/)
        yprv = (/yn05, yn04, yn03, yn02/)
        zprv = (/zn05, zn04, zn03, zn02/)
        tn = tn-step+(dabs(yn01)-xc)/dabs(zn01)
        yn = -xc
c--Neville's algorithm
        call polint(yprv,zprv,no,-xc,zn,d_zn)

```

```

call polint(yprv,apr,v,no,-xc,dzdt,d_zn)
print *,'wall=',xc
write (2,87) tn,yn,yh,zn,vh,fg,fd,fa,fh,fp,dzdt,ems,bre,H_N
goto 50
end if
40 continue
c-----!rebound!-----
50 print *, 'rbd course'
   zn = -zn * e_dry * e_wet
   print *,'rbd velocity=',zn
   u(m) = zn
   t(m) = tn
   step = delt/10.D0
   write (3,*) 'dia=',pd,'DR=',DR
   write (3,*) 'Re=',ReT,'Ton=',Ton
   write (3,*) 'aL=',aL,'iniang=',ang_ini
   write (3,*) 'edry=',e_dry,'e_wet=',e_wet
   write (3,*) 'xc=',xc
   write (3,80) '1-tn','2-pos','3-h*','4-vel','5-vh','6-fg','7-fd',
& '8-fa','9-fh','10-fp','11-dudt','12-ems','13-lamda','14-H_N'

do 60 i=1,99999999
call rk42W(tn,yn,zn,t,u,dudt,len,m,Ton,DR,aL,s0,ReT,Re_imp,
&      step,ynn,znn)
   yn = ynn
   zn = znn
   tn = tn + step
call histKim(tn,t,u,dudt,len,m,aL,s0,ReT,hist)
call Hfact(yn,aL,s0,H_N)
hist = hist * H_N
call deg2(yn,zn,Ton,DR,aL,s0,ReT,hist,Re_imp,
&      ems,fg,fd,fp,fh,bre,dzdt)
if (yh .ge. -p2) then
  if (zn .le. -conv2) then
    if (mod(i,mo3) .eq. 0) then
      fa = -dzdt*(ems-DR)/ems + fp
      yh = dsin(yn*s0)/(2.D0*aL)
      vh = zn*dcos(yn*s0)
      write (3,87) tn,yn,yh,zn,vh,fg,fd,fa,fh,fp,dzdt,ems,bre,H_N
    end if
    m = m + 1
    u(m) = zn
    dudt(m) = dzdt
    t(m) = tn
  else
    goto 92
  end if
end if

```

```

endif
  else
    goto 90
  endif
60 continue

80 format(1x,A16,1x,A16,1x,A16,1x,A16,1x,A16,1x,A16,1x,A16,
& 1x,A16,1x,A16,1x,A16,1x,A16,1x,A16,1x,A16)
87 format(1x,F16.8,1x,F16.8,1x,F16.8,1x,F16.8,1x,F16.8,1x,F16.8,
& 1x,F16.8,1x,F16.8,1x,F16.8,1x,F16.8,1x,F16.8,1x,F16.8,
& 1x,F16.8,1x,F16.8)

90 print *, 'stop in out regime'
92 print *, 'stop after rbd'
94 print *, 'finish one collision'
  pause
  end

c*****
c History force: Kim et al.
c*****
  subroutine histKim(time,t,u,dudt,len,m,aL,s0,ReT,sum)
  IMPLICIT DOUBLE PRECISION (A-H,O-Z)
  real(8) t(len),u(len),dudt(len)
c-----time: present time
  pi=3.1415926D0
  c1 = 2.5D0
  c2 = 22.D0
  c3 = 0.07D0
  c4 = 0.25D0
  c5 = 0.126D0
  sum = 0.D0

  do 200 j = 1,m-1
    eta = (time - t(j))
    re = ReT * dabs(u(j))
    vf3 = (dabs(u(j))/(0.75D0 + c5*re))**3.D0
    if (j .eq. 1) then
      G = 1.D0
      dk = (2.D0*pi*s0*eta/aL/ReT)**0.25D0
& + G*(0.25D0*pi*s0*s0*eta*eta*ReT*vf3/aL/aL)**(1/c1)
    else
      ac1 = dabs(dudt(j))/(u(j)**2.D0)

    if (dudt(j) .eq. 0.D0) then
      beta = 0.D0
    else

```

```

acr = dabs(dudt(j)-dudt(j-1))/(t(j)-t(j-1))/dabs(u(j)*dudt(j))
beta = c2 / (1.D0 + acr**(1.D0+c4)/c3/(acr+acr**c4))
endif
G = 1.D0 / (1.D0 + beta*dsqrt(ac1))
dk = (2.D0*pi*s0*eta/aL/ReT)**(0.5D0/c1)
& + G*(0.25D0*pi*s0*s0*eta*eta*ReT*vf3/aL/aL)**(1/c1)
endif
sum = sum + dudt(j)*(t(j+1)-t(j))/(dk**c1)
200 continue
return
end

c*****
c Wall correction term for Added mass force (outer)
c*****
subroutine amout(pos,aL,s0,w,dw)
IMPLICIT DOUBLE PRECISION (A-H,O-Z)
c-----h* :=h/a (where s*:=s/2a)-----
w = 0.D0
dw = 0.D0
dh = dsin(dabs(pos)*s0)/aL + 1.D0
hh = dh**2.D0

w = 1.D0/(8.D0*(dh**3.D0)) + 1.D0/(4.D0*hh-1.D0)**3.D0
& +1.D0/(4.D0*dh*(2.D0*hh-1.D0))**3.D0
& +1.D0/(16.D0*hh*hh-12.D0*hh+1.D0)**3.D0
& +1.D0/(2.D0*dh*(16.D0*hh*hh-16.D0*hh+3.D0))**3.D0
& +1.D0/(64.D0*(hh**3.D0)-80.D0*hh*hh+24.D0*hh-1.D0)**3.D0
&+1.D0/(8.D0*dh*(16.D0*(hh**3.D0)-24.D0*hh*hh+10.D0*hh-1.D0))**3.D0

dw = 1.D0/(128.D0*hh*(hh-1.D0)*((2.D0*hh-1.D0)**3.D0))
& - 1.5D0*dh*(4.D0*hh-3.D0)/((hh-1.D0)*((4.D0*hh-1.D0)**4.D0))
& + 0.5D0*dh/((hh-1.D0)*((4.D0*hh-1.D0)**3.D0))
& - (8.D0*hh*(hh-1.D0)+1.D0)/
& (128.D0*hh*hh*(hh-1.D0)*((2.D0*hh-1.D0)**4.D0))
& + 1.D0/(16.D0*hh*(hh-1.D0))
& -(2.D0*hh-1.D0)/(16.D0*hh*hh*(hh-1.D0))
return
end

c*****
c Wall correction term on AM (inner)
c*****
subroutine amin(pos,aL,s0,w,dw)
IMPLICIT DOUBLE PRECISION (A-H,O-Z)
c-----h* :=h/a (where s*:=s/2a)-----
w = 0.D0

```

```

dw = 0.D0
dh = dsin(dabs(pos)*s0)/aL + 1.D0
hh = dh**2.D0

w = 1.D0/(8.D0*(dh**3.D0)) + 1.D0/(4.D0*hh-1.D0)**3.D0
& +1.D0/(4.D0*dh*(2.D0*hh-1.D0))**3.D0
& +1.D0/(16.D0*hh*hh-12.D0*hh+1.D0)**3.D0
& +1.D0/(2.D0*dh*(16.D0*hh*hh-16.D0*hh+3.D0))**3.D0
& +1.D0/(64.D0*(hh**3.D0)-80.D0*hh*hh+24.D0*hh-1.D0)**3.D0
& +1.D0/(8.D0*dh*(16.D0*(hh**3.D0)-24.D0*hh*hh+10.D0*hh-1.D0))**3.D0

dw = 0.240636D0 - 0.000230238D0/(dh-1.D0)**0.5D0
& - 0.310507D0*(dh-1.D0)**0.5D0 + 0.0660344D0*(dh-1.D0)
& + 0.0979599*dLog(dh-1.D0)
& - 0.000205554D0*dLog(dh-1.D0)/(dh-1.D0)**0.5D0
return
end
c*****
c History factor augmentaion factor H(epsilon)
c*****
subroutine Hfact(pos,aL,s0,HF)
IMPLICIT DOUBLE PRECISION (A-H,O-Z)
c----h* :=h/a (where pos = Ltheta/Ltheta0)-----
dh = dsin(dabs(pos)*s0)/aL + 1.D0
hh = dh**2.D0
h3 = dh**3.D0

HF = 1.D0 - 3.D0/(1.D0 - 4.D0*hh)**3.D0
& - 0.015625D0/(dh - 2.D0*h3)**3.D0
& + 3.D0/(1.D0 - 12.D0*hh + 16.D0*hh*hh)**3.D0
& + 0.375D0/(3.D0*dh - 16.D0*h3 + 16.D0*hh*h3)**3.D0
& + (0.375D0 - 0.03125D0/(1.D0 - 2.D0*hh)**3.D0)/dh**3.D0
HF = dabs(HF)**1.5D0
return
end
*****Outer PD*****
subroutine derivg(pos,vel,Ton,DR,aL,s0,ReT,hsum,am,
& f_grav,f_drag,f_pres,f_hist,dy)
IMPLICIT DOUBLE PRECISION (A-H,O-Z)
c----y:position/ z:vel
c----sref: reference gravity scale
dh = dabs(dsin(pos*s0)/aL)
if (dh .lt. 1.D0) then
call amin(pos,aL,s0,w,dw)
else
call amout(pos,aL,s0,w,dw)

```

```

endif

am = DR + 0.5D0 * (1.D0 + 3.D0*w)
re = ReT * dabs(vel)
c_d = 1.D0 + 0.15D0*(re**(0.687D0))

f_grav = - (DR-1.D0)*(Ton**2.D0)*dsin(pos*s0)/am/s0
f_drag = -9.0D0*s0*dabs(vel)*c_d/aL/ReT/am
f_hist = -9.0D0*s0*hsum/aL/ReT/am
f_pres = -0.75D0*s0*dabs(dw)*vel*vel/aL/am
dy = f_grav + f_drag + f_hist + f_pres
return
end

*****outer PD for RK4*****
subroutine derivgRK4(pos,vel,Ton,DR,aL,s0,ReT,hsum,dy)
IMPLICIT DOUBLE PRECISION (A-H,O-Z)
dh = dabs(dsin(pos*s0)/aL)
  if (dh .lt. 1.D0) then
    call amin(pos,aL,s0,w,dw)
  else
    call amout(pos,aL,s0,w,dw)
  endif
am = DR + 0.5D0 * (1.D0 + 3.D0*w)
re = ReT * dabs(vel)
c_d = 1.D0 + 0.15D0*(re**(0.687D0))
dy = - (DR-1.D0)*(Ton**2.D0)*dsin(pos*s0)/am/s0
& -9.0D0*s0*dabs(vel)*c_d/aL/ReT/am
& -9.0D0*s0*hsum/aL/ReT/am
& -0.75D0*s0*dabs(dw)*vel*vel/aL/am
return
end

*****Outer PD*****
subroutine rk4(trk4,yrk4,zrk4,t,u,dudt,len,m,Ton,
& DR,aL,s0,ReT,step,yout,zout)
IMPLICIT DOUBLE PRECISION (A-H,O-Z)
c-----t,y,z: time, position, velocity inputs
  real(8) t(len),u(len),dudt(len)
  h6 = step/6.D0
c-----xh:time, yh:position, zh: velocity
  th = trk4 + 0.5D0*step
  yh = yrk4 + 0.5D0*step*u(m)
  zh = zrk4 + 0.5D0*step*dudt(m)
c ----k2
  call histKim(th,t,u,dudt,len,m,aL,s0,ReT,hsum)
  call Hfact(yh,aL,s0,HN)
  hsum = hsum * HN

```

```

dyt = dabs(zh)
call derivgRK4(yh,zh,Ton,DR,aL,s0,ReT,hsum,dzt)
yh = yrk4 + 0.5D0*step*dyt
zh = zrk4 + 0.5D0*step*dzt
c ----k3
call histKim(th,t,u,dudt,len,m,aL,s0,ReT,hsum)
call Hfact(yh,aL,s0,HN)
hsum = hsum * HN
dym = dabs(zh)
call derivgRK4(yh,zh,Ton,DR,aL,s0,ReT,hsum,dzm)
yh = yrk4 + step*dym
zh = zrk4 + step*dzm
dym = dyt + dym
dzm = dzt + dzm
c ----k4
th = trk4 + step
call histKim(th,t,u,dudt,len,m,aL,s0,ReT,hsum)
call Hfact(yh,aL,s0,HN)
hsum = hsum * HN
dyt = dabs(zh)
call derivgRK4(yh,zh,Ton,DR,aL,s0,ReT,hsum,dzt)
yout = yrk4 + h6*(u(m) + 2.D0*dym + dyt)
zout = zrk4 + h6*(dudt(m) + 2.D0*dzm + dzt)
return
end
c*****
c          !near wall subroutines!
c*****
subroutine deg1(pos,vel,Ton,DR,aL,s0,ReT,hsum,Re_imp,
& am,f_grav,f_drag,f_pres,f_hist,B,dy)
IMPLICIT DOUBLE PRECISION (A-H,O-Z)
c-----Re_imp: inner field impact Reynold's number
call amin(pos,aL,s0,w,dw)
am = DR + 0.5D0 * (1.D0 + 3.D0*w)
re = ReT * dabs(vel)
c_d = 1.D0
dh = dsin(pos*s0)/aL
B = 1.D0/dabs(dh) - 0.2D0*(1.D0+0.25D0*Re_imp)*dLOG(dabs(dh))
f_grav = - (DR-1.D0)*(Ton**2.D0)*dsin(pos*s0)/am/s0
f_drag = -9.D0*s0*c_d*dabs(B*vel)/aL/ReT/am
f_pres = -0.75D0*s0*dabs(dw)*vel*vel/aL/am
f_hist = -9.0D0*s0*hsum/aL/ReT/am
dy = f_grav + f_drag + f_pres + f_hist
return
end
*****rebound subroutine*****

```

```

subroutine deg2(pos,vel,Ton,DR,aL,s0,ReT,hsum,Re_imp,
& am,f_grav,f_drag,f_pres,f_hist,B,dy)
  IMPLICIT DOUBLE PRECISION (A-H,O-Z)
c-----re0: inner field impact Reynold's number
  call amin(pos,aL,s0,w,dw)
  am = DR + 0.5D0 * (1.D0 + 3.D0*w)
  re = ReT * dabs(vel)
  c_d = 1.D0
  dh = dsin(pos*s0)/aL
  B = 1.D0/dabs(dh) - 0.2D0*(1.D0-0.25D0*Re_imp)*dLOG(dabs(dh))
  f_grav = - (DR-1.D0)*(Ton**2.D0)*dsin(pos*s0)/am/s0
  f_drag = +9.D0*s0*c_d*dabs(B*vel)/aL/ReT/am
  f_pres = -0.75D0*s0*dabs(dw)*vel*vel/aL/am
  f_hist = -9.0D0*s0*hsum/aL/ReT/am
  dy = (f_grav + f_drag + f_pres + f_hist)
  return
end
*****NW for RK4*****
subroutine derk41W(pos,vel,Ton,DR,aL,s0,ReT,Re_imp,hsum,dy)
  IMPLICIT DOUBLE PRECISION (A-H,O-Z)
c-----Re_imp: inner field impact Reynold's number
  call amin(pos,aL,s0,w,dw)
  am = DR + 0.5D0 * (1.D0 + 3.D0*w)
  re = ReT * dabs(vel)
  c_d = 1.D0
  dh = dsin(pos*s0)/aL
  B = 1.D0/dabs(dh) - 0.2D0*(1.D0+0.25D0*Re_imp)*dLOG(dabs(dh))
  dy = - (DR-1.D0)*(Ton**2.D0)*dsin(pos*s0)/am/s0
&   -9.D0*s0*c_d*dabs(B*vel)/aL/ReT/am
&   -0.75D0*s0*dabs(dw)*vel*vel/aL/am
&   -9.0D0*s0*hsum/aL/ReT/am
  return
end

*****NW rebound for RK4*****
subroutine derk42W(pos,vel,Ton,DR,aL,s0,ReT,Re_imp,hsum,dy)
  IMPLICIT DOUBLE PRECISION (A-H,O-Z)
c-----Re_imp: inner field impact Reynold's number
  call amin(pos,aL,s0,w,dw)
  am = DR + 0.5D0 * (1.D0 + 3.D0*w)
  re = ReT * dabs(vel)
  c_d = 1.D0
  dh = dsin(pos*s0)/aL
  B = 1.D0/dabs(dh) - 0.2D0*(1.D0-0.25D0*Re_imp)*dLOG(dabs(dh))
  dy = - (DR-1.D0)*(Ton**2.D0)*dsin(pos*s0)/am/s0
&   +9.D0*s0*c_d*dabs(B*vel)/aL/ReT/am

```

```

&   -0.75D0*s0*dabs(dw)*vel*vel/aL/am
&   -9.0D0*s0*hsum/aL/ReT/am
return
end
*****NW*****
subroutine rk41W(trk4,yrk4,zrk4,t,u,dudt,len,m,Ton,DR,aL,s0,
&           ReT,Re_imp,step,yout,zout)
IMPLICIT DOUBLE PRECISION (A-H,O-Z)
real(8) t(len),u(len),dudt(len)
h6 = step/6.D0
th = trk4 + 0.5D0*step
yh = yrk4 + 0.5D0*step*u(m)
zh = zrk4 + 0.5D0*step*dudt(m)
c-----k2-----
call histKim(th,t,u,dudt,len,m,aL,s0,ReT,hsum)
call Hfact(yh,aL,s0,HN)
hsum = hsum * HN
dym = dabs(zh)
call derk41W(yh,zh,Ton,DR,aL,s0,ReT,Re_imp,hsum,dzt)
yh = yrk4 + 0.5D0*step*dym
zh = zrk4 + 0.5D0*step*dzt
c-----k3-----
call histKim(th,t,u,dudt,len,m,aL,s0,ReT,hsum)
call Hfact(yh,aL,s0,HN)
hsum = hsum * HN
dym = dabs(zh)
call derk41W(yh,zh,Ton,DR,aL,s0,ReT,Re_imp,hsum,dzm)
yh = yrk4 + step*dym
zh = zrk4 + step*dzm
dym = dym + dym
dzm = dzt + dzm
c-----k4-----
th = trk4 + step
call histKim(th,t,u,dudt,len,m,aL,s0,ReT,hsum)
call Hfact(yh,aL,s0,HN)
hsum = hsum * HN
dym = dabs(zh)
call derk41W(yh,zh,Ton,DR,aL,s0,ReT,Re_imp,hsum,dzt)
yout = yrk4 + h6*(u(m) + 2.D0*dym + dym)
zout = zrk4 + h6*(dudt(m) + 2.D0*dzm + dzt)
return
end
*****NW rebound*****
subroutine rk42W(trk4,yrk4,zrk4,t,u,dudt,len,m,Ton,DR,aL,s0,
&           ReT,Re_imp,step,yout,zout)
IMPLICIT DOUBLE PRECISION (A-H,O-Z)

```

```

real(8) t(len),u(len),dudt(len)
h6 = step/6.D0
th = trk4 + 0.5D0*step
yh = yrk4 + 0.5D0*step*u(m)
zh = zrk4 + 0.5D0*step*dudt(m)
c-----k2-----
call histKim(th,t,u,dudt,len,m,aL,s0,ReT,hsum)
call Hfact(yh,aL,s0,HN)
hsum = hsum * HN
dym = zh
call derk42W(yh,zh,Ton,DR,aL,s0,ReT,Re_imp,hsum,dzt)
yh = yrk4 + 0.5D0*step*dym
zh = zrk4 + 0.5D0*step*dzt
c-----k3-----
call histKim(th,t,u,dudt,len,m,aL,s0,ReT,hsum)
call Hfact(yh,aL,s0,HN)
hsum = hsum * HN
dym = zh
call derk42W(yh,zh,Ton,DR,aL,s0,ReT,Re_imp,hsum,dzm)
yh = yrk4 + step*dym
zh = zrk4 + step*dzm
dym = dym + dym
dzm = dzt + dzm
c-----k4-----
th = trk4 + step
call histKim(th,t,u,dudt,len,m,aL,s0,ReT,hsum)
call Hfact(yh,aL,s0,HN)
hsum = hsum * HN
dym = zh
call derk42W(yh,zh,Ton,DR,aL,s0,ReT,Re_imp,hsum,dzt)
yout = yrk4 + h6*(u(m) + 2.D0*dym + dym)
zout = zrk4 + h6*(dudt(m) + 2.D0*dzm + dzt)
return
end
*****
subroutine polint(xa,ya,n,x,y,d_y)
IMPLICIT DOUBLE PRECISION (A-H,O-Z)
integer n,NMAX
real(8) dy,x,y,xa(n),ya(n)
parameter (NMAX=10)
integer i,m,ns
real(8) den,dif,dift,ho,hp,ww,c(NMAX),d(NMAX)
ns = 1
dif = dabs(x-xa(1))

do 3011 i = 1,n

```

```
dift = dabs(x-xa(i))
if (dift .lt. dif) then
  ns = i
  dif = dift
endif
c(i) = ya(i)
d(i) = ya(i)
3011 continue

y = ya(ns)
ns = ns-1

do 3013 m = 1,n-1
do 3012 i = 1,n-m
  ho = xa(i) - x
  hp = xa(i+m) - x
  ww = c(i+1) -d(i)
  den = ho-hp

  if (den .eq. 0) pause
  print *,'failure in polint'
  den = ww /den
  d(i) = hp * den
  c(i) = ho * den
3012 continue
  if (2*ns .lt. n-m) then
    d_y = c(ns+1)
  else
    dy = d(ns)
    ns = ns -1
  endif
  y = y + d_y
3013 continue
return
end
```